HIERARCHICAL AND HIGH THROUGHPUT MECHANICAL CHARACTERIZATION OF TITANIUM ALLOYS USING SPHERICAL INDENTATION STRESS-STRAIN CURVES

A Dissertation
Presented to
The Academic Faculty

by

Jordan S. Weaver

In Partial Fulfillment
of the Requirements for the Degree
Doctor of Philosophy in the
George W. Woodruff School of Mechanical Engineering

Georgia Institute of Technology

December, 2015

HIERARCHICAL AND HIGH THROUGHPUT MECHANICAL CHARACTERIZATION OF TITANIUM ALLOYS USING SPHERICAL INDENTATION STRESS-STRAIN CURVES

Approved by:

Dr. Surya R. Kalidindi, Advisor
George W. Woodruff School of Mechanical Engineering
Georgia Institute of Technology

Dr. Hamid Garmestani
School of Materials Science and Engineering
Georgia Institute of Technology

Dr. David L. McDowell
George W. Woodruff School of Mechanical Engineering
Georgia Institute of Technology

Dr. Olivier Pierron
George W. Woodruff School of Mechanical Engineering
Georgia Institute of Technology

Dr. Richard W. Neu
George W. Woodruff School of Mechanical Engineering
Georgia Institute of Technology

Dr. Ulrike G.K. Wegst
Thayer School of Engineering
Dartmouth College

Date Approved: October, 27 2015

To my family, especially my wife, Alicia, and my daughter, Frances

ACKNOWLEDGEMENTS

I wish to thank my advisor, Surya Kalidindi, who has provided support in many tangible and intangible ways throughout the entire tenure of my PhD. In particular, he has provided the technical knowledge and practical wisdom needed for being successful. I want acknowledge Professors Shriram Pillapakkam and Parsaoran Hutapea who encouraged me to explore research during my undergraduate studies at Temple University. I also wish to thank Dr. Rick Ricker who showed me the breadth of problems in materials science and engineering at N.I.S.T. that ultimately sent me down this path. I am greatly indebted to my fellow graduate students who have provided training, solutions, entertainment, and their perspectives on all sorts of subject matter. Specifically, I am grateful for simulation results from Mr. Matthew Priddy and Mr. Dipen Patel and insights into hexagonal materials from Mr. Ali Khosravani.

I am very thankful for support from the Army Research Office (ARO) (Co-PIs Drs. Surya Kalidindi and Ulrike Wegst) and the National Science Foundation (NSF CMMI-1333083) (Co-PIs David McDowell, Surya Kalidindi, and Donald Shih). Any opinions, findings, and conclusions or recommendations expressed here are those of the author and do not necessarily reflect the views of the NSF or the ARO.

Lastly, I wish to thank my family and friends who have supported and encouraged me through the completion of my PhD.

TABLE OF CONTENTS

LIST OF TABLES

Page

LIST OF FIGURES

Page

LIST OF SYMBOLS AND ABBREVIATIONS

α-Ti	hcp phase of Ti
β-Ti	bcc phase of Ti
α-Ti64	hcp phase of Ti64
β-Ti64	hcp phase of Ti64
Ti64	titanium alloy Ti-6Al-4V
BOR	Burgers orientation relationship
CP	Commercially pure
BASCA	β-annealed slow cooled and aged thermal process
STA	solution treated and aged thermal process
bcc	body centered cubic
hcp	hexagonally close-packed
wt.%	percentage by weight
P	load
P^*	load correction
$\tilde{P}$	uncorrected load
h	displacement
h^*	displacement correction
$\tilde{h}$	uncorrected displacement
$\tilde{h}_e$	uncorrected elastic displacement
h_e	elastic displacement
S	stiffness
A	contact area
a	contact radius

d	contact diameter
D	indenter diameter
R_i, R	indenter radius
β	elastic indentation modulus correction factor
E_{eff}	effective modulus
E_{ind}	indentation modulus
Y_{ind}	indentation yield strength
H_{ind}	initial indentation hardening
E	Young's modulus
E_s	sample modulus
v	Poisson ratio
v_s	sample Poisson ratio
E_i	indenter Young's modulus
v_i	indenter Poisson ratio
h_t	total displacement
h_r	residual displacement
h_c	contact height
h_s	sample displacement
CSM	continuous stiffness measurement/module
HCS / CS	harmonic contact stiffness
ΔP	harmonic load amplitude
P_{app}	machine load
P_{act}	CSM corrected load
ΔP_{rms}	harmonic load
Δh	harmonic displacement amplitude

h_{app}	term
h_{act}	CSM corrected displacement
Δh_{rms}	harmonic displacement
S_{act}	corrected stiffness
S_{app}	machine stiffness
TMP	thermo-mechanical processing
ND	normal direction
RD	rolling direction
TD	transverse direction
P_{gap}	normalized difference in load between the starting points for regression fits
h_{gap}	normalized difference in displacement between the starting points for regression fits
R2	r-squared
AAR	average absolute residual
MAR	maximum absolute residual
P_0	first load data point on ISS curve
h_0	first displacement data point on ISS curve
FIB	focused ion beam
ISS	Indentation stress-strain
EBSD	electron backscatter diffraction
OIM	orientation image microscopy
Φ	declination angle
Φ_1 , φ , Φ_2	Bunge-Euler angles
$\vec{a}$	a-type Burgers vector
$\vec{c}+\vec{a}$	c+a type Burgers vector

FEM	finite element method
SEM	scanning electron microscopy
SE	secondary electron imaging
BSE	backscatter electron imaging
TEM	transmission electron microscopy

SUMMARY

Recent work has shown the capability of spherical nanoindentation to capture local structure-property relationships in polycrystalline cubic metals by measuring indentation stiffness and yield strength from stress-strain curves as a function of the local microstructure in the indentation zone. However, these protocols capture structure-property relationships at only one level of the material hierarchy (e.g., single grains). Thus it is still very difficult to infer bulk structure-property relationships using these indentation protocols, which is mainly due to a lack of understanding indentation length scale effects and the important role played by structural hierarchy (i.e., unique structural features at different length scales). It is the goal of this work to extend these protocols to systematically study length scale effects of mechanical properties (e.g., indentation stiffness and yield strength) in titanium alloys. Alpha-beta titanium alloys were chosen because they display a rich variety of two phase microstructures and structural hierarchy and are well documented in literature. Firstly, nanoindentation protocols are extended to characterize the elastic and plastic anisotropy of a hexagonally close packed metal (alpha titanium in commercially pure and alloy Ti-6Al-4V) and a two phase microstructure (alpha-beta colony in Ti-6Al-4V). Secondly, spherical microindentation stress-strain protocols are developed and employed to characterize polycrystalline volumes in three titanium alloys (commercially pure, Ti-6Al-4V, and Ti18). The results of these major advances in indentation protocols and systematic study of length scale effects on the mechanical properties in Ti-6Al-4V will be presented and discussed along with

applications demonstrating their high throughput nature to rapidly explore alloy development.

CHAPTER 1

INTRODUCTION

The main thrust of this dissertation is to demonstrate protocols for capturing critically needed materials knowledge (structure-property relationships) at multiple length scales. This information is needed for the development of reliable physics based homogenization theories. It is no easy task to collect this information even for a single material system or family as it requires intense effort and may take many years to compile. One of the slowest steps is mechanical characterization, particularly at lower length scales because specialized equipment and sample preparation techniques are usually required. New mechanical characterization protocols are urgently needed that can capture the mechanical response at multiple length scales in a high throughput manner. An introduction of hierarchical materials and two common approaches for hierarchical mechanical characterization of structural alloys are detailed in this section. This is followed by the scope and layout of this dissertation.

1.1 Hierarchical Structure of Advanced Materials

Most materials used in advanced technologies have structural hierarchy (i.e., different salient features at different length scales). This nomenclature, structural hierarchy, was catapulted into the materials community more than two decades ago [1]. A common example used to illustrate multiple levels of structural hierarchy is bone [1-4] illustrated in Figure 1. This illustration has four levels of structural hierarchy: the molecular level of the collagen, the arrangement of collagen and hydroxyapatite into a microfibril, the arrangement of microfibrils into an osteon, and the arrangement of

osteons into bone. Each level is separated by length scale (i.e., nanometers to millimeters), has a distinct structure, and the performance is controlled by different mechanisms. A number of other examples exist in literature: seashell (nacre) [5, 6], wood [2], and bamboo [7] which have superior performance (e.g., toughness, stiffness per weight, and strength per weight) that makes them attractive as guides to designing new advanced materials [8-15]. Thus the terms structural hierarchy and superior performance have become linked descriptors. While these descriptors are more commonly applied to natural and biological materials, they can also be used to describe advanced structural alloys.

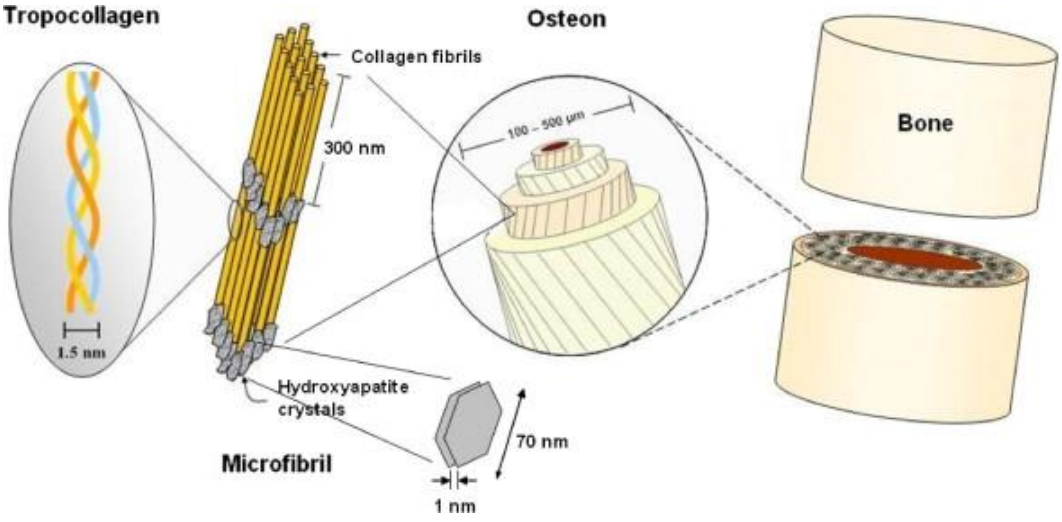

Figure 1: Illustration of the hierarchical structure in bone taken from [3].

The degree of structural hierarchy in advanced structural alloys in general is much less than that of biological and natural materials but none the less present. The example of most relevance to this work is the titanium alloy Ti-6Al-4V (Ti64). The different structural length scales can be categorized starting with the unit cell of atoms for an individual phase, the arrangement of α and β phases into grains (volumes of uniform unit cell orientation), the arrangement of α and β grains into colonies (volumes of

uniform alpha and beta grain orientations), and finally the arrangement of colonies in a polycrystalline aggregate (many colonies) that is the raw material. This is illustrated in Figure 2. These structural length scales are also separated mechanistically which requires a multi-scale approach (e.g., atomistic simulations, dislocation theory, crystal plasticity, and finite element methods) to make accurate performance predictions. The accuracy and advancement of such models relies heavily on gathering the information needed to quantify the material performance at each length scale. For structural materials this includes mechanical properties which are often highly anisotropic (i.e., depend on the orientation of the unit cell, feature, sample, etc.). Given the material hierarchy and mechanical anisotropy in structural alloys, it becomes apparent advanced hierarchical mechanical characterization tools are required.

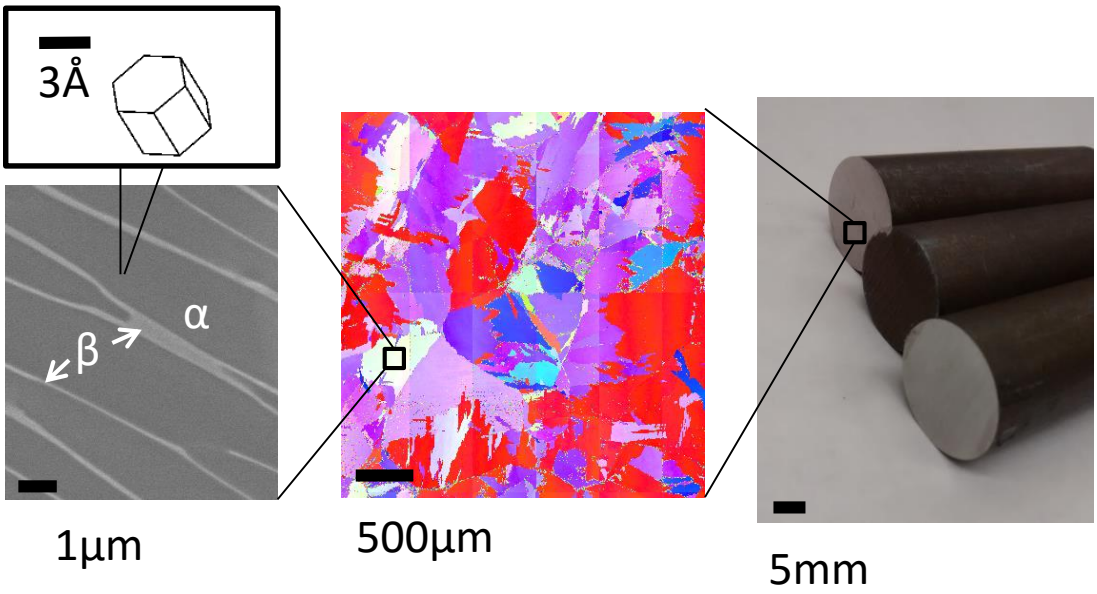

Figure 2: Illustration of the hierarchical structure in titanium alloy Ti-6Al-4V.

1.2 Hierarchical Mechanical Characterization of Structural Alloys

There are many methods for mechanically testing materials at a macroscopic or component length scale (e.g., uniaxial tension and compression, hardness, 3-point

bending, fatigue testing, etc.). The same methods are also available for testing specimens at the micro and nanoscale [16-19] which can be combined with macroscopic measurements to obtain materials knowledge across different structural length scales. Nanoindentation and micropillar compression are the most commonly employed test methods at the lower length scale. Each of these methods has its advantages and disadvantages which will be discussed in more detail.

1.2.1 Micropillar Compression

Micropillar compression involves fabricating micron to submicron diameter pillars using focused ion beam (FIB) milling and deforming the material in as close to a uniaxial compression stress state as possible. The specimen preparation is a slow process which requires highly specialized facilities and comes with certain challenges (e.g., ion beam damage, misalignment, non-uniform cross-section, etc.). However, it is highly advantageous for testing small features of various sizes in a variety of structural alloys. Second to the long sample preparation times, FIB damage to the specimen may also occur which can potentially alter the mechanical response. This problem has been documented for copper micropillars [20]. However, the effects or presence of FIB damage is often hard to quantity as in the studies on nickel micropillars [21, 22]. An alternative method to FIB was recently developed which uses chemical etching to make many samples [23]. Samples prepared with this technique subsequently showed greater relative strengths (i.e. closer to theoretical values). This raises some doubts about the quality of FIB micropillars for mechanical testing [23]. However, the etching micropillar technique is limited to certain microstructure morphologies and material systems. The present study relied [23] on the regular shape of one phase in a Mo alloy that could be

controlled with heat treatments. It is clear that standard micropillar compression testing protocols require long hours of sample preparation, and the results must be critically evaluated for the effects of FIB damage.

1.2.2 Nanoindentation

In contrast to micropillar testing, nanoindentation requires relatively simple equipment and sample preparation. The sample preparation is similar to procedures used in metallography (sectioning, grinding, and polishing), and large surfaces can be prepared quickly. Test procedures vary from the tip geometry to analysis protocols. A general test encompasses moving a hard indenter tip of known geometry into the sample surface while continuously measuring force and displacement. The indenter creates a highly heterogeneous stress field (as opposed to a uniaxial compression in micropillar testing) which typically leads to oversimplified analyses of the force and displacement data and the extraction of underwhelming material properties like hardness. Hardness is best used as a qualitative measure because it often depends on the test procedure and analysis protocols. The extraction of more quantitative properties from nanoindentation (e.g., uniaxial yield strength) has been achieved by establishing relationships between hardness and uniaxial strength [24], between load-displacement curves and uniaxial properties [25-28], and by converting load-displacement curves into indentation stress-strain curves [29-34]. The application of these analysis techniques are typically limited to a narrow range of materials or not capable of the accuracy required for moderate differences in material properties. However, recent advances in spherical nanoindentation protocols haves shown promising results where other protocols are lacking [35]. A high degree of effort is

required in order to extract meaningful and accurate material properties from nanoindentation, but it is cheap and fast.

1.3 Hierarchical and High Throughput Characterization of Titanium Alloys Using Spherical Indentation Stress-Strain (ISS) Curves

It should be obvious that indentation is the more attractive choice of the two test methods introduced for achieving high throughput. As was mentioned, some of the insufficiencies of nanoindentation analyses protocols to extract meaningful mechanical property information were addressed by Kalidindi and Pathak [31]. The details of these protocols and how they differ from more commonly used indentation protocols will be discussed in detail in Chapter 2. For structural alloys, theses protocols have only been used to make single phase, grain scale (i.e. in individual grains and near grain boundaries) measurements in polycrystalline metals with cubic symmetries [35-39]. In advanced materials there many more levels of hierarchy. This dissertation makes three major advances in indentation protocols by demonstrating their utility on titanium alloys:

1) Spherical nanoindentation stress-strain protocols are used to measure the grain scale elastic and plastic anisotropy of a hexagonal crystal (α-Ti in both commercially pure (CP) titanium and Ti64).
2) Spherical nano-ISS protocols are used to capture the 'grain' scale elastic and plastic anisotropy of the α-β colony feature in Ti64.
3) Spherical ISS protocols are developed for instrumented microindentation testing to capture a polycrystalline response (multiple grains at the indentation site) for three titanium alloys (CP-Ti, Ti-6Al-4V, and Ti18) with different α-β morphologies.

These three advances (hexagonal crystal, two phase, and polycrystalline indentation stress-strain measurements) demonstrated on titanium allows are presented and discussed in Chapters 5, 6, and 7 respectively. Prior to this, significant improvements to the spherical ISS protocols developed in this dissertation that have added a substantial amount of robustness are detailed in Chapter 3. The newly developed micro-ISS protocols are presented in Chapter 4 with a simple case study on an aluminum alloy. Chapter 9 summarizes and discusses the materials knowledge obtained through the demonstration of the protocols developed in this dissertation on Ti64. Lastly, the main conclusions and recommendations for future work are presented in Chapters 10 and 11, respectively. A comprehensive background of spherical indentation protocols including will be presented next with a brief overview of titanium alloys.

Chapter 2

Background

Indentation testing has existed for over 100 years [40]. The general test method has remained the same; however, the sophistication of test equipment and analyses has changed coincidently. There are two major types of indentation systems and analyses: traditional hardness measurements obtained by applying a specific force and measuring the geometry of the impression (e.g., [41, 42]) and instrumented indentation where properties are determined from the continuous measurement of force and displacement during loading and unloading [43]. An additional tool for instrumented nanoindentation is the continuous stiffness measurement (CSM) [44, 45] which replaces the need to unload the material in order to measure the modulus and hardness [16]. As its name implies, it provides this information continuously rather than at discrete points by fully unloading. For both types of indentation devices, there are a plethora of tip geometries: flat punch, spherical, spherical-conical, three-sided pyramid (Berkovich), wedge, cube corner, four-sided pyramids (Vickers), etc. There are distinct differences between sharp tip (e.g., Berkovich and Vickers) and spherical indentation protocols.

2.1 Limitations of Indentation with Sharp Tips

Indentation with sharp tips imposes a significant amount of deformation in the material, more so than spherical tips for similar test conditions. This is evident when considering the tip geometry. A pyramidal tip geometry will inevitably leave a residual impression even at small loads and displacements in a ductile material. In contrast, completely elastic loading and unloading (no residual impression) can be easily

accomplished with spherical tips at low loads and displacements. Intrinsically spherical indentation contains information about the virgin material's (without deformation) elastic response, elastic-plastic transition, and plastic deformation. Conversely, sharp tip indentation contains only the plastic response of the virgin material at high levels of deformation and the elastic response from a heavily deformed material. Thus, spherical indentation can potentially be more reliably related to the materials elastic and plastic properties (e.g., Young's modulus, yield strength, etc.).

2.2 Tabor's ISS Protocol

It is well known that traditional hardness measurements depend on test protocols for both sharp and spherical tips. This is evident in the standardization of test loads, tip materials and geometries, etc. for hardness measurements (e.g., [41, 42]). One reason for the dependence on the applied load is because the material under the indenter is going through a process of deformation which depends on the applied load. Thus it is an oversimplification to represent the material response with a single hardness measurement. Tabor [29] recognized this and performed spherical indentation on copper and steel measuring the hardness for different loads and assembling them into a single curve for each material. He reported the Meyer's hardness which is the load normalized by the projected contact area (P/A) also an effective or indentation stress [29]. The projected contact area was determined from the diameter of the impressions left after unloading. Tabor decided on a non-dimensional parameter for representing strain as the contact diameter divided by the indenter diameter (d/D). Using these two normalizations, the indentation measurements take on a similar shape to uniaxial stress-strain curves. Tabor scaled the uniaxial true stress by a factor of 2.8 and the uniaxial true strain by a factor of

0.2 showing reasonable agreement between the indentation and uniaxial curves [29]. The normalization of indentation measurements for different loads into representative stress and strain is an indentation stress-strain curve. There are numerous theoretical studies that support the relationship Tabor found between indentation and uniaxial stress-strain curves with only slight differences in the scaling factors [46-50]. However, the scaling relationship is limited to a fully plastic indentation zone or a specific range of d/D [33, 50].

2.3 Field and Swain's ISS Protocols

The protocols used by Tabor [29] required multiple indents at different locations with measurements of the residual impression after each indent. With the availability of instrumented indentation, Field and Swain [30, 51] developed spherical indentation protocols to analyze the load-displacement data of partial unloads to determine the contact area at maximum load. Field and Swain's analysis of the unloading curves relies on Hertz's theory [52] and a geometric definition of the contact radius at maximum load [16, 30, 43, 51]. Hertz's theory describes the relationship between the applied load, P, and the displacement, h, through an effective radius, R_{eff}, and modulus, E_{eff}, for isotropic, elastic, frictionless contact of axisymmetric surfaces [52, 53]. The equations are given below

$$P = \frac{4}{3} E_{eff} R_{eff}^{1/2} h_e^{3/2} \tag{2.1}$$

$$a = \sqrt{R_{eff} h_e} \tag{2.2}$$

$$\frac{1}{E_{eff}} = \frac{1-\nu_i^2}{E_i} + \frac{1-\nu_s^2}{E_s} \tag{2.3}$$

$$\frac{1}{R_{eff}} = \frac{1}{R_i} + \frac{1}{R_s} \quad (2.4)$$

where a is the contact radius, h_e is the elastic displacement, R_i, E_i, v_i and R_s, E_s, v_s are the indenter and sample radii, Young's moduli, and Poisson ratios, respectively. Field and The geometrical definition of contact radius used by Field and Swain is the same definition used by Oliver and Pharr [16, 33, 43]:

$$a = \sqrt{Rh_c - h_c^2} \quad (2.5)$$

where h_c is the contact depth determined from the unloading stiffness, S

$$h_c = h - \frac{3}{4}\frac{P}{S} \quad (2.5)$$

Equations 2.5 and 2.2 are equivalent for elastic loading. However, they deviate after plasticity occurs, and the difference is most pronounced for large strains [31, 54]. Which definition is better will be discussed in the next section. Using the theory described above for determining the contact radius at maximum load from partial unloads, Field and Swain plotted indentation stress-strain curves with definitions of indentation stress ($P/\pi a^2$) and strain ($a/R_i \; or \; d/D$) similar to Tabor [29]. The same protocols were adopted by Basu et al. [32] and Herbert et al. [33] for indentation testing using CSM instead of partial unloading.

2.4 Kalidindi and Pathak's ISS Protocols

Kalidindi and Pathak [31, 55] developed spherical indentation stress-strain protocols using a different definition of contact radius and indentation strain. Hertz's equations (Equations 2.1-2.4) are used including the definition of contact radius. In these protocols, the determination of an effective zero point is also required. The effective zero point deemphasizes errors in the machine determined zero point, small amounts of

surface roughness and tip disparities, and very thin oxide layers [31]. The zero point is determined from

$$S = \frac{3P}{2h_e} = \frac{3}{2}\frac{(\tilde{P}-P^*)}{(\tilde{h}_e-h^*)} \quad (2.6)$$

where S is the elastic unloading stiffness measured with CSM, $\tilde{P}$ and $\tilde{h}$ are the load and displacement from the machine zeroed data, and P^* and h^* are the load and displacement corrections [31]. Equation 2.5 is rearranged in order to determine the load and displacement corrections with a linear regression between $\tilde{P} - \frac{2}{3}\,S\tilde{h}_e$ and S:

$$\tilde{P} - \frac{2}{3}\,S\tilde{h}_e = -\frac{2}{3}\,h^*S + P^* \quad (2.7)$$

Without the zero point correction, the elastic-plastic cannot be clearly distinguished [31]. The data range for determining the zero point correction has to be confined to initial elastic loading. After the zero point correction is made ($P = \tilde{P} - P^*$ and $h = \tilde{h} - h^*$), a linear regression of Equation 2.1 using the initial elastic loading data can be made between $h^{\frac{3}{2}}$ and P to determine the effective modulus:

$$h = P^{\frac{2}{3}}\left(\frac{4}{3}E_{eff}R_{eff}^{\frac{1}{2}}\right)^{-\frac{2}{3}} + h_r \quad (2.8)$$

The effective radius is the indenter radius because the sample surface is flat. The total displacement, h, is related to the elastic displacement by

$$h = h_e + h_r \quad (2.9)$$

where h_r is the residual displacement. This value is theoretically zero for elastic loading. Up to this point, only the initial elastic contact has been analyzed. After plastic deformation occurs the surface is no longer flat ($R_s \neq 0$) and R_{eff} needs to be determined. Hertz's equations can still be used to analyze the unloading stiffness

measured by CSM because unloading is primarily elastic. The contact radius at any point can then be determined by

$$S = 2E^{*}a \tag{2.10}$$

where the effective modulus is assumed constant (measured from the initial elastic loading). This assumption is reasonable because the effective (average) plastic deformation in the indentation zone is quite small in these experiments. The protocols of Kalidindi and Pathak [31] define indentation stress and strain as:

$$\varepsilon_{ind} = \frac{3}{4\pi}\frac{h}{a} \tag{2.11}$$

$$\sigma_{ind} = \frac{P}{\pi a^2} \tag{2.12}$$

One of the advantageous of this definition of strain is that is has some physical relevance. It represents the compression of an indentation primary zone by an amount h. The primary zone is a cylinder with a diameter = $2a$ and a height of $2.4a$ [31]. This cylindrical zone is where most of the stress field and strains occur [31]. The definition of indentation strain then takes on a similar representation of change in length over length, and it has been shown to be a good measure of the effective (average) strain under the indenter [54]. The previous definition of contact radius (Equation 2.5) and indentation strain (proportional to a/R_i) yield the same results for the initial elastic loading [31, 54] However, the indentation stress-strain response differs significantly after plastic deformation [54].

Donohue et al. [54] critically evaluated the protocol differences with the finite element technique for isotropic elastic-plastic material behavior. They found that the protocols used by Kalidindi and Pathak yield more realistic strain hardening behaviors. For a perfectly plastic material, the indentation stress-strain curve had no hardening;

whereas, other protocols created significant amount of strain hardening as shown in Figure 3. They also found the geometrical definition of contact radius (Equation 2.5) better describes the actual contact radius while the protocols used by Kalidindi and Pathak estimate the Hertzian contact radius (i.e. one that is consistent with Hertz's theory). The reason these differ is because Hertz's equations are a solution to an equivalent contact problem of a flat surface and R_{eff} [52-54]. It is emphasized that the determination of the contact radius and definition of indentation strain by Kalidindi and Pathak are consistent with Hertz's theory and yield more representative indentation stress-strain curves of the uniaxial material behavior.

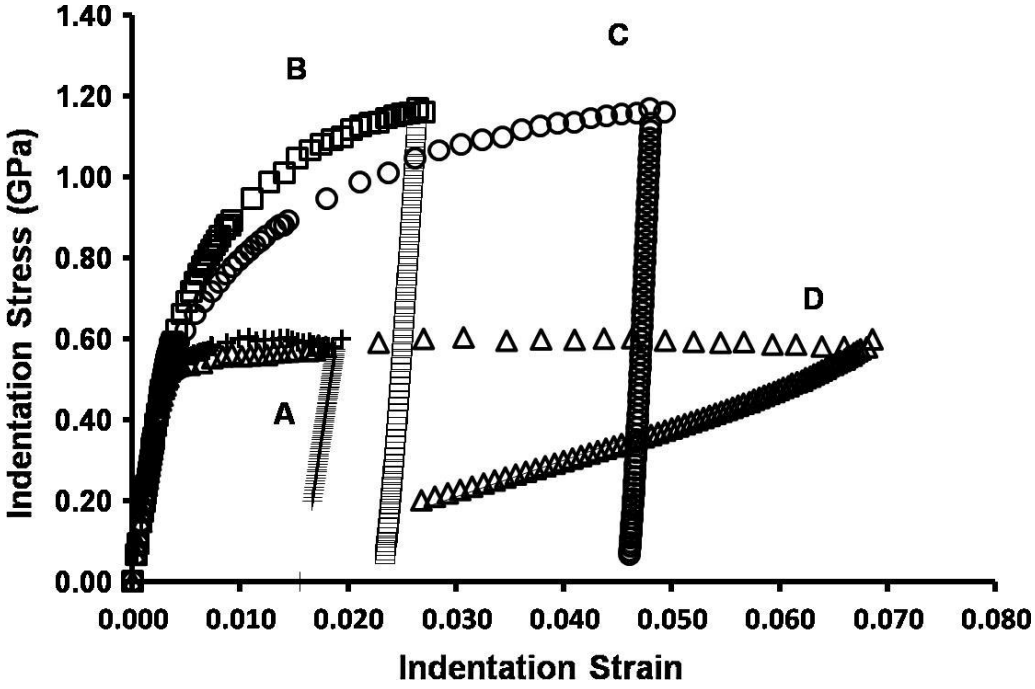

ε / a	$\left(\frac{3PR^*}{4E^*}\right)^{1/3}$	$\sqrt{2h_cR_i - h_c^2}$
$4h_t/3\pi a$	A	B
$4a/3\pi R_i$	D	C

Figure 3: ISS curves from FEM indentation simulations evaluating the different protocols for contact radius and indentation strain taken from [54].

2.5 Indentation of Elastically Anisotropic Materials

One of the major assumptions in Hertz's theory is that the material is elastically isotropic [52]. However, especially in nanoindentation, the material being indented is often elastically anisotropic. A general expression of the relationship of the effective modulus for the elastic contact problem can be expressed as

$$\frac{1}{E_{eff}} = \frac{1-v_i^2}{E_i} + \frac{1}{E_{ind}} \quad (2.13)$$

where the indentation modulus, E_{ind}, is a function of the elastic stiffness parameters of the indented material. For example, for an isotropic material, $E_{ind} = \frac{E}{1-v^2}$, where E and v denote the Young's modulus and the Poisson's ratio, respectively. Such expressions for general anisotropic materials are not currently available. Willis [56] derived an expression for an anisotropic elastic medium; however, the expression cannot be solved directly except for the special case of transverse isotropy. Vlassak and Nix numerically solved the problem for select cases of cubic symmetry (indentation on {100}, {111}, {110} surfaces) primarily based on a flat punch indenter [57]. Based on their studies, they found that E_{ind} for anisotropic materials can be expressed as

$$\frac{1}{E_{eff}} = \frac{1-v_i^2}{E_i} + \frac{1}{\beta}\left(\frac{1-v^2}{E}\right)_{iso} \quad , \quad (2.14)$$

where the indentation modulus is the multiplication of a correction factor, β, and the isotropic equivalent elastic indentation modulus [57, 58]. In their study E and v were calculated from a polycrystalline random textured aggregate [57, 58]. For cubic materials the authors interpolated between calculations of the correction factor using a function dependent on the anisotropy ratio and Poisson ratio in the cube directions [57, 58]. Additional methods for calculating the indentation modulus for different indenter geometries have since been formulated [59-61]. However, calculating the indentation modulus for an arbitrary orientation and symmetry is most practically done through the finite element technique. Patel et al. [62] modeled spherical indentation for cubic materials and confirmed the formulation of Vlassak and Nix for indentation modulus (Equation 2.14). Most importantly, his simulations showed that when using Equation

2.13 in conjunction with Hertz's theory (Equations 2.1-2.4), there is still a linear relationship between P and $h^{\frac{3}{2}}$. This relationship is central to the nanoindentation stress-strain analysis protocols [31].

In addition to the orientation dependence of the indentation modulus for anisotropic materials, the contact area shape becomes elliptical [56-61]. Hertz's equations (Equations 2.1-2.4) are limited to a spherical contact area described by a contact radius. However, the difference between circular and elliptical was shown to have a minimal effect on the calculation of indentation modulus [59-61], and likely the accuracy of the contact area as well.

Pathak et al. performed indentation experiments on differently oriented grains in polycrystalline Fe-3%Si which have significant elastic anisotropy [37]. The indentation modulus showed a dependence on the crystal orientation at the indentation site. Pathak et al. compared measurements on crystals oriented with the indentation axis close to {100}, {111}, {110} planes to Vlassak and Nix's calculations [58] by comparing the β correction factor. The theoretical correction factor and one determined from these experiments were in good agreement. Based on the experiments of [37] and simulations of [62] it becomes apparent that the spherical nanoindentation stress-strain protocols are capable of capturing elastic anisotropy through the orientation dependence of the indentation modulus. Patel et al. also demonstrated that the material elastic constants could be extracted from indentation modulus measurements for cubic materials [62].

2.6 ISS and Orientation Image Microscopy (OIM) Studies of Polycrystalline Cubic Metals

Pathak et al. used the ISS protocols to capture the anisotropic elastic and plastic behavior in polycrystalline Fe-3%Si using a combination of spherical nanoindentation and electron backscatter diffraction (EBSD) measurements [37]. They were able to correlate changes in indentation modulus and yield strength with the local crystal orientation, Figure 4. Additionally, they observed increases in the indentation yield strength after macroscopic deformation (30% and 80%) was applied. These increases in the indentation yield strength corresponded to increases in the dislocation density and slip resistances. They showed the indentation yield strength measured on the ISS curve is sensitive to subtle changes in the local structure (crystal orientation and dislocation density) at the indentation site [37]. Pathak et al. also demonstrated the utility of the indentation stress-strain protocols (e.g., indentation yield strength) for quantifying the heterogeneous deformation that happens in grain boundary regions [36]. Vachhani and Kalidindi recently applied the ISS protocols to study deformation mechanism in polycrystalline high-purity aluminum [38, 39]. Through these studies Fe-3%Si and Al it was demonstrated that microstructure-property relationships can be determined from EBSD and indentation stress-strain measurements in polycrystalline cubic metals.

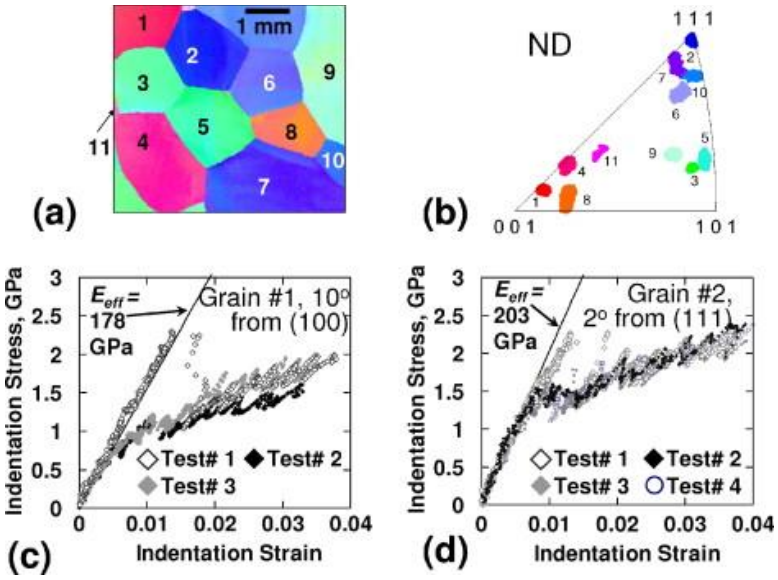

Figure 4: OIM and spherical nanoindentation to measure the grain scale elastic-plastic anisotropy (indentation modulus and yield strength) using indentation stress-strain curves taken from [37]. (a) OIM grain map (color represents orientation, (b) IPF triangle corresponding to OIM grain map, (c) ISS measurements for Grain #1, and (d) ISS measurements for Grain #2.

2.7 Indentation Size Effects

It is important to understand size effects that are observed in indentation testing in order correctly interpret indentation measurements made across multiple length scales. There are numerous size effects (i.e., properties depend on the size of the material tested) reported in nanoindentation measurements [63-67]. The commonly reported size effects are higher hardness values at small depths [63] and with small radius indenters [64, 66] and the dependence of pop-ins on indenter radius [68-70]. A common explanation for the increase in hardness at small depths during nanoindentation is the large strain gradient under the indenter creates a high number of geometrically needed dislocations (GNDs) which in turn increases the measured hardness [63, 65]. Pharr et al. [66] critically reviewed the hardness size effects reported in literature for Berkovich and spherical indentation and noted that sample preparation and test procedures have a significant

effect on the reported increase in hardness at small depths. Some examples include a reduced size effect for electropolished surfaces compared to mechanically polished surfaces, errors in the function used to describe the contact area, and errors in the machine zero point [66].

No size effect was observed for the indentation yield strength measured from indentation stress-strain curves for 10-100 μm radius indenters [36, 38, 39, 71]. Comparatively, literature reports a size effect on hardness for a similar range of indenter radius [64, 66]. The biggest size effect that has to be contended with in indentation stress-strain measurements is the pop-in size effect. A pop-in (displacement burst) occurs when there are not enough dislocation sources (e.g., Frank-Read source) in the volume being tested to generate the necessary dislocation multiplication and movement required for the material to plastically deform [68-70, 72]. Pop-ins are larger in well annealed materials with low dislocation densities and indentation with small indenter sizes (e.g., 1 μm radius). Pathak et al. [73] showed that a small amount of surface disturbance (vibropolishing) will suppress pop-ins without changing the shape of the pre and post pop-in ISS curve. In this way, the indentation yield strength can be defined for tests with small pop-ins using a back-extrapolation of the post pop-in ISS curve [36-39]. The indentation yield strength then corresponds to the material state where there is the minimum number of dislocation sources to avoid the need to generate a dislocation source and the displacement burst associated with it. This is illustrated in Figure 5. This of course breaks down for significantly large pop-ins or when there is no data without pop-ins to compare and verify the accuracy of using a back extrapolated indentation yield strength. The indentation yield strength is less sensitive to the choice of tip radius than

hardness which allows data from multiple tip sizes to be used without complications from size effects.

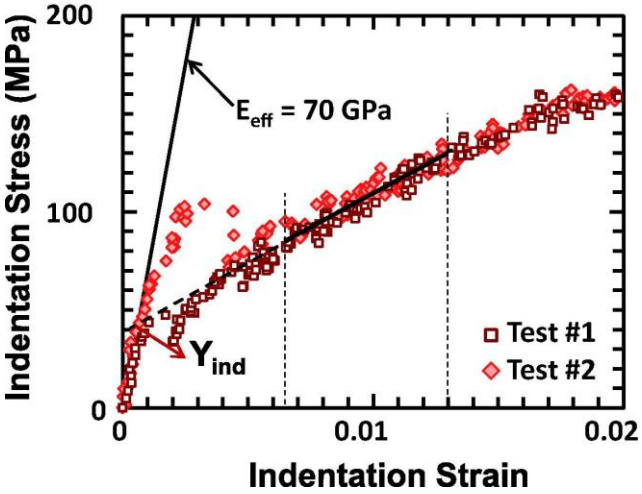

Figure 5: Example of back extrapolated indentation yield strength from [39].

2.8 Titanium Alloys

Titanium alloys were chosen for demonstrating the hierarchical mechanical characterization protocols because they contain a variety of microstructure morphologies including phase boundaries and complexity. Ti64 was particularly chosen because of its industrial importance, and it has been widely studied. A brief background on titanium alloys is provided here. A more comprehensive background can be found in these sources [74, 75].

2.8.1 Structure

Titanium alloys are typically classified based on the amounts of α and β phases that are present [74]. The α-phase is a hexagonal close packed crystal while the β-phase is body centered cubic. At room temperature, pure titanium is present in the α-phase. Certain alloying elements (e.g., V, Mo) stabilize the β-phase at room temperature while

others (e.g., Al, 0) stabilize the α-phase. The microstructure of titanium alloys is largely controlled by the addition of alloying elements and thermo-mechanical processing (TMP). An important temperature for TMP is the α-β transition temperature (882°C for pure titanium) [74]. The transition temperature will change depending on the amount of α and β stabilizers present. The structural morphology for different TMP above and below the β transition temperature in Ti64 ranges from equiaxed α grains with β at grain boundaries, fully lamellar α-β grains, and a duplex structure containing both equiaxed and lamellar grains. The misorientation of the α and β crystals are also related by the Burgers orientation relationship (BOR) [76] shown in Figure 6. This relationship is observed in most α-β titanium alloys which have undergone mild cooling rates and deformation during TMP.

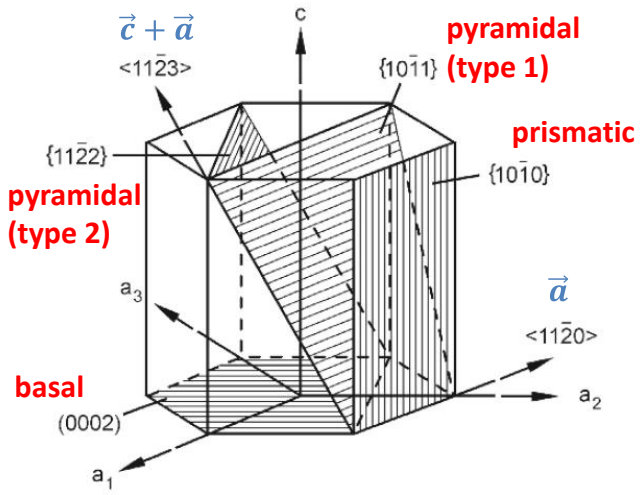

Figure 6: Schematic of α-β orientation relationship from [74].

2.8.2 Properties

Titanium alloys are primarily used in applications where corrosion resistance, high strength to weight ratios, and/or high fatigue life is required. At the crystal length scale, α and β are both elastically anisotropic [77, 78]. The plastic properties of α-Ti are

particularly interesting because of the differences in slip resistances across slip systems and occurrence of twinning. Titanium (α-Ti) has $\vec{a}$ and $\vec{c}+\vec{a}$ type Burgers vector characterized slip along with twinning to accommodate plastic strain. There are three families of planes for $\vec{a}$ type Burgers vectors ($\{0001\},\{10\bar{1}0\},\{10\bar{1}1\}$) and two families of planes for $\vec{c}+\vec{a}$ type Burgers vectors ($\{10\bar{1}1\},\{11\bar{2}1\}$). The slip systems are often designated basal, prismatic, and primary and secondary pyramidal as shown in Figure 7 [74]. The slip and twinning activity heavily depend on chemical composition. The dependence will be discussed in more detail in the relevant sections of Chapters 5, 6, and 7.

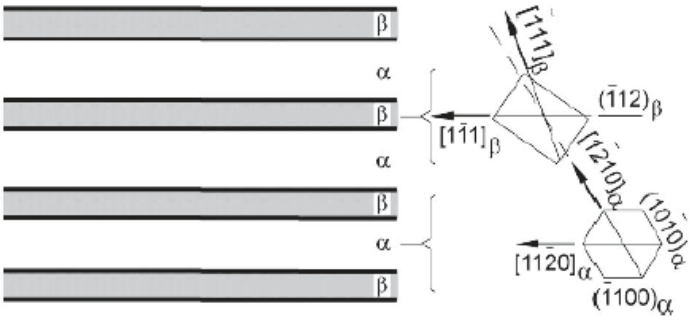

Figure 7: Schematic of hcp unit cell with slip systems labeled modified from [74]

Chapter 3

Improvements to Understandings and Protocols of Nano-ISS Analyses

The methodology for spherical indentation stress-strain curves developed by Kalidindi and Pathak [31] was reviewed in Chapter 2. In this chapter, a number of refinements to the protocols developed in this dissertation, which have added significant robustness, will be detailed. These include an alternative explanation for the zero-point correction, use of CSM corrections, accounting for the displacement of the indenter tip in the calculation of indentation strain, quantify the appropriate selection of the elastic segment as well as the variance of indentation properties due to this process, and the use of a strain offset for measuring indentation yield strength.

3.1 An Alternative Perspective of the Zero-Point Correction

The process of establishing an effective zero-point is critical to recovering the elastic and elastic-plastic transition in the nanoindentation stress-strain curve. The physical reasons for this correction include small disparities in the assumed tip and sample geometry caused by surface roughness, other surface conditions such as a thin oxide layer, and errors in the machine determined zero-point [31]. The machine determines the beginning of the test and the zero-point using two different approaches [79]. The start of the prescribed loading regiment is determined by an increase in the load-displacement slope. This value increases sharply when the tip comes into contact with the sample. However, it is not as accurate as the increase in the CSM signal, and so the machine places the zero-point post-test based on a user defined stiffness value (typically 200 N/m) using the CSM signal, Figure 8. The zero-point correction for ISS

measurements also relies on CSM. While the zero-point can be established without CSM [55], all subsequent studies have used CSM. In theory, only the load and displacement are needed to establish the indentation modulus in the initial elastic loading. The redundant signal from CSM, S, is used to correct the load, P, and displacement, h. Here lies some additional understanding of the zero-point correction and the importance of CSM for indentation stress-strain protocols.

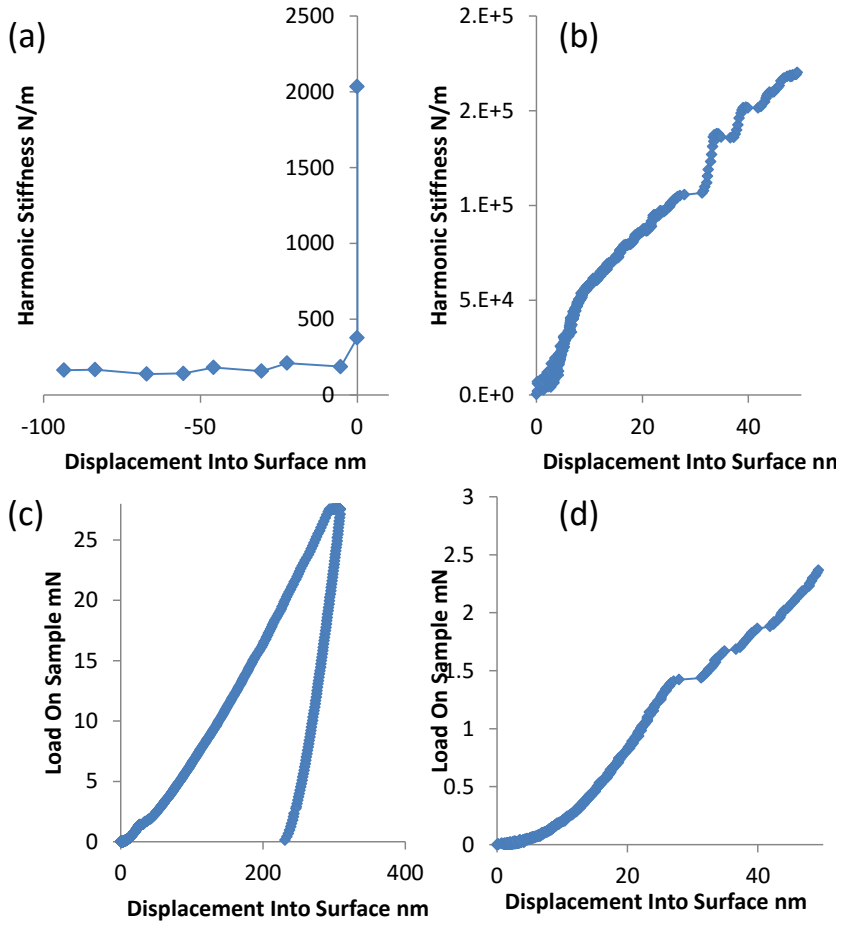

Figure 8: Indentation signals for a 16 µm radius indenter on CP Ti. (a) The stiffness (a.k.a. Harmonic Contact Stiffness (HCS)) in air before contact and the first two points after contact showing a sharp increase, (b) The stiffness during the initial 50 nm of depth, (c) The load-displacement curve for the entire test, and (d) The load-displacement curve for the first 50 nm. The first discontinuity is a pop-in event followed by further smaller ones.

Hertz's theory identifies a relationship between the three signals for a spherical indenter as

$$S = \frac{3P}{2h_e} \tag{3.1}$$

Note the stiffness measured by CSM is the unloading stiffness, where unloading is considered to be primarily elastic. In the initial elastic loading of the material, the total displacement and the elastic displacement are equivalent. The left and right hand side of the equation can be compared before and after the zero-point correction to see its effect, as seen in Figure 9. Notice that only a portion of the initial data is selected to establish the zero-point correction (i.e., the range is from 8 nm to 15 nm). Prior to the zero-point correction, there is poor agreement for the expected relationship in Equation 3.1. The zero-point correction brings the expression on the right hand side of the equation into agreement with the quantity on the left hand side. Thus, the zero-point correction establishes an effective zero-point for the load and displacement which deemphasizes the first point of contact. The first point of contact is not likely described by the geometry of a spherical tip indenting a flat surface due to tip and surface roughness at this length scale. It is clear that the accuracy of the stiffness measurement is critical for a reliable effective zero point and ISS curve. Therefore, an additional consideration of the CSM corrections described in literature is warranted.

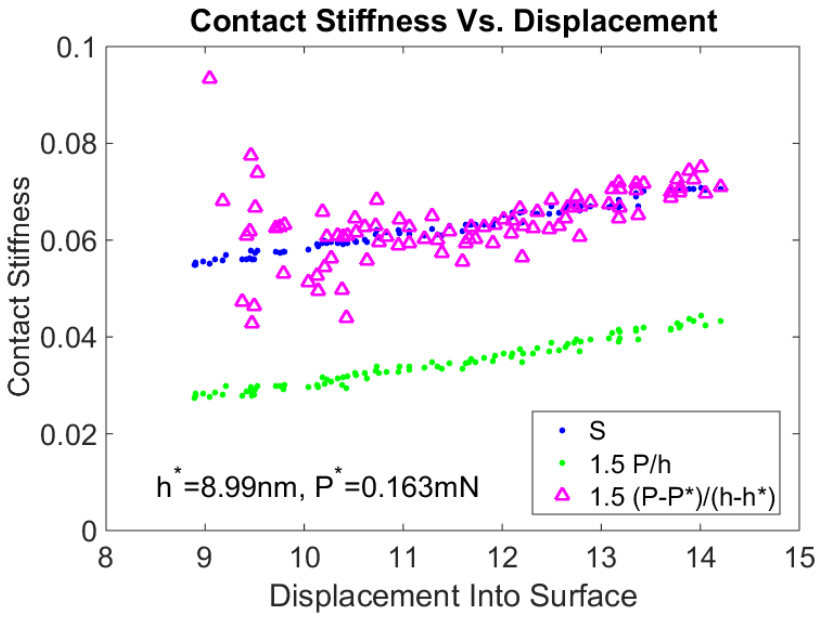

Figure 9: Alternative visualization of the effect of the zero-point correction. Data is the same used in Figure 8.

3.2 Revisiting CSM Corrections

It is well documented in literature that there are small errors in the load, displacement, and stiffness measurements due to the data acquisition protocols of the test equipment [80-82]. The load (input) and displacement (response) signals have both a monotonic (DC signal used on the loading coil) and oscillatory (AC signal) when CSM is used [79]. The machine typically reports the mean load and displacement, when in actuality the sample experiences slightly higher loads and displacements due to the superimposed oscillatory load. The corrections proposed for load and displacement are

$$P_{act} = P_{app} + \frac{\Delta P}{2}, h_{act} = h_{app} + \frac{\Delta h}{2} \quad (3.2)$$

$$\Delta P = 2\sqrt{2}\Delta P_{rms}, \Delta h = 2\sqrt{2}\Delta h_{rms} \quad (3.3)$$

where the actual (act) and apparent (app) are the corrected and machine determined signals, respectively, and the root mean squared (rms) values of the oscillatory signals are

the machine recorded harmonic load and displacement. In addition to these corrections, the harmonic contact stiffness also has an error due to the assumption that $S = \frac{dP}{dh} \approx \frac{\Delta P}{\Delta h}$. In actuality, the relationship between load and displacement is nonlinear. For very small displacements, $\frac{\Delta P}{\Delta h}$ is a reasonable approximation. Following the formulation described by Phar et al. [81], Vachhani et al. [80] derived the following correction for the measured stiffness for the case of a spherical indenter:

$$S_{act} = \frac{1}{\sqrt{2\pi}} \frac{P_{max}}{\Delta h_{rms}} \left(\frac{1}{K}\right)^{\frac{1}{m}} \left[1 - \left(1 - \frac{2\sqrt{2}\Delta h_{rms} S_{app}}{P_{max}}\right)^{\frac{1}{m}}\right] \quad (3.4)$$

$$K = 0.6524,\ m = 1.5,\ \ P_{max} = P_{act} \quad (3.5)$$

This correction to the stiffness contains an expression that might produce imaginary values. This condition corresponds to tapping (i.e., the indenter is coming in and out of contact with the surface), which can occur during the initial contact with the sample [81, 82]. In this condition,

$$P_{act} - 2\sqrt{2}\Delta h_{rms} S_{app} < 0 \quad (3.6)$$

which is also equivalent to

$$P_{act} - \Delta P < 0 \quad (3.7)$$

and will produce an imaginary S_{act}. The equation above also means that in order for full contact to occur, the monotonic load must be equal to or greater than the harmonic load amplitude. Pharr et al. [81] calculated the depth at which tapping will stop based on the material properties (modulus and hardness). When the material properties are not known a priori, a plot of P_{act} and $2\sqrt{2}\Delta h_{rms} S_{app}$ (labeled ΔP) shown in Figure 10 can assist in determining when tapping has ceased. In this case, tapping is assumed to cease as soon as

S_{act} is a real number. A clear transition can be seen when the apparent load exceeds the harmonic load (calculated as above).

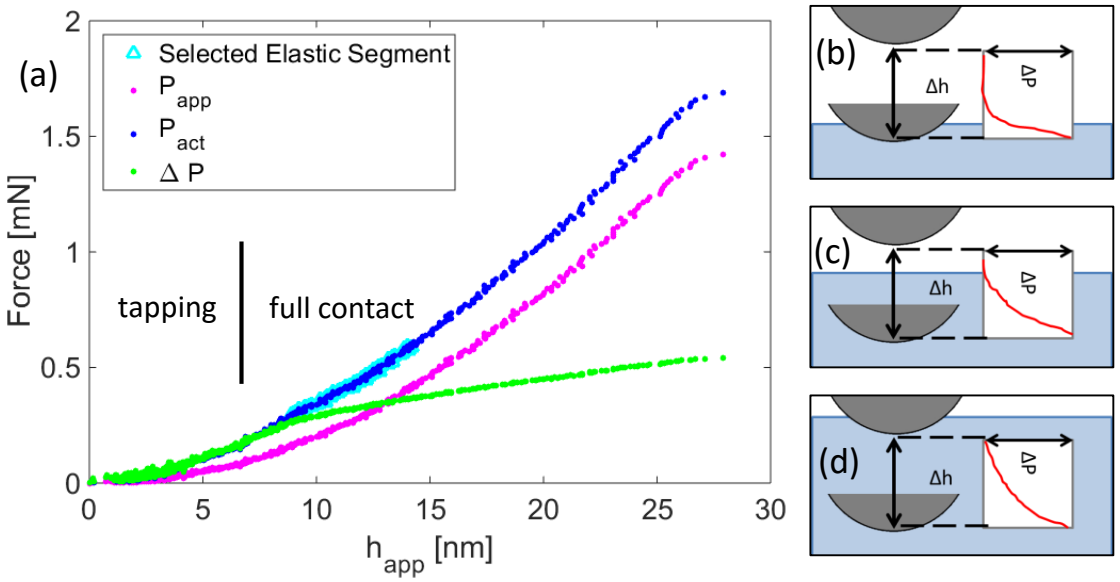

Figure 10: (a) Examination of harmonic and monotonic forces versus the apparent displacement which illustrates the effect of the harmonic load correction (pink and dark blue curves) and a transition from possible tapping to full contact (blue and green curves). The selected elastic segment used for determining the zero-point correction and modulus is highlighted (light blue) on the actual load curve (blue). An illustration of (b) tapping, (c) transition point between tapping and full contact, and (d) full contact.

Vachhani et al. [80] critically evaluated the effect of the load, displacement, and CSM corrections on the indentation stress-strain protocols for fused silica and pure aluminum. They determined that the combined effect on the overall indentation stress-strain curve is negligible for these materials. This makes sense because establishing the effective zero-point downplays tapping by deemphasizing the first few nanometers of contact. Conversely it was also observed that the corrections tended to discard data that was useful in determining the zero-point correction due to the imaginary values of the corrected stiffness [80]. This would have been data at the transition between tapping and full contact. However, without using Equation 3.4, it is not apparent how much data used

for the zero-point correction is potentially below the transition from tapping to full contact. Furthermore, it is not clear if the conclusions from Vachhani et al. [80] apply to other materials. Consequently, rather than evaluate the impact of these corrections for each new material, it makes sense to consistently apply the CSM corrections to load, displacement, and stiffness. This also makes sense given the importance of the stiffness signal for determining the zero-point correction. In summary, the CSM corrections are used to add robustness to the nanoindentation stress-strain protocols and avoid pitfalls in analyzing the initial contact caused by erroneous CSM data due to tapping.

3.3 Accounting for the Indenter Tip Elastic Displacement in the Calculation of Indentation Strain

For a rigid indenter, the displacement measured by the indentation machine is the sample displacement. In reality the indenter is not rigid, and the machine displacement is a combination of the indenter and sample displacements as shown in Figure 11. The surface profiles of deformable bodies in contact predicted by Hertz's theory are well illustrated in the book by Johnson [53]. Since strain in intrinsic to the material, its definition (and computed value) should be independent of the material properties of the indenter. In other words, we need to subtract the elastic displacement in the indenter from the total displacement measured in the experiment. One can approach the tip elastic displacement as being similar to a compliance correction in conventional testing protocols. Note that the indenter machine compliance is something different, and it is already accounted for in the measured total displacement.

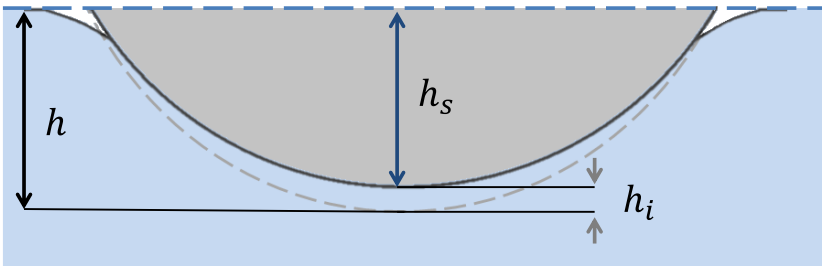

Figure 11: Schematic of indenter and sample highlighting the individual displacements of the sample and indenter. The solid line profiles are the indenter and sample surfaces during contact. The dotted lines are the indenter and sample original surfaces or in the unloaded state for complete elastic recovery.

The indenter displacement can be estimated through Hertz's theory. If we consider contact loading between the indenter and a rigid surface, the elastic displacement in the indenter can be expressed as

$$h_i = \frac{3\left(1-\nu_i^2\right)P}{4E_i a} \tag{3.8}$$

where the displacement is a function of the current load, contact radius, and the indenter elastic properties. Note that the displacement becomes zero for a rigid indenter and will become more significant for a compliant the indenter (e.g., steel instead of diamond). The sample displacement can then be estimated at any point during the actual test as $h_s = h - h_i$. Thus, the indentation strain can be calculated using the sample displacement

$$\varepsilon_{ind} = \frac{4}{3\pi}\frac{h_s}{a} \tag{3.9}$$

The calculation of the tip displacement shown above is similar to one reported in literature [83, 84] and only differs by the leading constant (~0.64 instead of 0.75) which has a negligible effect.

The correction for the displacement of the indenter is only needed for the determination of the indentation strain. Hertz's equations used for the zero point and modulus determination already account for the tip compliance through the indenter's

elastic properties. Some authors have chosen to subtract the indenter displacement prior to the determination of the unloading modulus [84, 85]. However, it is not necessary in order to determine the indentation modulus [86].

Any correction for the indenter displacement is rarely applied in literature. In many cases the properties measured using indentation are not affected or the effect is negligible. Additionally, the modulus of nanoindenter tips is typically 10 times the sample modulus making the displacement correction rather small. Le [87] modeled the effects of a non-rigid indenter with finite element method using a diamond indenter ($E = 1140\ GPa$, $v = 0.07$) for a variety of materials. He concluded the indenter displacement is less significant for softer materials and at deeper indentation depths. In order to avoid the errors associated with harder materials (or softer tips) and shallow indentation depths, the tip displacement should be accounted for before calculating indentation strain.

3.4 Accounting for the Variance in ISS Properties Due to Analysis Protocols

Previous nanoindentation studies have estimated variance by doing repeated measurements inside the same grain or microstructural feature [35-39]. What has not been discussed or addressed is the uncertainty arising from analyzing a single test (i.e., multiple answers for one test). Multiple answers can be found for a single test due to the analysis protocols of selecting the appropriate initial elastic segment. Figure 12 illustrates this point where the ISS curve for one choice (blue) is straddled by two other choices (black). The statistics of the properties determined from twenty solutions for one test is given in Table **1**. The protocols for identifying the elastic segment in the load-displacement curve have also not yet been standardized. It is critical to record multiple

potential estimates of ISS properties of interest (modulus, yield strength, initial hardening, etc.) from a single test and estimate the inherent uncertainty involved. A workflow addressing this critical need is presented in this dissertation, which provide some means for standardization and accounts for the uncertainty associated with multiple answers from a single test.

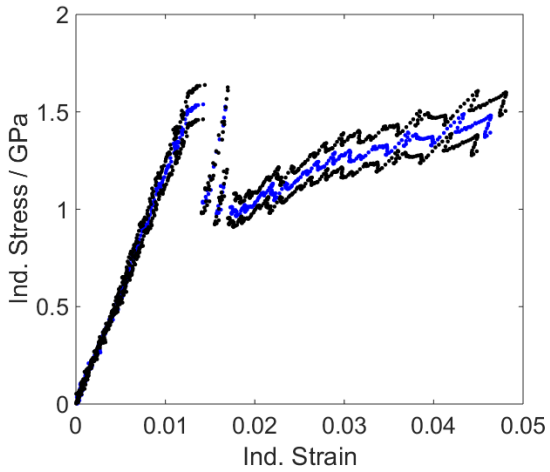

Figure 12: Variance of ISS curve and properties for 20 appropriate answers. The data is from a 16 µm radius indenter on CP Ti.

Table 1: ISS average properties for multiple analyses of one test corresponding to Figure 12.

Units: GPa	**E_{ind}**	**Y_{ind}**	**H_{ind}**
Mean	115.6	0.7713	24.3
Median	115.8	0.7744	24.3
Standard Dev.	2.74	0.0174	1.30
Minimum	110.4	0.7352	22.1
Maximum	119.9	0.7951	26.5

The variation in the analysis protocols is tied to the choice of appropriate initial elastic segment. The strategy used here was to analyze a multitude of choices for the initial elastic segment, filter the results based on well-defined metrics, and compute the statistics (mean, standard deviation, etc.) of the properties measured on all the appropriate answers. The metrics used are listed in Table 2. The actual values for each metric are

likely to depend on the material, indenter size, test parameters, etc. However, a knowledge base of acceptable values leading to the best analyses can be built and applied for future tests. This will lead to consistent, repeatable, and potentially automated results reducing the time spent finding the appropriate elastic segment.

Table 2: List of quantifiable metrics for the identification of the initial elastic segment.

General Guidelines	Current Quantification	Proposed Quantification
Quality of linear regressions	R^2, h_r	R^2, h_r, average and maximum absolute residuals
Overlap of segments for regressions	none	h_{gap}, P_{gap} (normalized displacement and load differences between linear regressions Eqns. 2.7-2.8)
Realistic zero-point	h^*, P^*	h^*, P^*
Realistic Modulus	E_s	E_s
ISS curves goes through origin	none	H_0, P_0 (first load and displacement data point)
Elastic ISS segment is linear and matches regression analysis	none	average (AAR) and maximum absolute residuals (MAR

As an example, the ISS curves for three tests inside the same grain are shown in Figure 13. The curves in Figure 13 are representative curves for each test (i.e., The ISS curve for each test is one of multiple curves captured in the proposed workflow). It can be seen that the variance in each property for each test is comparable to the in grain variance (differences in average properties). Previous protocols measured the variance from multiple tests using one analysis per test which is also a good measurement of the uncertainty. However, computing the variance for each test adds some robustness to the data analyses protocols because it allows the user to measure uncertainty for single test. This is particularly important when it is not possible to run multiple tests on the same microstructure feature (e.g., grain). Previous studies were on very large grains in order to

develop the indentation stress-strain protocols. In some materials it is not possible, very difficult or impractical, to make the features large enough for repeated indentation on the same feature, particularly the α-phase in Ti-6Al-4V.

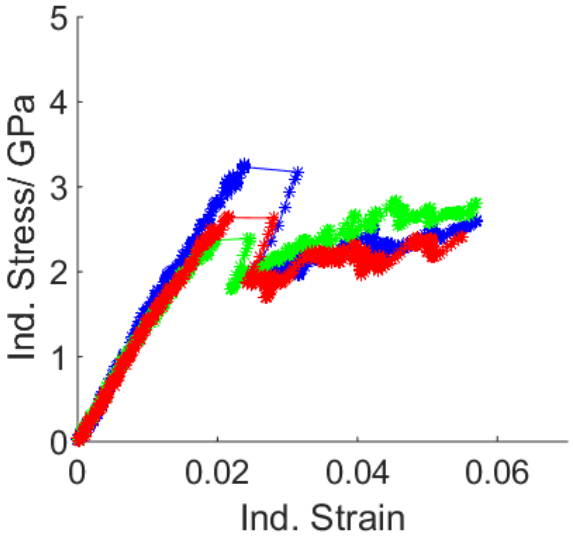

Figure 13: Variance of ISS curve and properties for 3 tests in the same grain. Tests are from a 16 µm radius indenter on CP Ti.

Table 3: ISS measurement averages and standard deviations for three different tests in the same grain. The data corresponds to Figure 13.

	Test 1	**Test 2**	**Test 3**
E_{ind} [GPa]	138.4 ± 6.6	144.1 ± 2.9	138.0 ± 7.1
Y_{ind}[GPa]	1.62 ± 0.13	1.52 ± 0.05	1.57 ± 0.02
H_{ind}[GPa]	27.8 ± 2.1	39.9 ± 1.3	31.0 ± 7.7
a_{yield} [nm]	287 ± 14	529 ± 14	309 ± 32
Pop-in stress [GPa]	3.30 ± 0.27	2.41 ± 0.10	2.85 ± 0.25

Using the approach above, the average metrics defined in Table 2 for the elastic segment for each test were compiled for all the nanoindentation analyses in this dissertation. The resulting histogram plots for reach metric are show in Figure 14. These metrics could be used for standardization and automating the analysis.

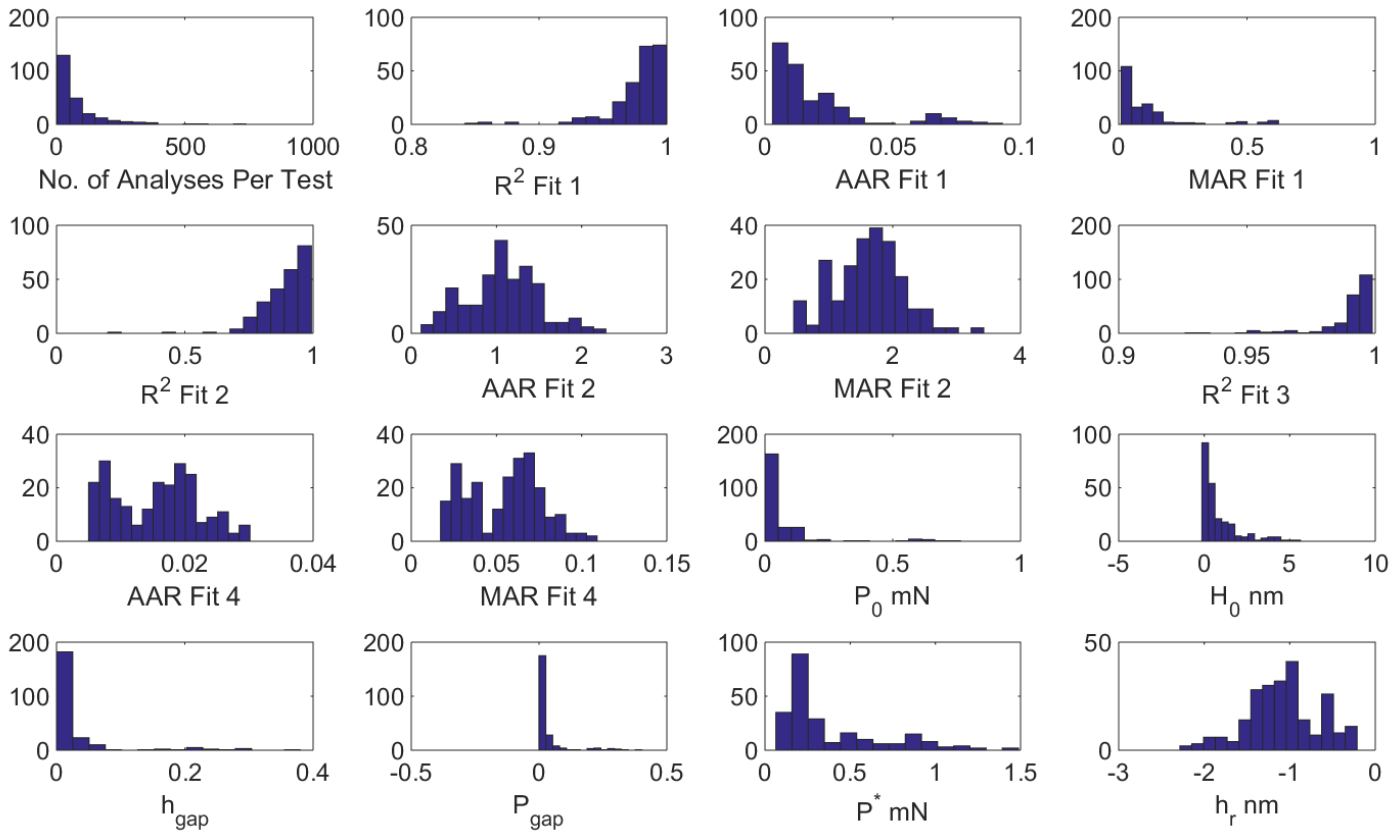

Figure 14: Histogram plots for the average elastic segment metrics for all nanoindentation tests (> 200). Fits 1 and 2 correspond to Eqns. 2.7 and 2.8. Fit 3 is a linear fit to the elastic indentation stress-strain data. Fit4 is measuring the error between the indentation modulus line and the elastic indentation stress-strain data. The variables correspond to those listed in Table 2

3.5 Defining Indentation Yield Strength with a Strain Offset for Metals

Indentation yield strength is a measurement of the elastic-plastic transition on the indentation stress-strain curve. Prior authors have relied on back extrapolation methods for determining the indentation yield strength [35-39], as seen in Figure 5. Such ad-hoc approaches are especially necessitated by the occurrence of pop-in events that mask the elastic-plastic transition in the ISS curves. In addition, the shape of the curve must be assumed (in most cases as linear) in order to extrapolate. However, for ISS curves without pop-ins, these requirements and assumptions are unnecessary. This is why an alternative approach using an offset strain was used to define the indentation yield strength for tests without pop-ins.

A small offset (a few tenths of a percent) is needed in order to provide a measure that is insensitive to indentation test parameters. A significant offset (more than a few tenths of a percent) defeats the purpose of trying to establish the initial flow stress as it would now be the flow stress at some equivalent strain. The back extrapolated yield strength and a 0.2% offset yield strength are very similar for a test without a pop-in (Figure 15). The choice of 0.2% was made for practicality; it has no direct link to a 0.2% offset on a uniaxial test, although the concept is the same. Using an offset eliminates multiple assumptions in determining the indentation yield strength for tests without pop-ins.

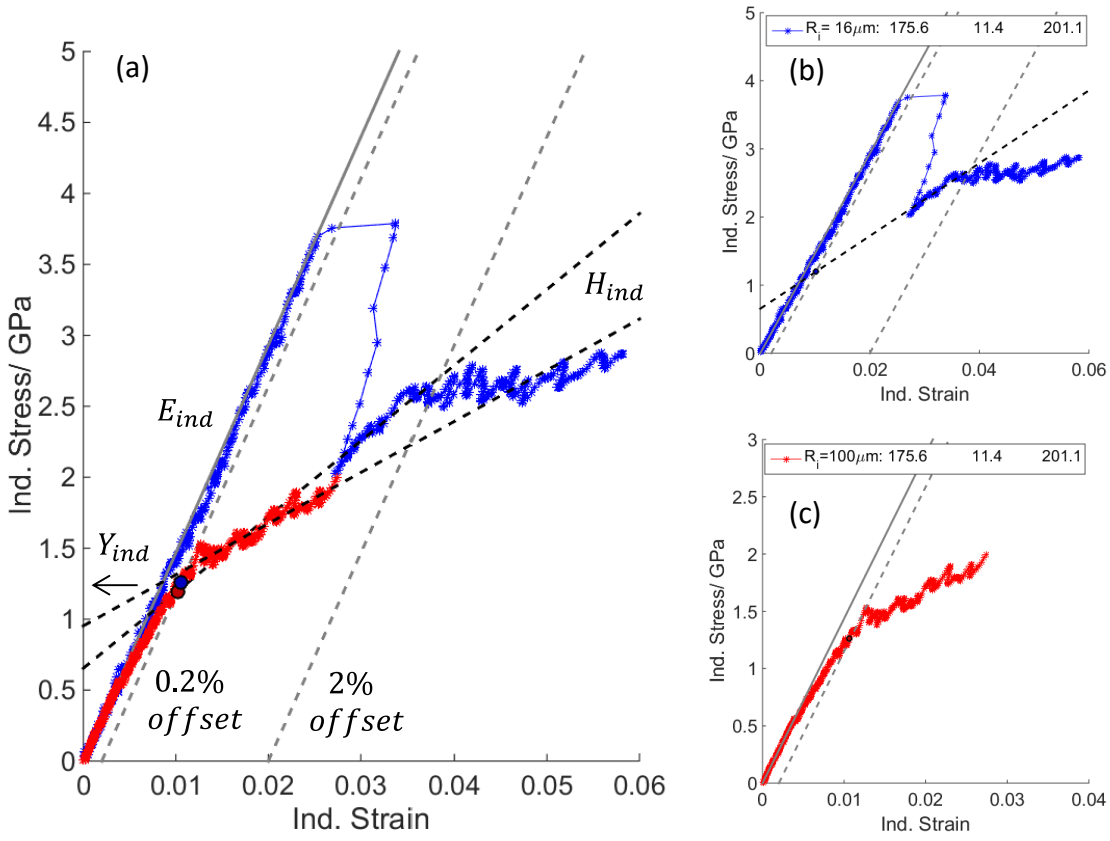

Figure 15: (a) Example of indentation stress-strain properties. Tests are from the same grain using a 16 µm (blue) and 100µm (red) radius indenter. The initial hardening slopes (H_{ind}) were determined inside a 2% strain offset, (b) The indentation yield strength (Y_{ind}) for the 16µm test was determined from back extrapolating the post pop-in ISS data to a 0.2% strain offset, (c) The indentation yield strength (Y_{ind}) for the 100 µm test was determined with a 0.2% strain offset.

The elastic-plastic indentation properties from the indentation stress-strain curve include: indentation modulus (E_{ind}), indentation yield strength (Y_{ind}), and the initial hardening slope (H_{ind}) as shown in Figure 15. In addition to these, the indentation stress at which the first pop-in occurs and the contact radius at yield can be recorded. These properties and measurements along with structure measurements at the indentation site will be used to quantify and understand the elastic and plastic anisotropy of the material as well as microstructure-property relationships.

Chapter 4

Microindentation Stress-Strain Protocol

One of the main purposes of this dissertation is to develop indentation protocols that span from nano to macroscopic length scales in order to mechanically characterize and understand hierarchical materials. The nanoindentation system used in this study has an maximum loading capacity of 10 N [79]. In order to perform indentation tests with larger tip radii on most alloys, a much higher loading capacity is required. For this reasons, a second indentation system was used to measure indentation stress-strain curves with 500 and 6,350 μm radii tips with maximum loading capacity of 2,500 N. Unfortunately, there is no CSM capability for such an instrument. The purposes of this section are to layout the developed protocols for measuring indentation stress-strain curves from an instrumented microindentation system without CSM and demonstrate the new protocols. This is the first extension of the nanoindentation ISS protocols to microindentation testing which has its challenges. As such, it makes sense to start out with a simpler material (aluminum) before moving to titanium alloys.

4.1 Zero-point Correction without CSM

The nanoindentation stress-strain protocols which capture the initial elastic and – elastic-plastic response of the material require the establishment of an effective zero-point. The same is true for microindentation stress-strain protocols; however, the ISS curve is far less sensitive to the zero-point correction. The reasons for needing an effective zero-point (e.g., surface or tip roughness) are likely to be reduced with a larger indenter radius.

Pathak et al. [55] explored determining the zero-point correction for nanoindentation without the CSM. The starting point for the protocol is the same, Hertz theory for a spherical indenter

$$P = \frac{4}{3} E_{eff} R_{eff}^{1/2} h_e^{3/2} \tag{4.1}$$

$$a = \sqrt{R_{eff} h_e} \tag{4.2}$$

$$\frac{1}{E_{eff}} = \frac{1-\nu_i^2}{E_i} + \frac{1-\nu_s^2}{E_s} \tag{4.3}$$

$$\frac{1}{R_{eff}} = \frac{1}{R_i} + \frac{1}{R_s} \tag{4.4}$$

Upon selecting the initial elastic segment, a linear regression analysis of Equation 4.1 can be performed to establish the effective modulus. Here the assumption of a correction is made in the form of

$$h = k(P - P^*)^{\frac{2}{3}} + C \tag{4.5}$$

$$k = \frac{3}{4} E_{eff}^{-\frac{2}{3}} R_i^{-\frac{1}{3}} \tag{4.6}$$

$$C = h^* \tag{4.7}$$

Following a similar protocol to [55], a number of possible load corrections, P^*, are evaluated. However, the displacement correction, h^*, is not left independent of the load correction. It is rather calculated as the y-intercept in the regression analysis. The optimal zero-point correction is one that minimizes the residual of the regression (e.g., log of the average absolute residual). In this process, the zero-point correction is automatically identified. In many cases, the zero-point correction turns out not to be needed (i.e., the correction is zero). This process is shown in Figure 16.

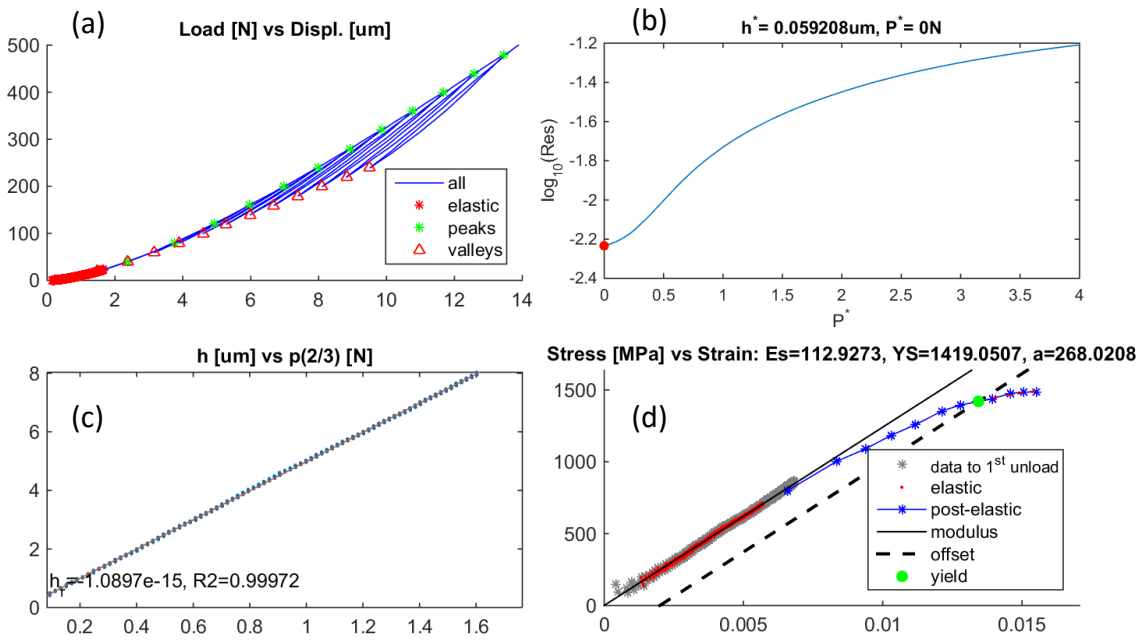

Figure 16: (a) Load-displacement curves with sequential unloads. Initial elastic segment highlighted in red. (b) Residual versus load correction to determine zero-point correction. (c) Linear regression of the initial elastic segment to measure the indentation modulus. (d) ISS curve. Data is from 6.35mm radius tip on Ti64.

4.2 Measuring Unloading Stiffness without CSM

The unloading stiffness is needed to estimate the contact radius and subsequent indentation stress and strain. In nanoindentation, this is accomplished from CSM which superimposes a small oscillatory signal (many unloads) on the monotonic loading sequence. In microindentation it is accomplished with sequential unloading (i.e., unloading at different load increments during a single test). Prior to the existence of CSM, this was the standard protocol for instrumented indentation testing in order to recover hardness and modulus as a function of depth or load at a single indentation site [30, 43]. The analysis used closely resembles the protocols of [31, 55]. Each unload is analyzed to produce a single point on the indentation stress-strain curve as follows

$$h = kP^{\frac{2}{3}} + h_r \qquad (4.8)$$

$$k = \frac{3}{4} E_{eff}^{-\frac{2}{3}} R_{eff}^{-\frac{1}{3}} \quad (4.9)$$

$$a = \sqrt{R_{eff}(h_{max} - h_r)} \quad (4.10)$$

$$\sigma_{ind} = \frac{P_{max}}{\pi a^2} \quad (4.11)$$

$$\varepsilon_{ind} = \frac{4}{3\pi} \frac{h_{s,max}}{a} \quad (4.12)$$

The subscript max denotes the displacement and load just before unloading. The effective modulus is assumed constant as determined from the initial elastic loading data at the beginning of test. This is a reasonable assumption since the deformation imposed is typically not large enough to cause severe damage (e.g., cracking) or rotation of the grains under in the indentation site. The definitions of indentation stress and strain are the same ones used for nanoindentation (i.e., indentation strain is determined from the sample displacement and not the total displacement). The main assumption in measuring the unloading stiffness is that the response is primarily elastic. To this end, the effect of sequential unloading on the response was experimentally studied

4.2.1 Understanding Hysteresis of the Unload-reload Cycle

Hysteresis is observed in the unload-reload cycle of the load-displacement curve during nano and microindentation testing, Figure 17. The hysteresis in these materials is not due to a phase change, viscoelastic behavior, or cracks forming since they are all ductile metals. Oliver et al. [43] examined the unloading behavior for nanoindentation measurements in detail for different materials with a sharp tip. For single grain nanoindentation measurements in pure metals, they concluded creep was the main culprit for inelastic unloading behavior, Figure 17a. This creep and hysteresis decreased with successive unloads leading to primarily elastic unloading behavior. The authors suggest a

basic rule of four unloads at a fixed point with the unloading stiffness determined from the final unload to minimize these effects. However, they also note that the unloading stiffness is not very sensitive to the choice of unload cycle (first, second, etc.). The unloading cycles for a spherical tip in CP Ti, Figure 17 b, show similar behavior to tungsten in that the unloading and reloading curves appear to only have a small shift during the load controlled holds at both ends of the loop. Spherical microindentation on CP Ti, Figure 17 c and d, shows a similar result to nanoindentation. It is the unloading and reloading curves of Ti64 and Ti18 that show a pronounced difference in shape, Figure 17 e and f. For microindentation on these materials, there is a clear ovalling of the loop.

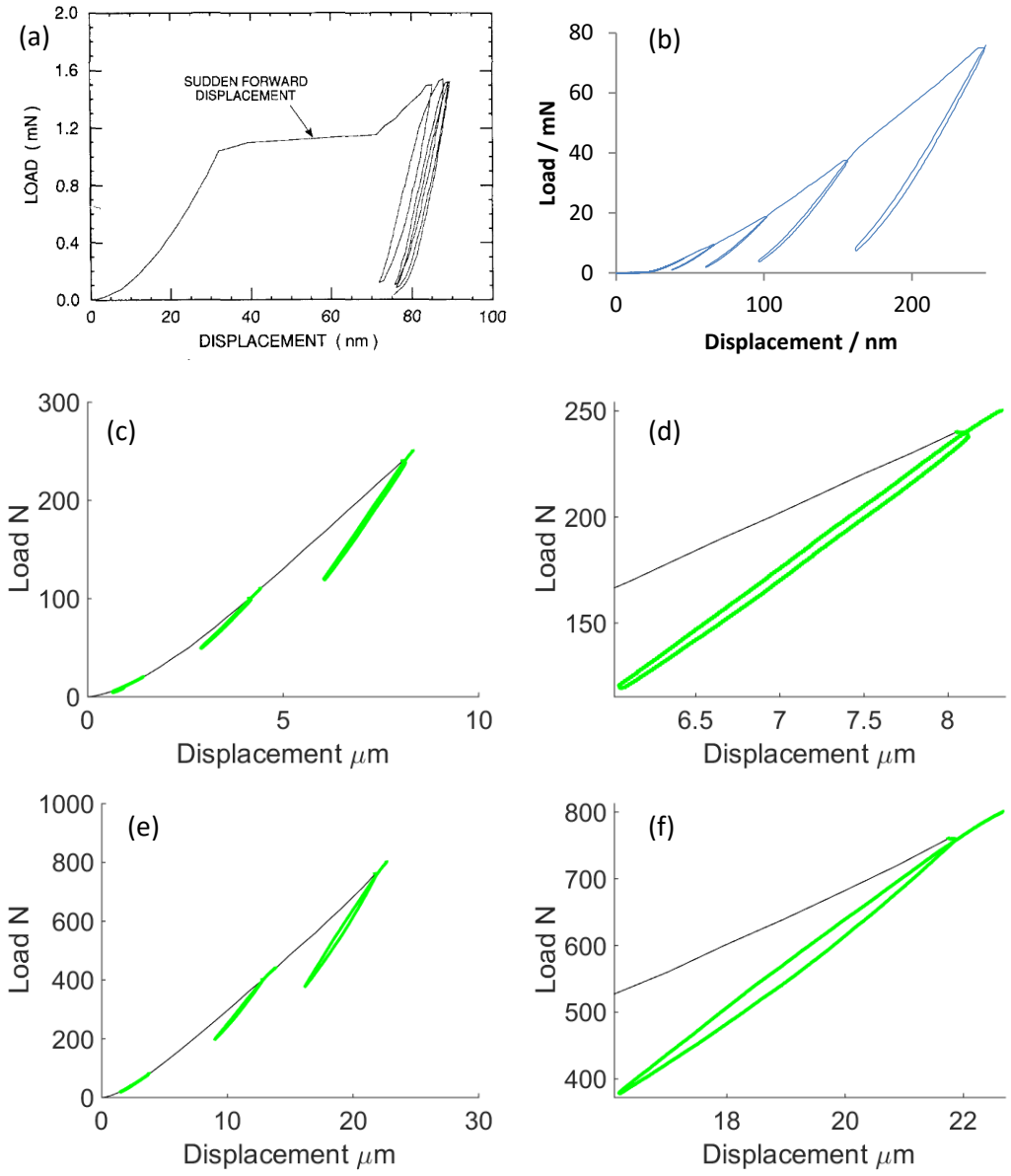

Figure 17: Cyclic load-displacement curves: (a) Berkovich tip on tungsten take from [43], (b) Spherical (100 µm radius) nanoindentation curve on electropolished CP titanium, (c-f) Spherical (6.35 mm radius) microindentation load-displacement curves for CP titanium (c-d) and Ti64 (e-f).

There are three possible explanations for the hysteresis observed in these microindentation tests: Bauschinger effect, friction, and non-uniform elastic recovery leading to a small amount of localized plasticity. The first two explanations would cause significant problems in the application of Hertz's theory to the analysis of unloading

curves (e.g., unloading is completely elastic and contact is frictionless). The last explanation also poses a contradiction to using Hertz's theory; however, it will be shown that the effects are mostly negligible. The support for the explanation that the hysteresis in the unload-reloading cycle is caused by the irreversibility of dislocation movement (Bauschinger effect) comes from indentation simulations using kinematic hardening [88-90]. The hysteresis loops can be replicated with a kinematic hardening model; however, the material behavior associated with it does not make complete physical sense. In the model, during the final stage of unloading, the material has to go through plastic deformation to get back to a completely unloaded state. It is unlikely that this is the case in the experiments, and the hysteresis loops shown in this work occurred without complete unloading (partial unloading to 50% of the peak force was used). Addressing the second explanation (i.e., friction), Johnson [53] estimates the energy loss for elastic loading and unloading cycles to be 0.4% caused by a small amount of material at the edge of contact that sees some stick and slip (friction and interfacial slip). Such a small amount of energy loss would not make a measureable difference in the loading-unloading curve. It is unlikely that the Bauschinger effect or friction is the reason for the hysteresis.

Rather, it can be reasoned that during unloading of a heterogeneous indentation site the elastic recovery in the primary indentation zone does not happen uniformly in all features (e.g., grains, phases) which causes a small amount of localized plasticity. In the case of Ti64 and Ti18, there are two phases with different elastic and plastic properties. For indentation of such microstructures, during unloading the initial contribution to the recovery will be greatest from the stiffest and largest feature. As unloading continues, the contributions become more proportional or uniform between the features in the

indentation site. Upon reloading, the same dominant feature will contribute to the response more than other features. With further reloading the contributions of features in the indentation zone become more uniform. This would explain why the final unloading and initial reloading slopes are the point where there seems to be greatest difference in the stiffness (dP/dh) as well as at the top of the loop. For microindentation of CP Ti, the indentation site contains many grains so that there is no dominant feature. In the explanation above, the unloading stiffness may change during unloading since the material elastically recovers non-uniformly with a small amount of localized plastic deformation. A large section of the unloading curve (95 to 50% of the peak force) is used to determine the stiffness. With this approach, the unloading stiffness is less sensitive to small events of localized plastic deformation. The unloading curves also exhibit a linear h versus $P^{2/3}$ relationship in accordance with Hertz's equation. Furthermore, it will be demonstrated the there is no substantial effect on the ISS response due to sequential unloading. The assumption that the microindentation unloading behavior of titanium alloys is assumed to be primarily elastic and analyzed using Hertz's equations.

4.2.2 Effect of Sequential Unloading on the ISS Curve

Field and Swain experimentally studied the effects of sequential unloading (i.e., partial unloading) versus a continuous loading test on the load-displacement curve [30]. They found it was negligible. However, it is not clear if this has an effect on the indentation stress-strain response. To experimentally quantify this effect, there different test sequences were used: one with the full amount of sequential unloading, one test continuously loaded to half the maximum load of the previous test followed by a partial unload, and one test continuously loaded to the maximum load of the first test followed

by a partial unload. Each test was conducted at a different indentation site; however, the indentation moduli were in close agreement minimizing the scatter due to the different indentation sites. The indentation stress-strain curve for tests 2 and 3 produces only one plastic stress-strain point. The results can be seen in Figure 18 which shows no significant effects from sequential unloading on the indentation stress-strain response of the material. This supports the assumption that unloading is primarily elastic, and therefore has no effect on the material response measured in the load-displacement and indentation stress-strain curve.

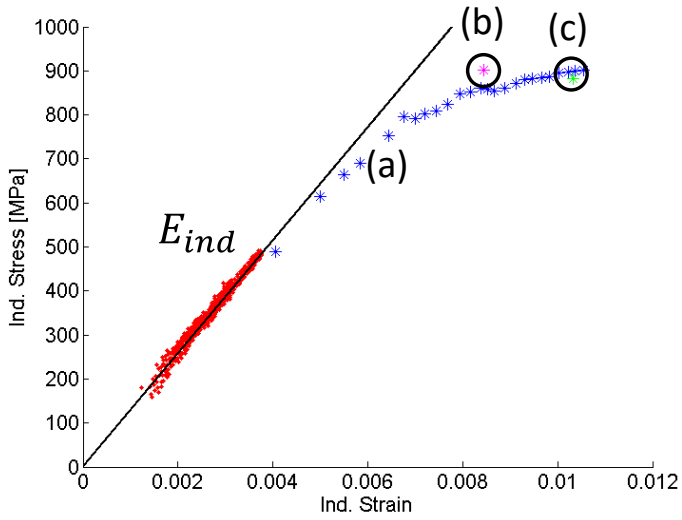

Figure 18: Indentation stress-strain curve for three test sequences. (a) 25 sequential unloads in order to recover a complete ISS curve, (b) A continuous load sequence until half the maximum load used in (a) followed by an unload, (c) A continuous load sequence until the maximum load used in (a) followed by an unload. The data comes from a 6.35 mm radius tip on CP Ti.

4.3 Micro-ISS Test Case on Al-6061

A case study was done to evaluate the ability of the microindentation stress-strain protocol to measure the initial elastic and elastic-plastic response of a polycrystalline indentation site. Al-6061 was chosen because it has a well-known Young's modulus and can be easily heat treated to vary the uniaxial yield strength. A rolled plate of Al-6061

(as-received (AR) condition) was sectioned and heat treated at 204, 274, 343, and 413 °C for 2 hours followed by a water quench to produce samples with different uniaxial yield strengths. Samples were ground and polished down to 0.06 μm colloidal silica for indentation testing and metallography. It is still important to prepare samples that are free of a distributed surface layer similar to nanoindentation samples. In addition, microindentation samples typically must be much larger with both faces (front and back) polished parallel to obtain good results. The grain size and initial weak texture in the Al-6061 material remained the same between heat treatments. The change in the material structure between heat treatments was the relative fraction and type of Mg_2Si precipitates which has a strong effect on hardness and strength [91-93]. Indents were done on each condition along the normal direction (ND) of the sheet and uniaxial tension along the rolling direction (RD). Representative indentation load-displacement and indentation stress-strain curves for each condition are shown in Figure 19. ISS curves show clear differences in strength which correlate well with the difference in uniaxial strength. The average Young's modulus for all conditions determined from indentation measurements was 69.5 ± 2.94 GPa which is in good agreement with the value of 70 GPa determined from uniaxial tests. It can also be seen that the indentation site contains multiple grains and is no longer a single grain measurement, Figure 19. These findings are critical for proceeding to more complex alloys (e.g., titanium alloys) which show higher elastic anisotropy and contain a variety of microstructures. More details of this study are can be found in [94].

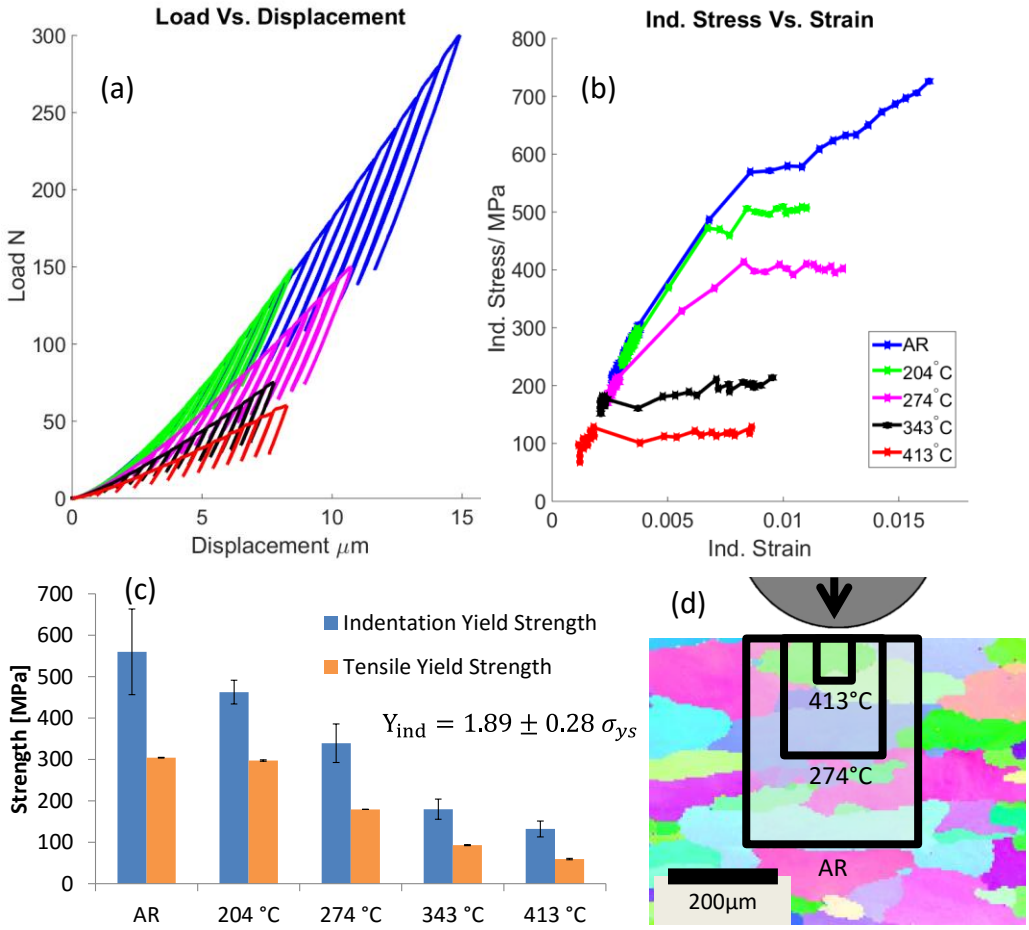

Figure 19: (a) Load-displacement curves for 5 different Al-6061 conditions, (b) Corresponding ISS curves, (c) Indentation and uniaxial yield strength measurements for all five conditions, and (d) The primary indentation zone overlaid on a representative micrograph.

Chapter 5

Nanoindentation of Commercially Pure Titanium

5.1 Methods and Materials

A commercially pure (grade 2) bar of titanium from McMasterCar was heat treated at 800°C for 2 hours in air and allowed to furnace cool to room temperature. This was done to anneal the material and grow the grain size to make indentation measurements with 16 and 100μm radii indenter tips inside individual grains possible. In order to overcome the texture in the original material and survey a variety of grain orientations, two different samples were sectioned with different orientations relative to the sample dimensions. The thinnest dimension of the bar was designated the normal direction (ND) and the long direction of the bar was designated the rolling direction (RD). One sample was oriented with the indentation plane parallel to the ND which had a basal texture, and the other sample was oriented for indentation along the RD. Micrographs of the ND samples are show in Figure 20. Careful sample preparation was done to ensure that the indentation surface was free of deformation and any oxidation from the heat treatment. This was accomplished with careful sectioning, grinding, and polishing to remove a total of few millimeters of material followed by electropolishing. A perchloric acid based electrolyte (354mL Methanol, 210mL 2-butoxyethanol, 36 mL Perchloric Acid) was chilled to -20°C for electropolishing at a constant voltage between 20-25V and a time of 0.5 to 5 mins. The final surface had a mirror like finish with the grain boundaries and Fe impurities etched.

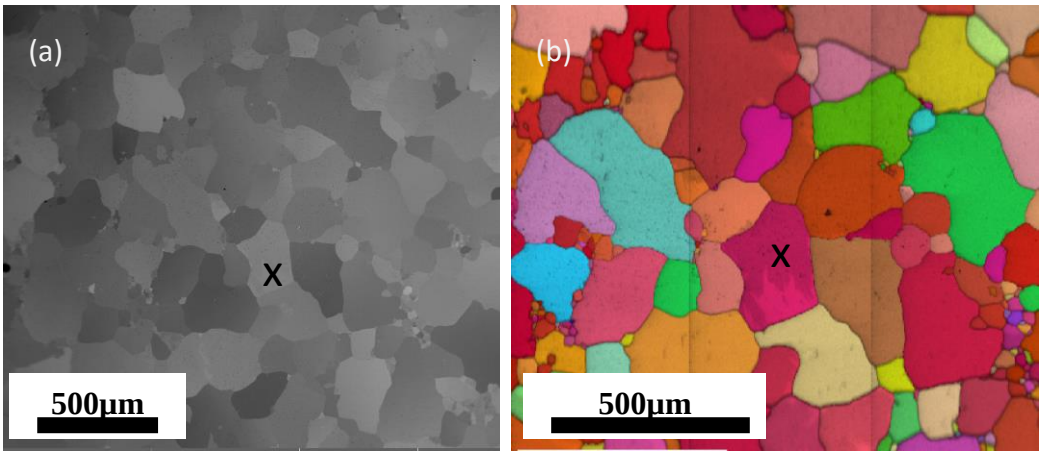

Figure 20: (a) SEM-BSE micrograph and (b) EBSD inverse pole figure map. The X marks the same grain in both micrographs for comparison. The images come from an electropolished surface.

An Agilent G200 Nanoindenter with an XP head and CSM were used to perform indentation tests with conical-spherical diamond tips having nominal radii of 16.5 and 100 µm. The manufacturer specified radii were confirmed with SEM images from multiple side profiles of the tip. Two indenter sizes were used in order to determine if there are any size effects on the ISS response in titanium. The test method used was the standard method for the continuous measurement of modulus, hardness, and tip calibrations; however, the analysis was done posttest using the protocols of [31] with the improvements outlined in Chapter 3. The indentation test parameters included a CSM amplitude and frequency of 2nm, 45 Hz, a final displacement of 300 nm (16µm radius indenter) and 400-500 nm (100 µm radius indenter), and a constant loading rate normalized by the load (effective strain rate for Berkovich tips) of 0.05 /s. The last test parameter yields a relatively constant indentation strain rate and allows the sample to be slowly loaded. The relatively small indentation depths reflect an emphasis on the initial elastic and elastic-plastic response of the material before significant plastic deformation occurs under the indenter. Indents were placed well away from grain boundaries to

eliminate the effects of surrounding grains. Grain orientations at the indentation site (single average orientation per grain) were determined prior to indentation using an EDAX Hikari EBSD detector with TSL OIM Analysis and a Tescan Mira XMH field emission SEM. The indentation properties and measurements were correlated with the crystal orientation at the indentation site.

5.2 Results

5.1.1 Elastic Anisotropy

The elastic constants of commercially pure titanium are widely accepted from Simmons and Wang [77]. Capturing the initial elastic contact is critical for ISS protocols and so emphasis is placed on indentation modulus measurements. CP Ti serves as a benchmark for extending the nanoindentation stress-strain protocols to an hcp material. The crystal Young's modulus only depends on the second Bunge-Euler angle or declination angle (Φ) of the c-axis with respect to the test direction due to the axial symmetry about the c-axis for elasticity. The indentation modulus (E_{ind}) determined from 16 and 100 μm radii indenters is plotted against the crystal declination angle in Figure 21. From FEM simulations using the elastic constants for pure Ti [77], the predicted indentation modulus can be determined. Indentation measurements for both indenter sizes (16 and 100μm) radius are in good agreement with each other and the predicted indentation modulus. There is some disagreement with the prediction at high and low declination angles.

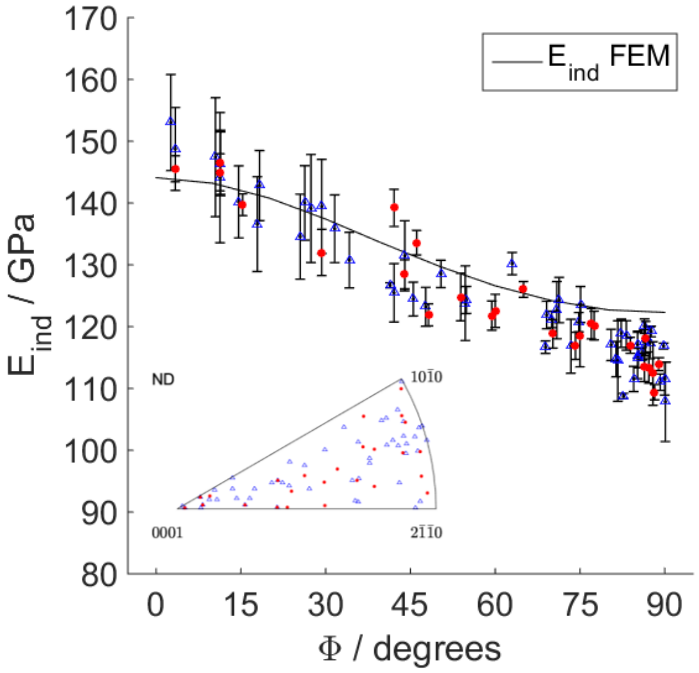

Figure 21: Indentation modulus (E_{ind}) versus declination angle (Φ) measured from 16 µm radius (blue) and 100 µm radius (red) indenters on CP Ti. The expected indentation modulus (E_{ind} FEM) is determined using single crystal elastic constants from literature[77] in FEM simulations courtesy of M. Priddy. Error bars are ± one standard deviation which incorporates multiple answers for single tests and multiple measurements in the same grain when applicable. There are approximately 25 grains (35 tests) and 50 grains (74 tests) for the 100 and 16µm radius indenters respectively.

5.1.2 Plastic Anisotropy

The orientation dependence of the indentation stress-strain curve for 16 and 100 µm radii indenters can be seen in Figure 22 and Figure 23. Pop-ins are present in the 16 µm radius indenter tests which decrease significantly in the 100 µm radius indenter. This is due to the inherent size effect of pop-in events [68], and the change in the size of the primary indentation zone at yield between indenter tips. A plot of the indentation stress at which the pop-in occurs for both indenter sizes (Figure 24), supports the trends seen in the selected ISS curves. A clear orientation dependence on the pop-in stress is observed for a 16 µm radius indenter. A decrease by 2-3 times occurs as the crystal is declined from 0 to 45°. The contact radius at the indentation yield point is shown in Figure 25 and

changes from 500 nm to 2.25 µm with the different tip sizes. The contact radius at yield is about 2-3% of the indenter radius. The primary indentation zone at yield [31] can be estimated as a cylinder with dimensions (diameter and height) of 1 and 1.2 µm for the 16 µm tests and 4.5 and 4.7 µm for the 100 µm test, respectively.

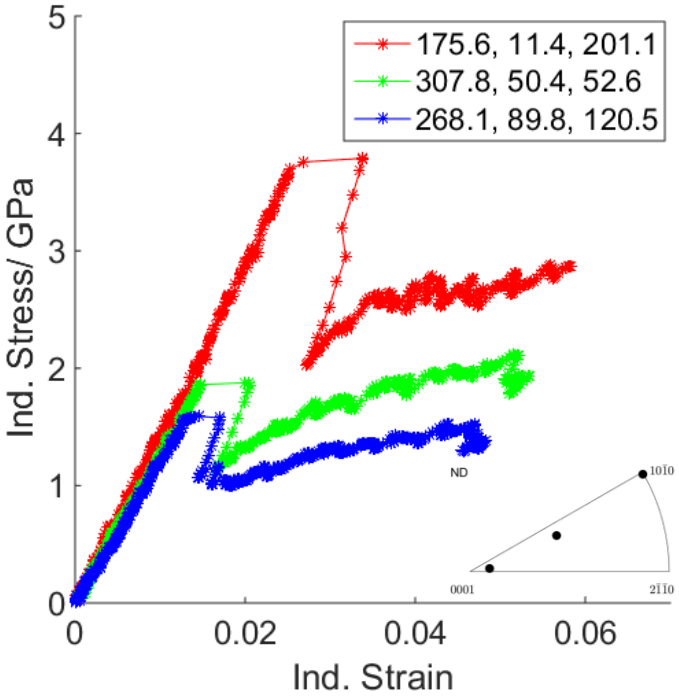

Figure 22: ISS curves for select orientations measured with a 16 µm radius indenter. The Bunge-Euler angles are given in the legend for each test.

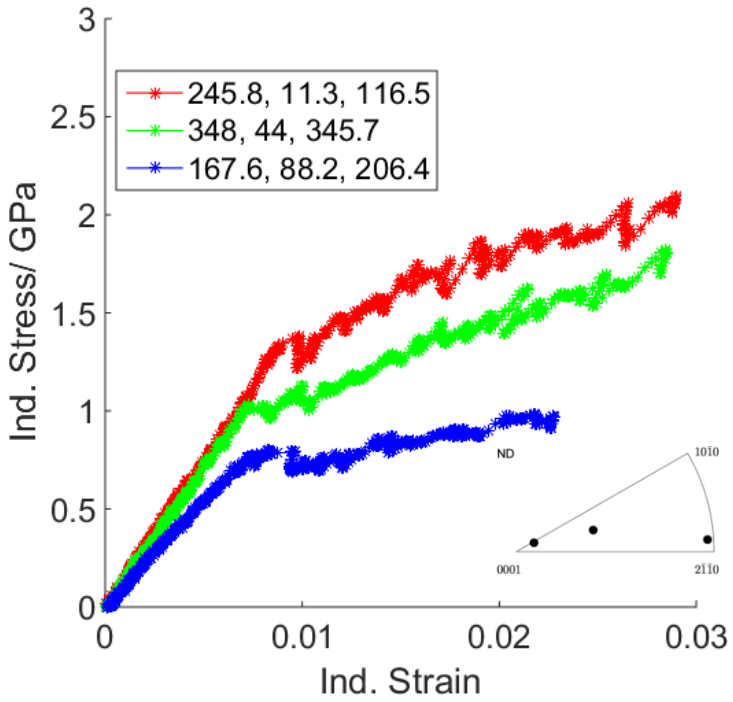

Figure 23: ISS curves for select orientations measured with a 100 µm radius indenter. The Bunge-Euler angles are given in the legend for each test.

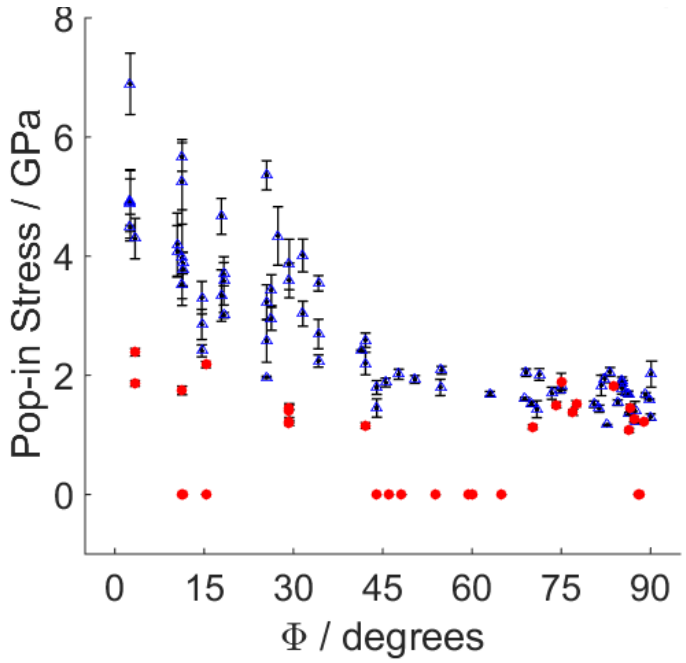

Figure 24: Pop-in stress for each test for 16 (blue) and 100 (red) µm indenter sizes versus declination angle.

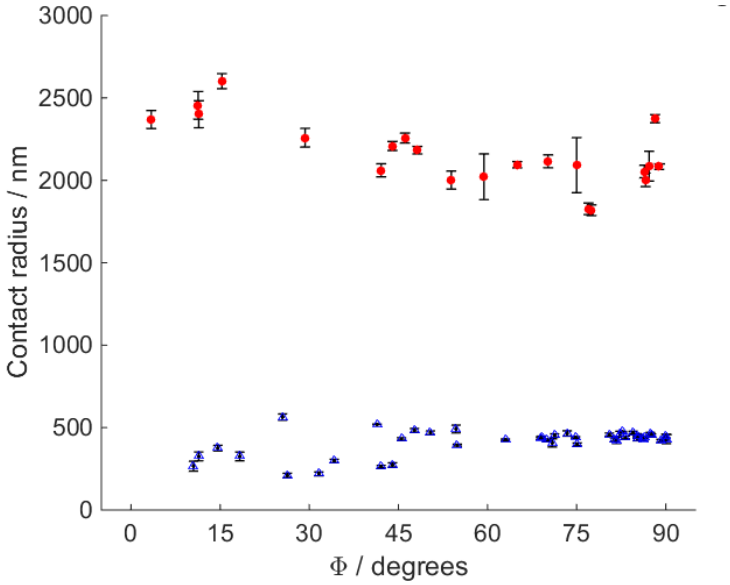

Figure 25: Average contact radius at yield for 16 (blue) and 100 (red) µm indenter sizes versus declination angle.

The main purposes for using two indenter sizes on CP Ti was to understand the reliability of estimating indentation yield strength from back extrapolation methods on tests with pop-ins and understand if there is a size effect on the indentation yield strength. Figure 26 a and b shows the ISS curves for 16 and 100 µm radius indenters measured in the same grain for two different orientations. The ISS curves agree where there is overlap and trends in the same directions where there is no overlap. The pop-ins in the 16 µm radius indentations mask the elastic-plastic transition. However, it appears that both indenter sizes would measure the same indentation yield strength if pop-in events could be negated. In other words, the only size effect is on the pop-in and not the indentation yield strength estimated from back extrapolation. As such, the indentation yield strength describes the material if the minimum number of dislocation sources were present to avoid a pop-in event. It also appears that in order to estimate the yield strength for tests with pop-ins, the back extrapolation has to come from data before 0.020 - 0.025 indentation strain. The indentation yield strength for both indenter sizes was determined

using a 0.2% offset and the above mentioned guide for back extrapolation for tests with pop-ins, Figure 27. Tests with very large pop-ins that provided too little data for extrapolation were not used for determining indentation yield strength. The strongest trend in indentation yield strength is again with the crystal declination angle showing the highest strength for grains indented along the c-axis and a minimum approaching orientations completely declined. No significant trend is observed between grains indented along $\{\mathbf{10\bar{1}1}\}$ and $\{\mathbf{11\bar{2}1}\}$. One approach to fitting the orientation dependence of indentation yield strength is to use generalized spherical harmonics (GSH) which are often employed to describe orientation distribution functions of polycrystalline materials with known symmetries. This was used to interpolate between indentation data points in the orientation space by Vachhani et al. [39]. Figure 28 is the result of such a regression fit and the subsequent contour plots in the IPF triangle. The regression fit captures the overall trend well; however, there is some clear scatter in the data points with regard to the fit. Lastly, initial indentation hardening slopes were calculated for tests with both indenter tips, Figure 29. There is strong trend in the hardening slopes with orientation. The 100 μm radius indenter tests appear to have higher hardening slopes than 16 μm radius indenter tests, and the 16 μm radius indenter tests have a lot of scatter approaching the c-axis.

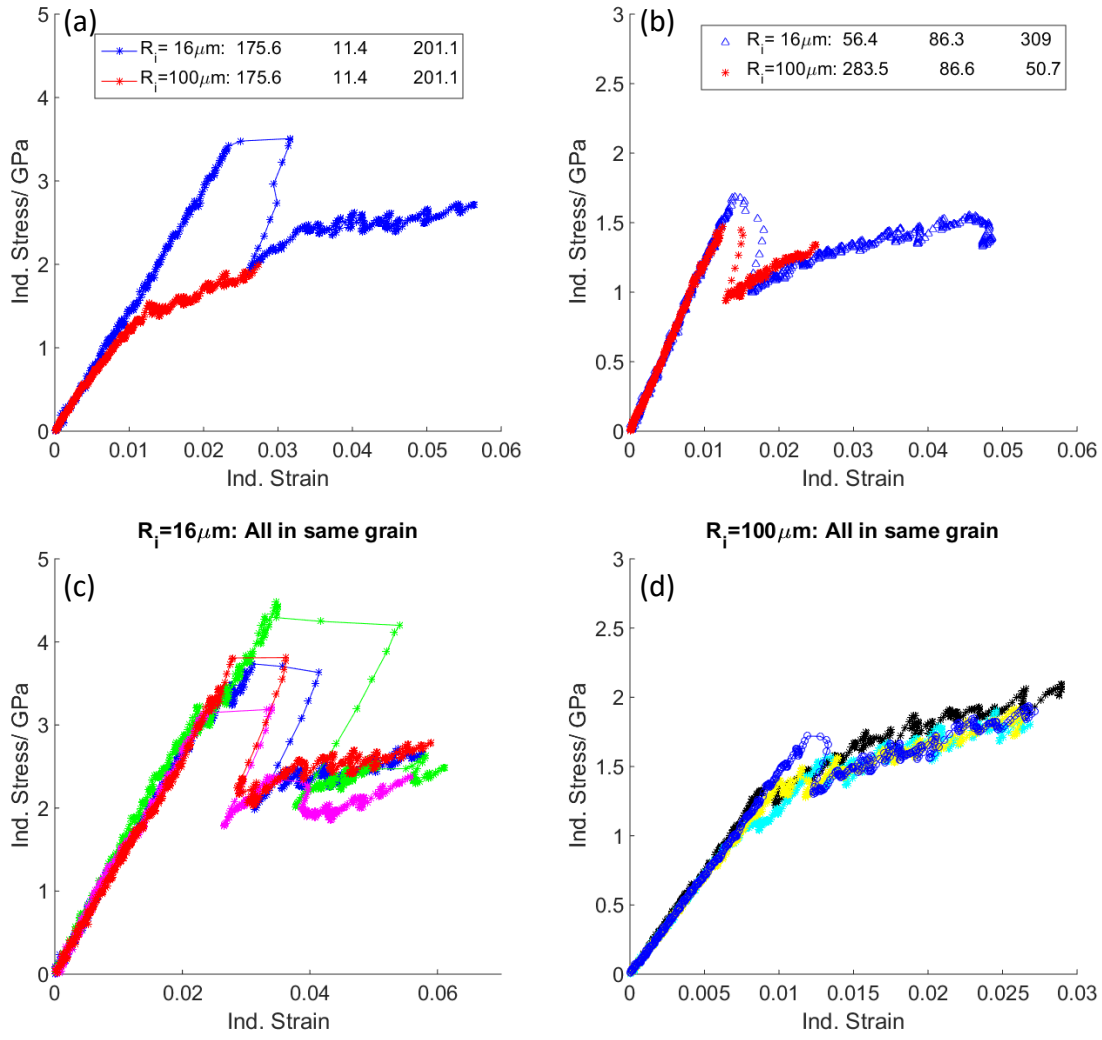

Figure 26: (a-b) Comparison of ISS curves for 16 and 100 µm radius indenters for orientation near and far from c-axis, respectively. (c-d) Comparison of ISS curves in the same grain for 16 and 100 µm radius indenters. The orientation for (c) and (d) is 245.8, 11.3, 116.5 (same grain).

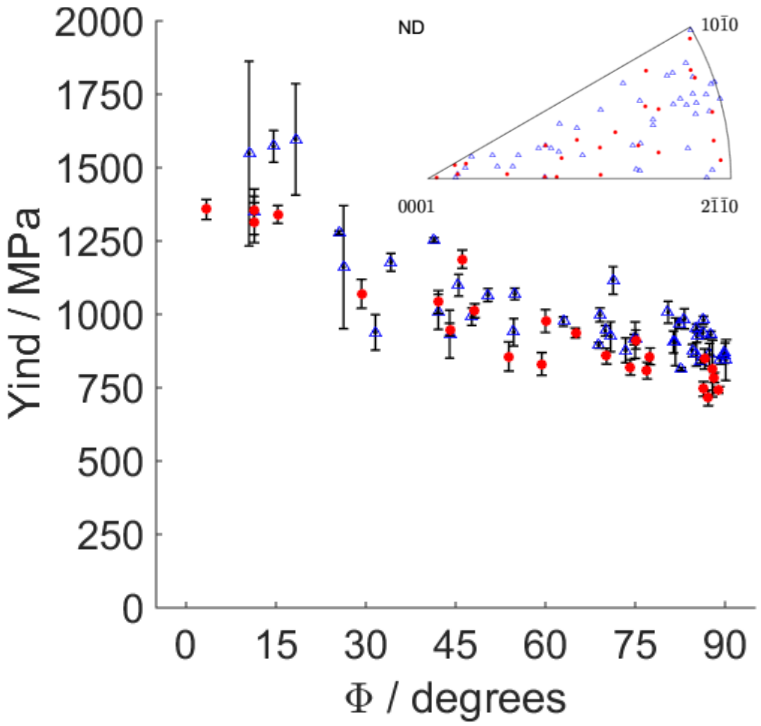

Figure 27: Indentation yield strength versus declination angle for 16 (blue) and 100 (red) µm radius indenters.

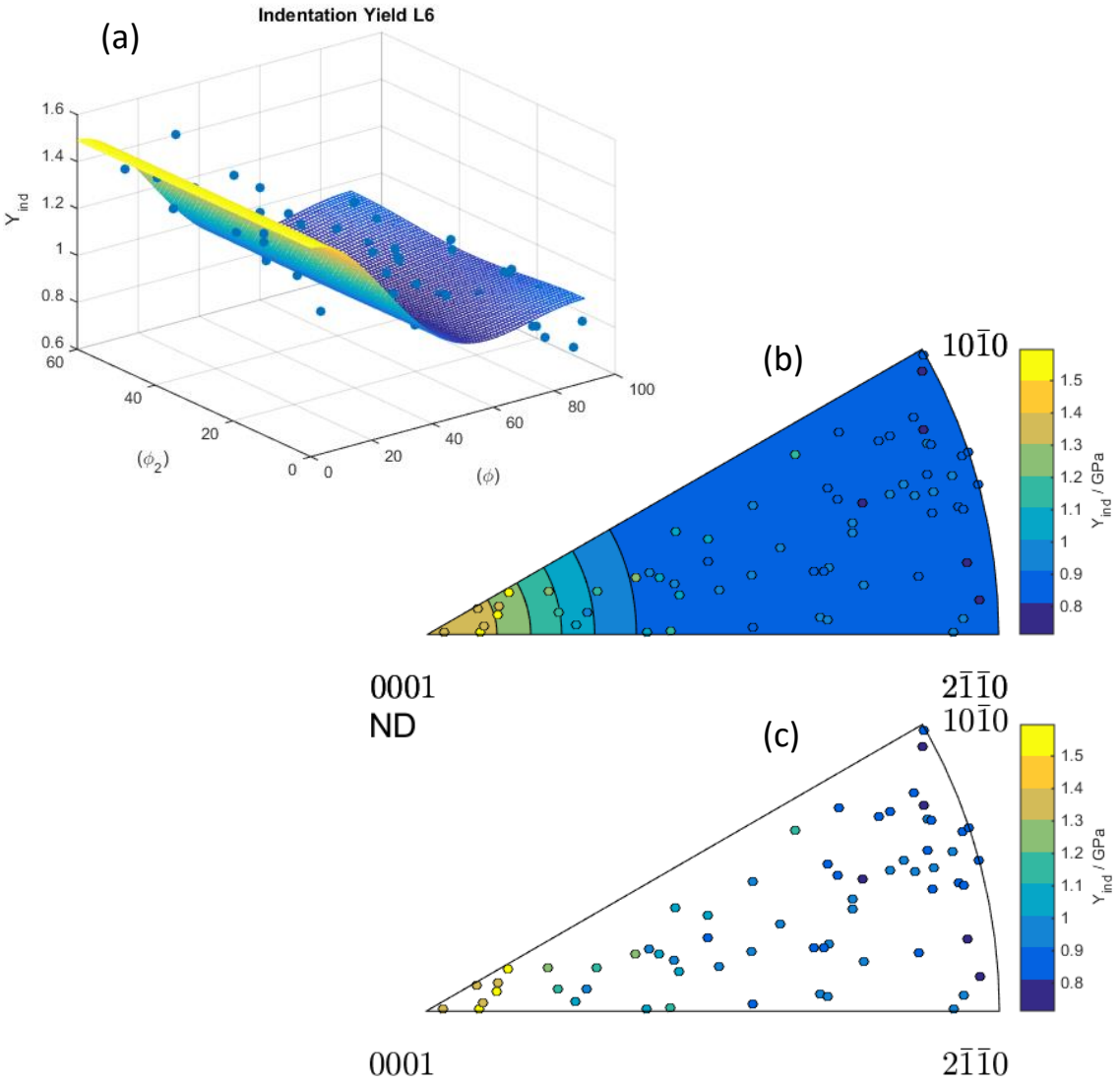

Figure 28: (a) GSH regression fit for indentation yield strength in the indentation orientation space (Bunge-Euler angles ϕ_2, φ) courtesy of D. Patel, (b) IPF contour plot for indentation yield strength. Background contour determined from regression fit. Data points are colored according to their actual values, (c) IPF contour plot without regression fit. Data includes 16 and 100 µm radius indenters.

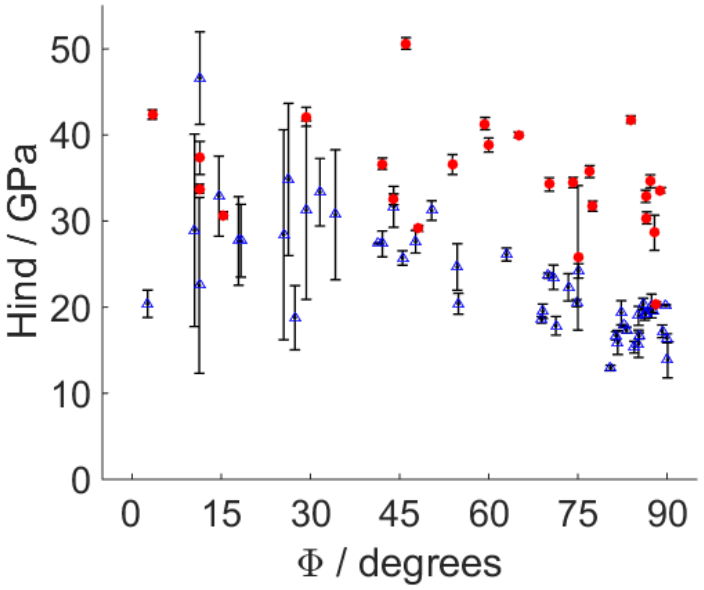

Figure 29: Indentation initial hardening slope versus declination angle for 16 (blue) and 100 (red) μm radius indenters. A linear regression was used on data between the indentation yield point and indentation strains up to 0.020-0.025. A moving average was applied to the data before the fit to decrease the sensitivity of the fit to the jagged nature of the hardening behavior.

5.3 Discussion

5.3.1 Elastic Anisotropy

Pure titanium was also chosen for demonstrating the protocols in this dissertation in part because there is a lot of available literature on the nanoindentation of individual grains using [95-99]. Berkovich indentation measurements show less agreement with the expected elastic anisotropy and appear to be inconsistent. Mante et al. [95] tested two orientations (basal Φ=0° and pyramidal Φ~60° planes) of single crystal Ti (99.999%) and a polycrystalline Ti control sample which all showed similar moduli (~125 GPa). Merson et al. [99] tested a wide range of orientations in a polycrystalline CP Ti with a Berkovich tip and also reported no trend in modulus with orientation. Britton et al. [96] similarly tested a range of orientations for grade 1 CP Ti with a Berkovich tip, but reported a trend of modulus with orientation: 145-130 GPa with the highest value for indents approaching

the basal plane (Φ=0). Their results also show a variation of ~10% for orientations with similar declination angles. More recently, Fizanne-Michel et al. tested a variety of orientations in grade 2 CP Ti with Berkovich and spherical tips and reported a range of 140-110 GPa for Berkovich indentation and a range of 175-115 GPa for spherical indentation with no trend with orientation [98]. Two things stand out from this survey of literature. Firstly, there are clearly conflicting reports about the degree of elastic anisotropy from Berkovich indentation measurements. Secondly, the trend reported by Britton et al. [96] shows less anisotropy than the measurements reported here. Conflicting reports and relatively smaller trends reported in literature are a direct result of the test protocols used. Berkovich (sharp) tip indentation plastically deforms the material almost immediately and causes significant deformation with increased indentation depth. This means the material at the indentation site is no longer virgin material (i.e., crystal rotation has likely occurred for a significant volume of material), and the response is from a deformed indentation zone. This would explain why some authors report no trend [95, 98, 99] and Britton et al. [96] reports a weaker trend compared to the dependence of indentation modulus on orientation that is reported here.

Fe-3%Si has been the only other elastically anisotropic material to be characterized using the same spherical nano-ISS protocols [31]. It has a much higher anisotropy (Young's modulus ranges from 120 to 250 GPa) [37, 62]. The elastic anisotropy of CP Ti is particularly challenging to characterize because it is relatively small (100 to 145 GPa), yet significant that it cannot be ignored as in pure aluminum [39] or tungsten [31]. From the scatter of some individual measurements and multiple measurements with similar declination angles, it is apparent that the accuracy of the

sample modulus is around 10% (10-15 GPa) for materials with similar elastic anisotropy to titanium. However, these results are promising for studying titanium alloys such as Ti64 which have high volume fractions of α-Ti and similar elastic properties.

5.3.2 Plastic Anisotropy

There are some conflicting trends reported in literature regarding the orientation dependence of hardness. Zambaldi et al. [97] report a hardness range of 1 to 0.75 GPa for grade 2 CP Ti for increasing declination angles from 0 to 90°, respectively. Merson et al. [99] report a higher hardness range of 2.73 to 1.34 GPa for the same dependence on declination angle for CP Ti. Britton et al. [96] report an even higher range of 5.5 to 4.4 GPa for the same dependence on declination angle but for grade 1 CP Ti. Mante et al. [95] tested two single crystal orientations of high purity titanium and reported the opposite trend: 1.60 GPa (Φ=0°) and 1.87 GPa (Φ~60°). Lastly, Fizanne-Michel et al. [98] reported a mean hardness of 2.9 GPa for grade 2 CP Ti. The differences in range for grade 2 CP Ti are likely due to different test conditions (i.e., maximum load, depth, etc.). Changes in these test conditions will result in different flow stress-measurements until the strain hardening of the material under the indenter saturates. For this reason it is difficult to use hardness in a quantitative sense and compare measurements made with different test conditions. Even more alarming is the conflicting results between grades 1 and 2 CP Ti. Oxygen has a strong effect on the yield strength of pure titanium which can increase from 170 to 275 MPa for oxygen content going from 0.18 wt.% (grade 1) to 0.25 wt.% (grade 2), respectively [74]. Due to the increase in oxygen content, hardness measurements on grade 2 CP Ti should be larger than grade 1 CP Ti. However, the

reported values of Britton et al. [96] for grade 1 CP Ti are about twice as much as the values reported for grade 2 CP Ti.

The overarching trends in hardness measurements for different grain orientations are also seen in indentation yield strength measurements in Figure 27. The increase in indentation yield strength with decreasing declination angle can be understood by considering the orientation of different slip systems and their resistances. There is general agreement in literature that all three slip systems (basal, prismatic, and pyramidal) are active during indentation regardless of orientation despite the much higher resistance of pyramidal $\vec{c} + \vec{a}$ slip [96, 97, 99]. This makes sense given the highly heterogeneous stress state imposed by the indenter, especially with Berkovich tips. However, certain orientations are more favorably oriented for different slip systems. Using the Schmid factor for different orientations as a way to roughly estimate the levels of slip activity on different slip systems (indentation is not a uniaxial stress-strain) reveals that for the extreme orientation of Φ=0°, $\vec{c} + \vec{a}$ type slip is predominantly needed. It is therefore not surprising that the highest indentation yield strength is measured for orientations with the c-axis parallel to the indentation direction. Moving away from the c-axis reduces the indentation yield strength because $\vec{a}$ type slip which has lower resistance is available. The minimum in indentation strength appears to be at Φ=0° for which prism $\vec{a}$ slip is more favorably orientated than basal $\vec{a}$ slip. This supports the literature which finds prismatic slip as the principal slip system with the lowest resistance in CP Ti [96, 97, 100, 101].

A more specific analysis of the slip systems to indentation was developed by Li et al. [102] in the form of an indentation Schmid factor. The indentation Schmid factor is

defined as the maximum resolved shear stress on a given slip system over the contact pressure [102].This requires solving the anisotropic elastic contact equations to determine the stress fields for different crystal orientations. Thus the indentation Schmid factor will depend on the elastic constants and anisotropy. Indentation Schmid factors using elastic constants for Ti-6wt%Al [103] were calculated by Kwon et al. [104]. These will be discussed in more detail for indentation experiments on α-Ti64. However, the indentation Schmid factors for extreme orientations agree well with the statements made using the uniaxial Schmid factor. Namely, indents along the c-axis likely activate pyramidal $\vec{c} + \vec{a}$ and indents on fully declined crystals active prism slip.

Twinning readily happens during uniaxial compression and tension of pure titanium [105-108]. In polycrystalline materials, the stress required to produce twins increases with decreasing grain size [106, 107, 109]. Therefore, it is likely that the stress required to produce twins in small volumes of material is higher than polycrystalline samples. Twinning has been observed in micropillar compression tests of single crystals [110-112]; however, it also shows a size effect. Twinning deformation in Ti5Al (5 wt.% Al) subsides when the pillar size becomes less than 1μm [110, 112]. Comparing this size to spherical nanoindentation tests in this work, the widths of the primary indentation zone [31] (also the width of a cylinder) for indents on CP Ti were around 1μm and 4.5 μm. There was little difference with indenter size on the indentation yield strength; therefore, a width of 4.5 μm can be used to compare to the micropillar experiments. Additionally, pure titanium was indented which twins more readily than alloyed titanium (5-6 wt.% Al) [74, 113]. Despite the higher likelihood of twinning in these experiments compared to micropillar tests due to size and composition, no twins were observed on the surface at

indentation sites. Figure 30 shows BSE micrographs of indentation sites for three different orientations (near c-axis, partially declined, and fully declined) with the 100 µm radius indenter on CP Ti. The deformation that appears on the surface outside the impression appears to line up with prismatic planes of the crystal and is likely due to prism slip.

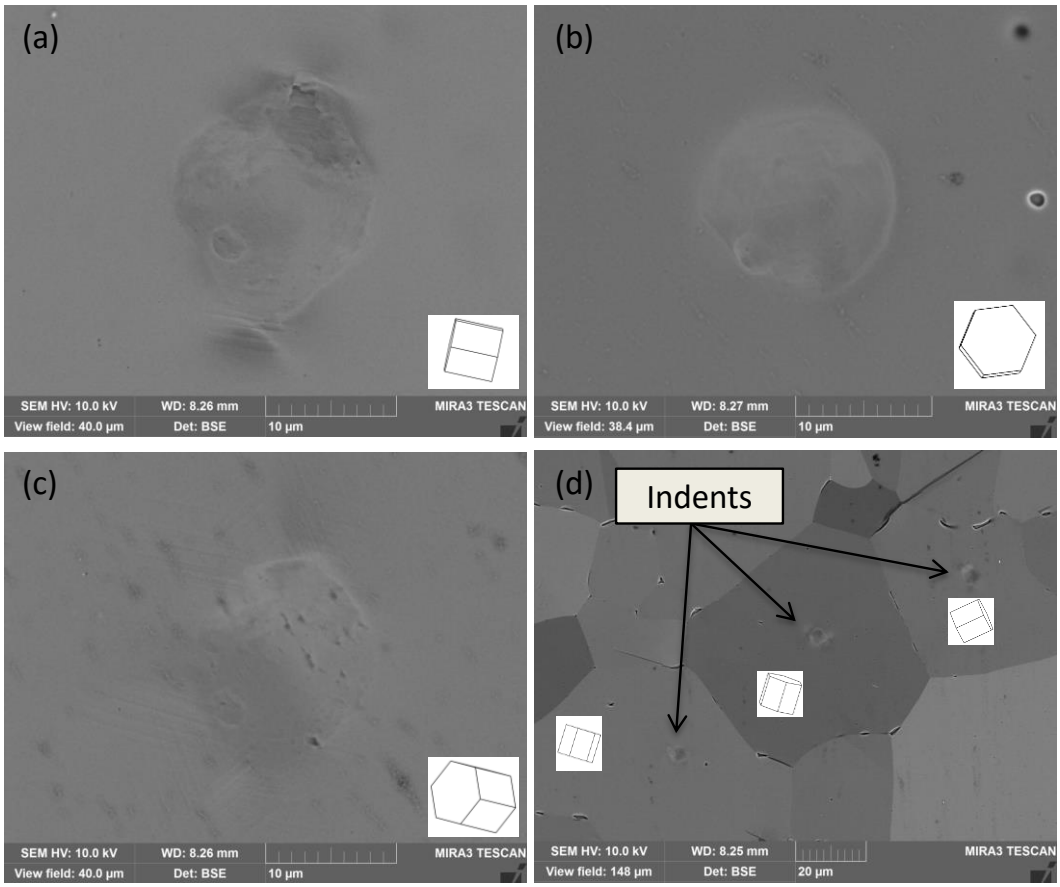

Figure 30: (a-c) BSE images of 100 µm radius indents on CP Ti ND sample with crystal lattice orientation top view shown in the lower left hand corner, and (d) BSE image of 16 µm radius indents on CP Ti RD sample. The Bunge-Euler angles in degrees for (a-c) are [167.6, 88.2, 206.4], [59.2, 3.4, 278.1], and [166, 42.1, 209.3], respectively.

In fact, no nanoindentation studies on pure or alloyed α-Ti provide any convincing evidence that twinning occurs. The only report of a twin was by Kwon et al [104] in alloyed titanium for cross-sectional TEM of an indent on a fully declined

orientation. However, the main evidence for the observed feature being a twin was based on a high indentation Schmid factor. As was discussed earlier, the ratio between the stress required for twinning and slip is likely much higher than estimates from uniaxial tests of polycrystalline materials. Therefore, a high indentation Schmid factor is not enough for twinning to occur. In a similar study on a similar material [114], no twinning was observed. It is unclear if twinning deformation occurs in these experiments, but the evidence thus far seems to suggest it is not occurring. This topic will be discussed further in Chapter 6.3.2.

Gong and Wilkinson [115] investigated the plastic anisotropy of grade 1 CP Ti by bending of micro-cantilever beams fabricated from single grains using FIB. Using slip trace analysis and FEM simulations, they found basal slip (209 MPa) to be within 15% of prismatic (209 MPa) and pyramidal $\vec{c} + \vec{a}$ to be about twice as much (474 MPa). No twinning was observed for beam dimensions of ~ 5μm wide and 30 μm long. Their analysis compares well to the observation that prismatic slip is likely the easiest. The difference between prismatic and basal slip is likely reduced going from grade 1 to grade 2 CP Ti due to the increased oxygen content [113]. However, the slip resistance for pyramidal $\vec{c} + \vec{a}$ still remains much higher than $\vec{a}$ slip.

In summary, the indentation yield strength is a more reliable measure of the orientation dependence on the initial flow stress than hardness measurements. The indentation yield strength orientation dependence can be explained by lack of available slip systems for indents along the c-axis requiring the more difficult pyramidal $\vec{c} + \vec{a}$ slip. The lower indentation yield strengths for declined crystals is due to the lower resistance of basal and prismatic slip, and the minimum indentation yield strength occurs for fully

declined crystals where prism is most likely occurring at the indention yield point. These observations are in good agreement with literature of testing of bulk single crystals and micro-mechanical tests on FIB specimens.

Chapter 6

Nanoindentation of α-Ti64

6.1 Methods and Materials

A bar of Ti-6Al-4V from McMasterCarr (Grade 5) was used in this study. The starting material had a duplex microstructure (equiaxed primary α grains and lamellar α+β grains). The raw material was heat treated in order to produce marginally larger primary α grains to make the process of nanoindentation with a 16μm radius indenter less difficult. The raw material was annealed at ~1025°C for 2 hours, slowly cooled (0.1°C/min) to 950°C where it was held for 1 hour. The sample was then allowed to furnace cool. This produced larger primary α grains, some having elongated shapes, as well as larger lamellar regions as shown in Figure 31. Samples were metallographically prepared to produce pristine surfaces free of deformation and oxidation. This was accomplished by removing the oxide layer that formed during the heat treatment, sectioning the material to expose an inner surface, and careful grinding and polishing. Two separate samples were prepared for nanoindentation and EBSD. The first sample was electropolished using a perchloric based electrolyte (354mL Methanol, 210mL 2-butoxyethanol, 36 mL Perchloric Acid) chilled to -20°C. A constant voltage between 20-25V for 0.5 to 5 mins was used to produce a mirror polished surface. The grain boundaries and β-phase were preferentially polished with respect to the α-phase due to the difference in electronegativity. The second sample is discussed in Chapter 7.

The same nanoindentation test procedure for CP Ti was used with a maximum indentation depth of 450 nm with a 16.5 μm radius indenter. Indents were carefully placed in the centers of grains to avoid effects from grain boundaries. Since the grain size

(20-50 µm) was much smaller than CP Ti (~400µm) only 1-2 indents could be reliably placed in individual grains. Grain orientations were determined from EBSD measurements prior to indentation following the same procedures described for CP Ti. The indentation properties and measurements were correlated with the crystal orientation at the indentation site.

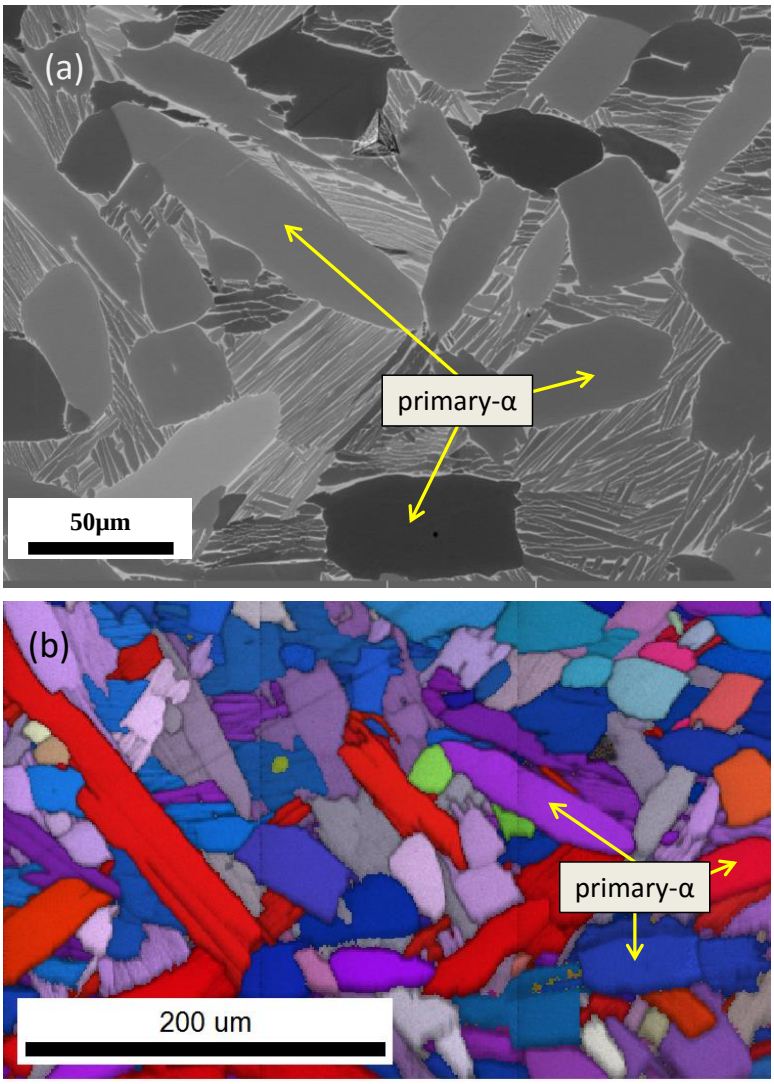

Figure 31: (a) SEM-BSE micrograph and (b) EBSD inverse pole figure map. The same three primary α-Ti64 grains are labeled in each micrograph. The images are from a chemo-mechanically polished surface.

6.2 Results

6.2.1 Elasticity Anisotropy

Indentation modulus was measured for a variety of grain orientations. The indentation modulus primarily depended on the declination angle, Figure 32. The maximum indentation modulus (~140 GPa) occurred for indents near the c-axis, and the minimum (~105 GPa) occurred for indents with declination angles approaching 90°. This was lower than CP Ti (~150-115 GPa).

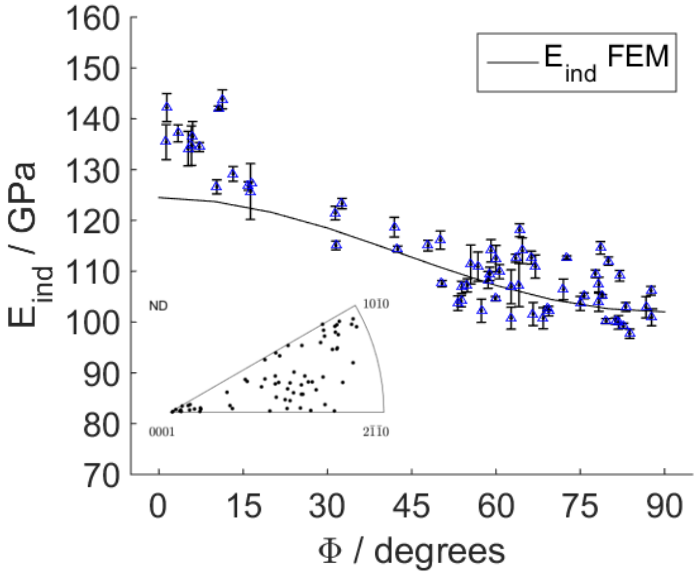

Figure 32: Indentation modulus (E_{ind}) versus declination angle (Φ) measured with a 16µm radius indenter on α-Ti64. The expected indentation modulus (E_{ind} FEM) is determined using single crystal elastic constants for Ti6Al from literature [116] in FEM simulations courtesy of M. Priddy. Error bars are ± one standard deviation which incorporates multiple answers for single tests and multiple measurements in the same grain when applicable.

6.2.2 Plastic Anisotropy

Representative ISS curves spanning the range of declination angle are show in Figure 33. The highest stresses are reached for indents close to the c-axis (low declination angles). Large pop-ins for low and high declination angles occurred in many tests. Figure

34 shows the pop-in stress versus declination angle. Pop-ins for indents near the c-axis were as high as 8 GPa decreasing to around 4 GPa for indents with declination angles between 30 and 60°. The pop-in stress then increased to as high as 5 GPa for indents with declination angles approaching 90°. This was noticeably different than the pop-in stress trends in CP Ti. The average contact radius was around 800 nm for all orientations as shown in Figure 35 which was a 300nm increase over 16µm radius indents on CP Ti. This difference is likely a reflection of the different indentation modulus and yield stresses compared to CP Ti.

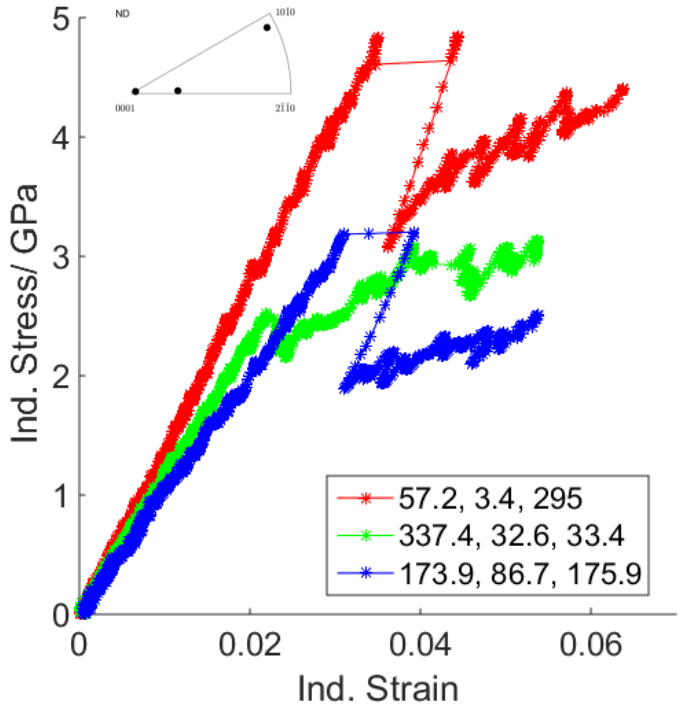

Figure 33: ISS curves for different select orientations measured with a 16µm radius indenter on α-Ti64. The Bunge-Euler angles are given in the legend for each test.

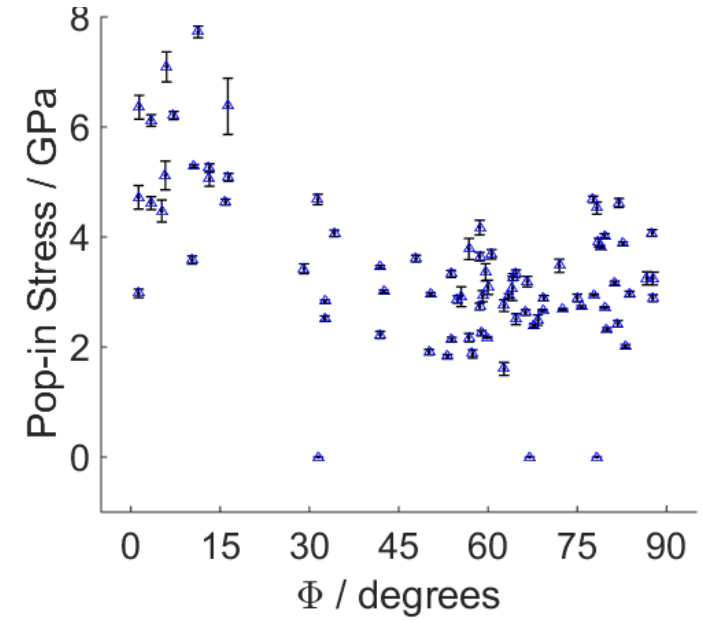

Figure 34: Pop-in stress for each test versus declination angle for α-Ti64. Error bars are ± one standard deviation based on multiple answers for each test.

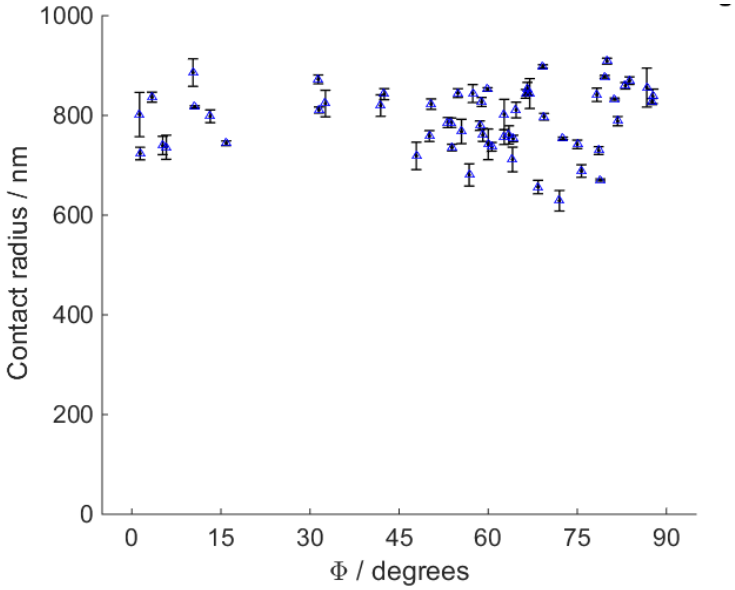

Figure 35: Average contact radius at yield versus declination angle for α-Ti64. Error bars are ± one standard deviation which incorporates multiple answers for single tests and multiple measurements in the same grain when applicable.

The indentation yield strength primarily depended on the declination angle shown in Figure 36. This trend with declination angle was similar to CP Ti; however, the indentation strengths were significantly higher (increase by a factor of 1.8 to 1.5). The indentation yield strength IPF contour plot is shown in Figure 37. The initial hardening

slope showed a clearer trend in α-Ti64 than in CP Ti, Figure 38, almost increasing by three times from 90° to 0° in a linear fashion. The linear fits for back extrapolating, which are the fits for the determining the initial hardening slope, were limited to indentation strains approximately less than 0.025 in order to be consistent with CP Ti measurements. This value was chosen for CP Ti because it gave consistent results for both 16 and 100 μm radius indenters for the back extrapolated indentation yield strength.

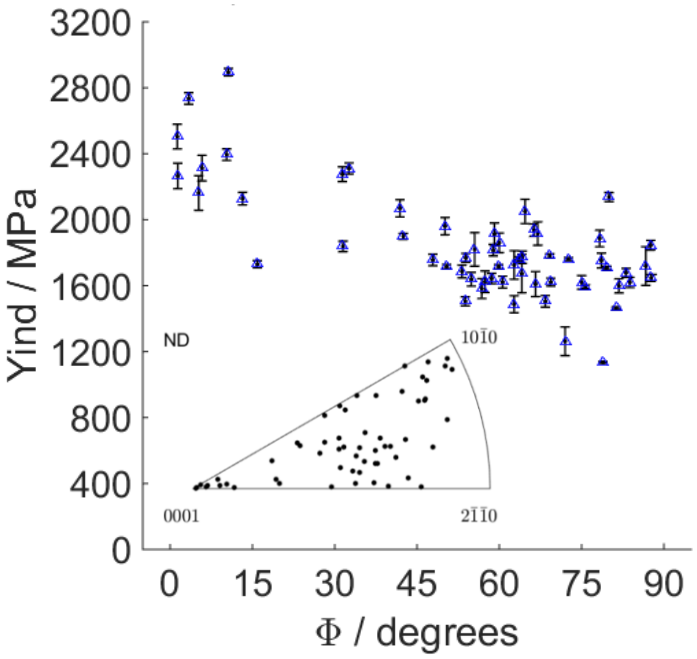

Figure 36: Indentation yield strength versus declination angle for α-Ti64. Error bars are ± one standard deviation which incorporates multiple answers for single tests and multiple measurements in the same grain when applicable.

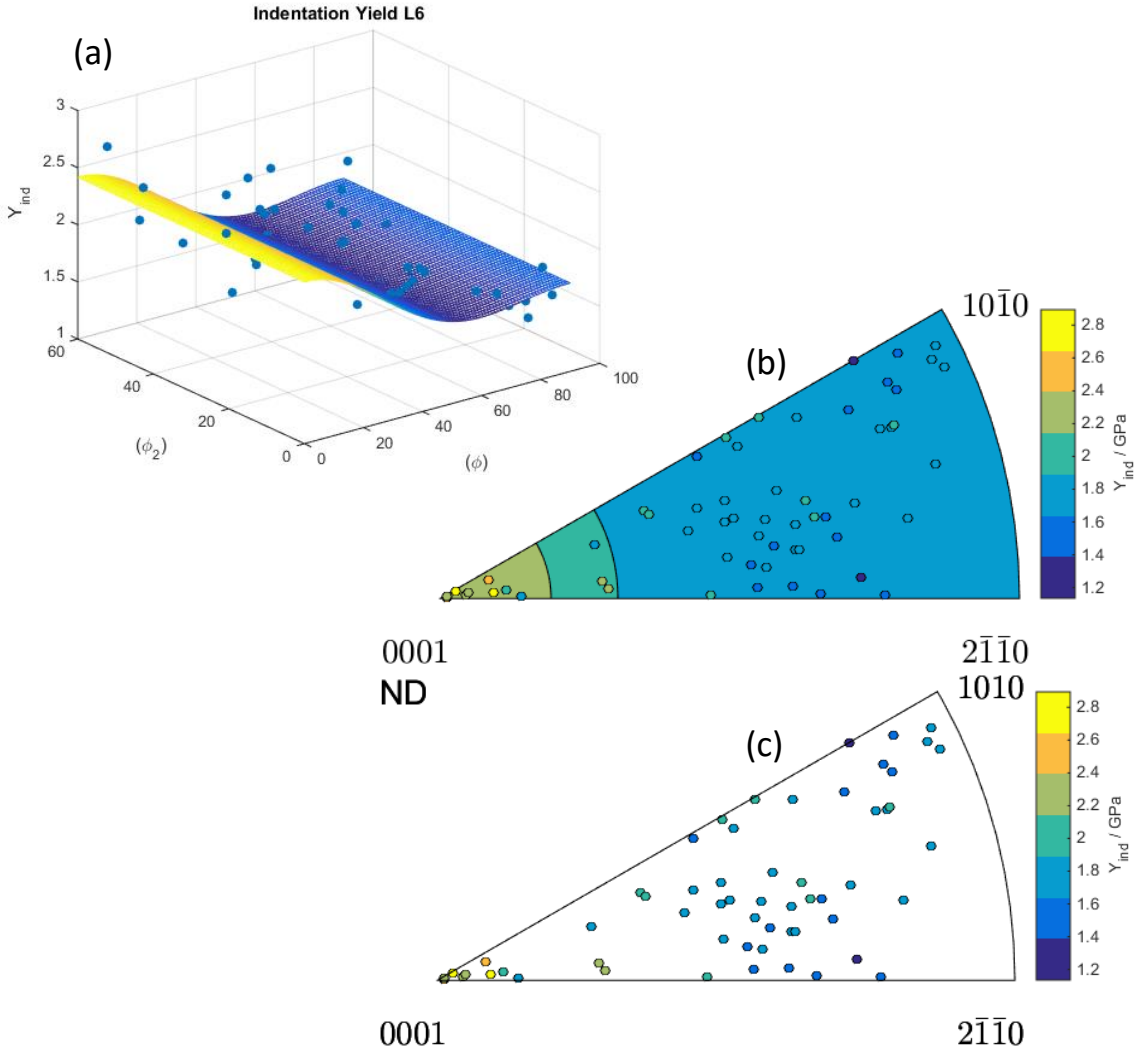

Figure 37: (a) GSH regression fit for indentation yield strength in the indentation orientation space (Bunge-Euler angles ϕ_2, φ) courtesy of D. Patel, (b) IPF contour plot for indentation yield strength. Background contour determined from regression fit. Data points are colored according to their actual values, (c) IPF contour plot without regression fit contours. Data is 16 μm radius indenter measurements on α-Ti64.

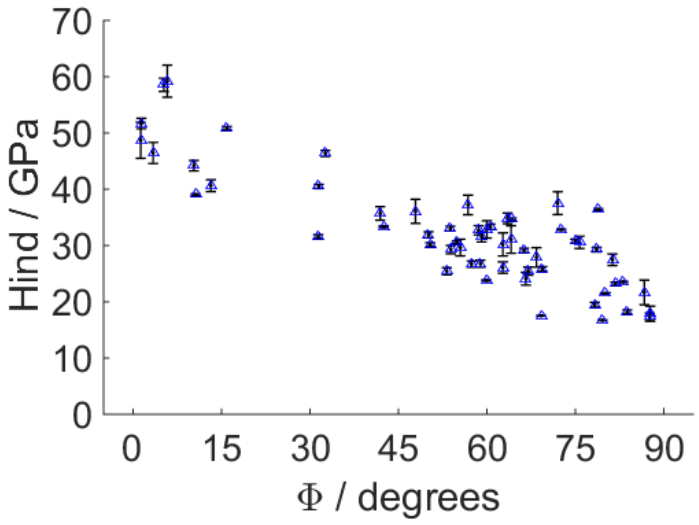

Figure 38: Indentation initial hardening slope versus declination angle for a 16 µm radius indenter on α-Ti64. A linear regression was used on data between the indentation yield point and an offset strain up to 0.02-0.025. A moving average was applied to the data before the fit to decrease sensitivity to the starting and end points due to the jagged nature of the hardening behavior.

6.3 Discussion

6.3.1 Elastic Anisotropy

The most surprising observation was the decrease in indentation modulus from CP Ti to α-Ti64. The main difference between the two is chemical composition. The α-phase in Ti64 has approximately 6.5 to 7.3 wt.% Al and 0.7 to 1.4 wt.% V [117, 118]. There is little data available on the elastic anisotropy of α-Ti64. Kim and Rokhlin [116, 119] used a novel acoustic technique to measure the α-phase elastic anisotropy in single crystal Ti6Al (6 wt.% Al) and the α-phase in a Ti alloy 6242 which had a lamellar microstructure. They found the stiffness of and α-Ti6Al to be less than CP Ti and α-Ti6242 to be more than CP Ti [116]. A minor reduction in the bulk modulus of α-Ti with the addition of Al and V is predicted by first principles [120]. Additionally, Wilson et al. [121] looked at the effects of a variety of alloying elements on the elastic constants and polycrystalline shear modulus of α-Ti. They calculated the Voigt-Ruess-Hill

approximation for the polycrystalline shear modulus and found that Al and V both reduced the shear modulus [121]. A closer look at the Kim and Rokhlin's method shows that the determination of the lamellar phase elastic constants through an inverse method is heavily dependent on the initial guess [116]. The initial guesses were the elastic constants of α-Ti [77] and β-Ti [78]. It's not clear if choosing the elastic constants of α-Ti6Al as the starting point would drastically change the results for α-Ti6242. It is also reasonable to assume that there is less uncertainty in the elastic constants of α-Ti6Al because only a single set of elastic constants was required as a starting point compared to two for the inverse method. Therefore, more weight is given to the elastic constants of α-Ti6Al then α-Ti6242. The elastic constants from Kim and Rokhlin's measurements on α-Ti6Al [116] were used to estimate the indentation modulus for α-Ti6Al. The comparison matches quite well for all orientations except indents parallel to the c-axis, Figure 32.

6.3.2 Plastic Anisotropy

A direct comparison of the indentation yield strengths for α-Ti64 and CP is shown in Figure 39. The increase is ~1.8 for indents on crystals fully declined and ~1.5 for indents on crystals nearly aligned with the c-axis. Slip resistances in titanium are strongly influenced by changes in oxygen and aluminum [74, 113, 122-126]. Aluminum increases prism slip resistance disproportionally more than other slip systems [122]. The amount in α-Ti64 (~7 wt.%) also suppresses twinning [122, 123, 127]. Oxygen content has a similar influence on prism slip and twining [74, 113, 123]. These changes are strongest going from high purity to commercial purity oxygen contents [113]. The maximum oxygen contents in grade 2 CP Ti and grade 5 Ti64 are 0.25 and 0.20 wt.%, respectively. Therefore, the increase in indentation strength is likely due to the addition of aluminum

and not small differences in oxygen content. The disproportional increase in the slip resistance of prism is seen in these measurements by the higher increase in yield strength at fully declined orientations where prism slip is most active (see Chapter 5.3.2 for comparison).

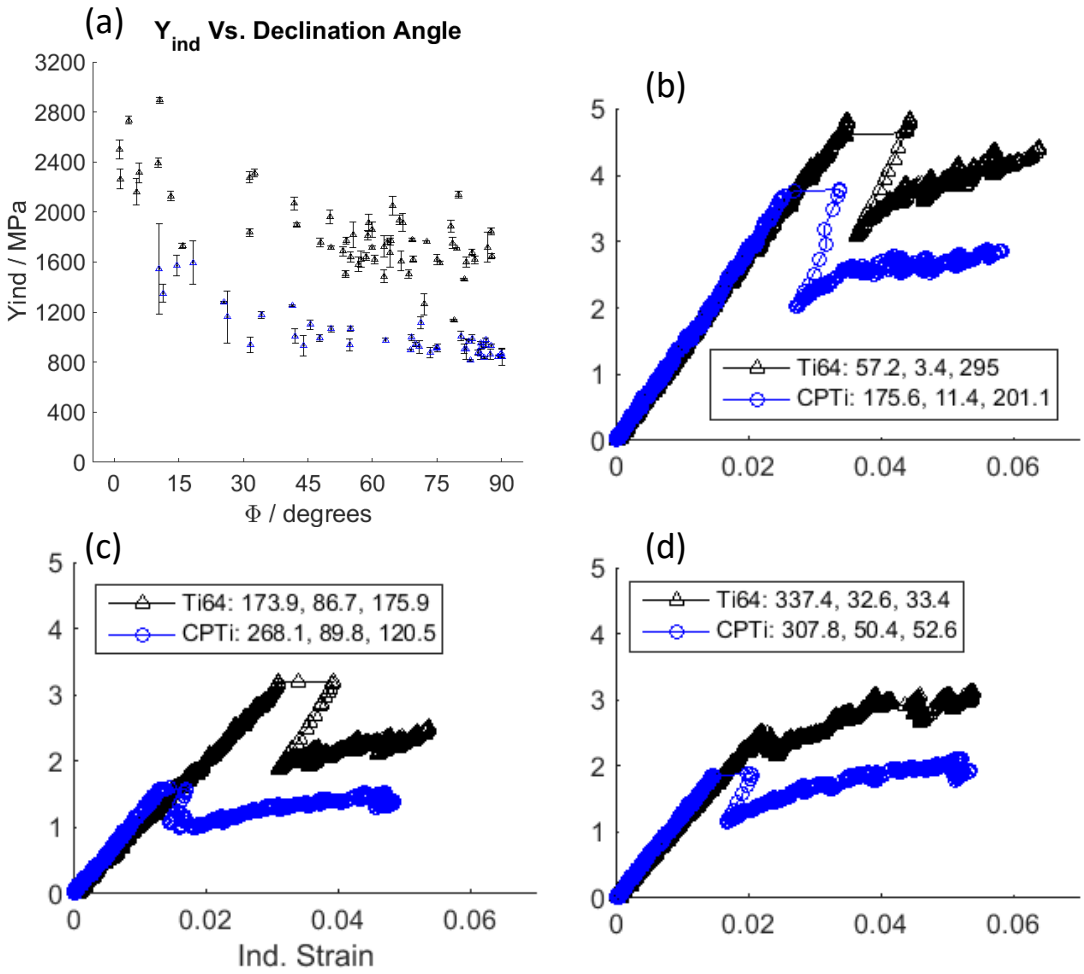

Figure 39: (a) Indentation yield strength versus declination with a 16µm radius indenter on α-Ti64 (black) and CP Ti (blue), (b, c, d) ISS curves with 16µm radius indenter for CP Ti (blue) and α-Ti64 (black) for similar orientations ranging in declination angle.

The indentation Schmid factor calculations by Kwon et al. [104] can be applied to understand the orientation dependence on indentation yield strength with a higher degree of confidence than on CP Ti because they used elastic constants for α-Ti6Al [103, 119] which are in close agreement with the indentation measurements in this work. These

calculations, Table 4, were done for three orientations with prism, basal, and pyramidal $\vec{a}$, first and second order pyramidal $\vec{c}+\vec{a}$, and $[\bar{1}101](1\bar{1}01)$ extension twinning. Extension twinning is more readily observed than compression twinning for this alloy content [122, 128], and no compression twining was observed for compression of single crystals along the c-axis [122]. Again, it becomes clear that pyramidal $\vec{c}+\vec{a}$ is more favorably oriented for slip than other systems for indents along the c-axis. Due to its higher slip resistance, this lead to the increase in indentation yield strength for near c-axis orientations. For fully declined indents ($[\bar{1}100]$ and $[\bar{1}2\bar{1}0]$), prism is favorably oriented and has the lowest slip resistance which leads to a minimum in indentation yield strength.

Table 4: Indentation Schmid factors calculated for alloyed α-Ti take from [104]

Indentation Orientations and Maximum Indentation Schmid Factors			
	Orientations		
Slip/twin systems	[0001]	$[\bar{1}100]$	$[\bar{1}2\bar{1}0]$
Basal 〈a〉	0.204	0.207	0.233
Prismatic 〈a〉	0.0372	0.275	0.275
Pyramidal 〈a〉	0.106	0.24	0.24
1st pyramidal 〈c + a〉	0.295	0.283	0.27
2nd pyramidal 〈c + a〉	0.312	0.249	0.289
Extension twin	0.0463	0.293	0.252

Fundenberger et al. [128] studied the differences in slip for CP Ti and Ti64 using a combination of modeling and polycrystalline experiments. They reported the ratios of each slip system normalized by prism slip. Comparing the ratios of Ti64 to CP Ti in their study (e.g., $\left(\frac{basal}{prism}\right)_{Ti64} / \left(\frac{basal}{prism}\right)_{CP\ Ti}$) the relative changes of each slip system with respect to its prism slip level was 1, ~0.55, and ~0.9 for basal, pyramidal $\vec{a}$, and pyramidal $\vec{c}+\vec{a}$. In other words, the ratio of basal to prism remained the same, the ratio

of pyramidal $\vec{a}$ to prism in Ti64 is predicted less than the ratio in CP Ti, and the ratio of pyramidal $\vec{c}+\vec{a}$ to prism only changed marginally. No twinning was allowed in Ti64, while for CP Ti extension twinning was slightly easier than pyramidal $\vec{c}+\vec{a}$ and compression twinning was slightly higher [128]. The predicted ratios of slip resistance of basal and pyramidal $\vec{c}+\vec{a}$ normalized to prism slip for CP Ti and Ti64 according to Fundenberger et al. [128] are in good agreement with the indentation yield strength trends for declination angles. This agreement includes a small decrease in the ratio of pyramidal $\vec{c}+\vec{a}$ to prism in Ti64 manifest in the slightly lower increase in indentation yield strength for indents along the c-axis compared to fully declined crystals. A closer look at the pop-in stress also provides some insight into the initial plastic deformation.

There is a difference in the pop-in stress for grains declined between 45 and 90° between CP Ti and α-Ti64 as seen in the ISS curves in Figure 39 and the orientation dependence in the pop-in stress in Figure 40. The activation of dislocation sources in starved volumes (pop-ins) and slip system activity are closely related because the pop-in is a process of dislocation multiplication and motion to the surface (i.e., slip) [68]. The same indenter size was used for both measurements, both materials were well annealed, and both surfaces were electropolished. This allows us to compare the pop-in stresses without any effects due to indenter size or deformation history (e.g., cold work). The pop-in stress for α-Ti64 clearly increases for increasing declination angles going from 45 to 90°. While, in CP Ti measurements it declines slightly. The pop-in stresses for α-Ti64 are also twice as much as CP Ti at 90°. The overall increase in the pop-in stresses for all orientations are likely due to the increases in slip resistances in α-Ti64. However the pronounced difference at fully declined orientations may be due to the difference in prism

slip which is the most sensitive slip system to the difference in aluminum content between CP Ti and α-Ti64.

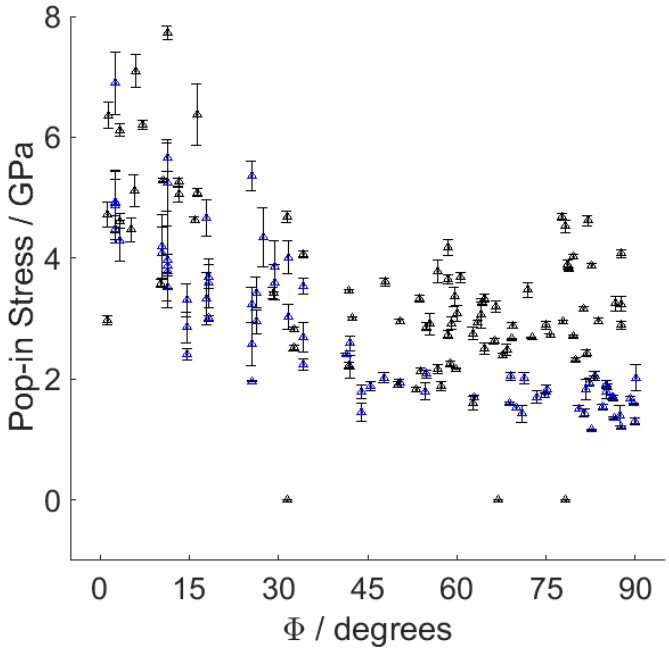

Figure 40: Indentation pop-in stress versus declination angle with a 16μm radius indenter on α-Ti64 (black) and CP Ti (blue).

As was discussed earlier it is not clear whether twinning occurs (Chapter 5.3.2), and there are clear differences in twinning deformation in bulk polycrystalline CP Ti and Ti64. However, the indentation yield strength trends with orientation between CP Ti and α-Ti64 are similar, and the differences can be easily explained by the expected differences in slip resistances. This is further evidence that twinning is likely not occurring during indentation of CP Ti and α-Ti64 in the early stages of plastic deformation. A comparison to literature of micromechanical testing on alloyed α-Ti will also help to provide further clarification of the trends observed in the ISS response.

There have been a number of nanoindentation studies on alloyed α-Ti [104, 114, 129, 130]. As was the case for CP Ti, modulus and hardness measurements using traditional indentation protocols have led to inconsistent results. Han et al. [129] reported

the highest hardness values (4.71 GPa) in α-Ti64 for an orientation close to the $\{10\bar{1}0\}$ and the lowest hardness values (3.51 GPa) for orientation half way between $[10\bar{1}0]$ and $[11\bar{2}0]$ with a high declination angle. The hardness measurements by Kwon et al. [104] on α-Ti7Al (7 wt.% Al) resulted in the highest hardness for indents near the c-axis (7.7 GPa) and values of 5.1 and 4.6 GPa for $[\bar{1}100]$ and $[\bar{1}2\bar{1}0]$ orientations, respectively, with the differences being statistically significant. This is consistent with the measurements by Viswanathan et al. [114] who found values of ~6.5 GPa along the c-axis and ~4.5 for fully declined orientations in α-Ti64. None of these authors reported an orientation dependence on the indentation modulus with Berkovich indentation. Kwon et al. [104] also made spherical indentation measurements with a conical-spherical tip with a 0.36 μm radius for which they report elastic sample moduli of 189, 155, and 150 GPa for [0001], $[\bar{1}100]$, and $[\bar{1}2\bar{1}0]$, respectively. These values are much higher than the expected values for their material.

Viswanathan et al. [114] and Kwon et al. [104] performed careful cross-sectional TEM analysis at indent sites. Viswanathan et al. [114] concluded that the slip systems which had the highest resolved shear stress determined using the Schmid factor were the ones with the most dislocations and slip activity. Additionally, the Schmid factor for $\vec{c}+\vec{a}$ slip had to be significantly higher than any $\vec{a}$ -type slip system in order for $\vec{c}+\vec{a}$ dislocations to be the primary ones observed. In their study, no twinning was observed. Kwon et al. [104] observed slightly different slip activity likely due to the difference in tip geometry. They used a conical-spherical tip and indented past the spherical geometry of the tip as opposed to a Berkovich tip. They observed features which look like very small extension twins for indents on $[\bar{1}100]$. However, as was discussed previously, the

evidence that the features are twins is primarily based on a high indentation Schmid factor for extension twinning. They also observed slip for every slip system for all three orientations. The drawbacks of both of these studies are that the TEM analysis is made post-test after a significant amount of deformation has occurred. Although the conical-spherical tip puts less deformation in the material than the Berkovich tip, it still would have produced an equivalent indentation strain much higher than the indentation strains in this work. The indentation yield strength is also a measure of the early stage of deformation which further distances the observations made by TEM to the deformation behavior that controls the indentation yield strength. This is why it is not directly clear from these studies as to which slip activity is occurring in the elastic-plastic transition of the ISS measurement in this work. However, the basic observations are in good agreement with the indentation yield strength trends in this work.

There are only three micropillar compression studies on alloyed α-Ti [110, 112, 131]. The single study [112] that looked at the response for different orientations showed pillars of Ti5Al (5 wt.% Al) were stronger for c-axis orientations compared to $[2\bar{1}\bar{1}0]$ pillars. The strength for a comparable pillar size (primary indentation zone diameter) was ~ 2 GPa for c-axis orientations. Given the difference in stress state, protocols, and chemical composition, this value compares reasonably well to the indentation yield strength of ~2.4 GPa. In summary, the increase in indentation yield strength in α-Ti64 over CP-Ti crystals is due to an increase in the slip resistances in prism, basal, and pyramidal $\vec{c} + \vec{a}$ with a slightly higher increase likely for prism slip. There is little evidence for twinning during these indentation experiments which is expected since the

stress required for twinning is likely much higher during nanoindentation than in polycrystalline bulk tests.

Chapter 7

Nanoindentation of α-β Single Colonies in Ti64

7.1 Methods and Materials

Ti-6Al-4V (Ti64) in the β-annealed condition was used for characterizing the colony microstructure because it has a fully lamellar microstructure, Figure 41. No additional heat treating was made to the as-received material since it is already in a well annealed condition. The β-phase (bcc crystal structure) made up only a small volume fraction of the material (~2%) [132] and had a thickness of ~0.5μm. The α-phase (hcp crystal structure) lathe thickness was around 3.5 μm. The EBSD map in Figure 41 contains orientation information for only the α-phase. The Burger's orientation relationship (BOR) describes the possible orientations (variants) of the α-phase that can form when the material is cooled down from above the β transition temperature [76]. The BOR relationship was described in Chapter 2, Figure 6. Another way to think about the colony microstructure is for a given α-phase orientation, there are 12 possible symmetrically related β-phase orientations. Due to the high symmetry of the β cubic crystal and one slip family, the exact variant of the β-phase is likely not important in relating the structure of the α-β colony to ISS measurements. Thus, only the α-phase orientation will be used to describe the orientation of the colony.

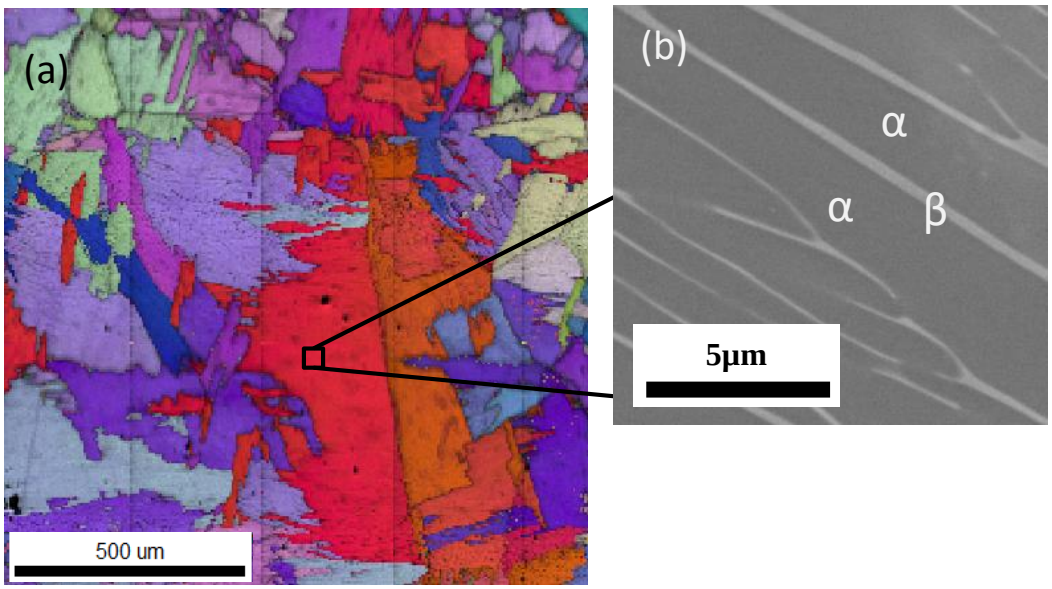

Figure 41: (a) EBSD IPF map of the α-phase orientations of α-β colonies, and (b) SEM-BSE micrograph of the α-β structure inside a single colony. The images come from a chemo-mechanically polished surface.

In order to probe individual colonies, a 100 µm radius indenter was used. It will be shown that this indenter size produces indentation zones that encompass multiple α-β lathes. The same indentation test procedures as CP Ti and α-Ti64 were used with a final displacement of 800 nm. Similarly to previous samples, EBSD was done prior to indentation. However, in this case SEM images were taken at indentation sites after indentation. The same analysis procedures for CP Ti and α-Ti64 were used to extract indentation stress-strain curves form the load-displacement data and make ISS property measurements. Samples were metallographically prepared with the rod axis (designated ND) parallel to the indentation direction. Sectioning, grinding, and polishing was done following the same procedures used for previous titanium samples. Two samples were prepared for indentation which differed only in the final polishing step. The first sample was electropolished using a perchloric based electrolyte (354mL Methanol, 210mL 2-butoxyethanol, 36 mL Perchloric Acid) chilled to -20°C. A constant voltage between 20-25V and a time of 0.5 to 5 mins was used to produce a mirror polished surface. The grain

boundaries and β-phase were preferentially polished with respect to the α-phase due to the difference in electronegativity. Electropolishing is the preferred preparation method for nanoindentation because it constituently produces deformation free surfaces for many metals. However, for two phase indentation sites, it appears to cause problems. Figure 41 shows a representative indentation result for an electropolished sample. The ISS curve has a distinct jog in the elastic loading. SEM imaging shows the clear height differences between the α and β phases caused by electropolishing. The jog in the ISS curve in the elastic loading appears to correlate with contact area crossing the phase boundary as illustrated on the SEM micrograph with contact areas overlaid. The results for the electropolished sample also yielded low modulus values more often than not and considerable scatter between indents in the same colony. This was likely a consequence of the surface roughness.

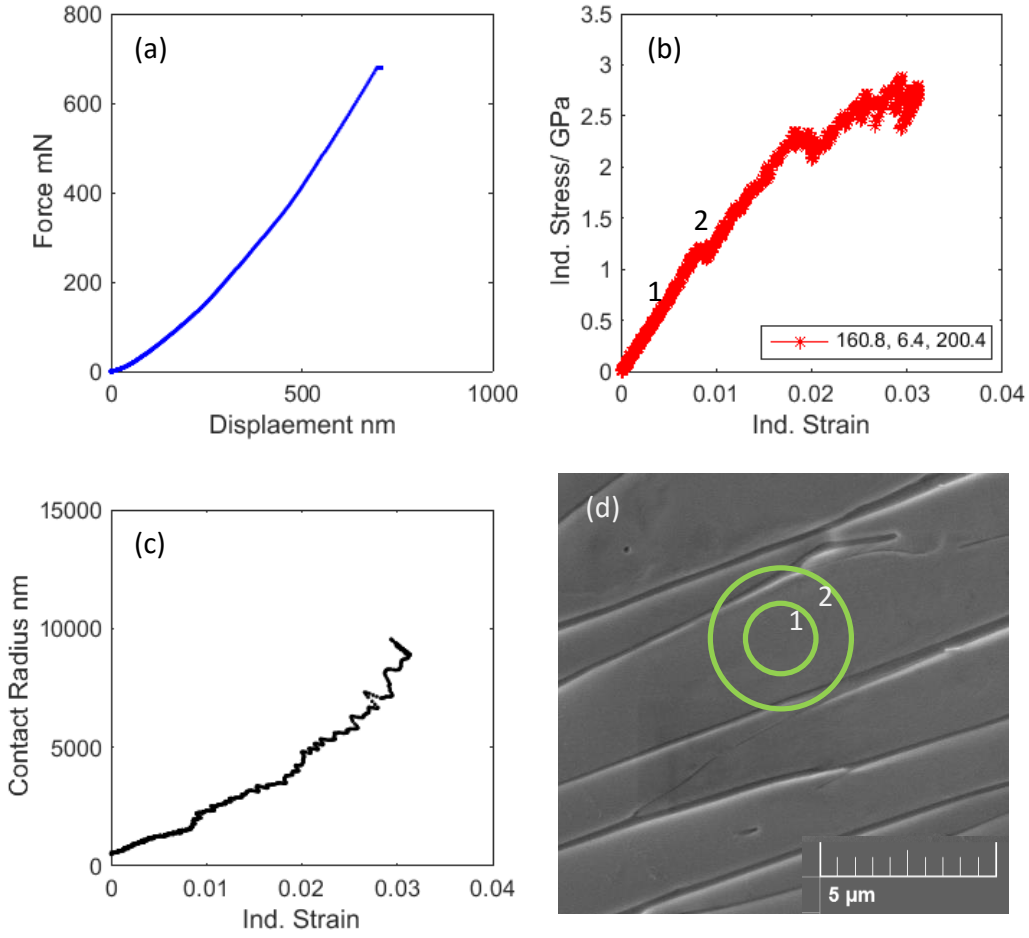

Figure 42: (a) Load-displacement curve, (b) ISS curve, (c) contact radius versus indentation strain, and (d) SEM micrograph of indentation site post-test. Circles 1 and 2 correspond to the approximate projected contact area for indentation strains of 0.004 and 0.01 respectively. For emphasis, these points are marked on the ISS curve. Micrograph is a SE image. The surface was electropolished.

In order to produce a flatter surface in α+β regions, a chemo-mechanical polishing procedure was used. The final polishing step was with 5 parts 0.06 µm colloidal silica mixed with 1 part hydrogen peroxide. The quality of surfaces prepared using this procedure were first evaluated on Ti-64 samples that were heat treated for larger α-Ti64 grains (Ti64 material used in Chapter 6). This provided a direct comparison between electropolished surfaces where roughness was not a problem and chemo-mechanical polished surfaces using the 16 µm radius indenter. Due to the smaller primary indentation

zone at yield, the 16 μm radius indenter is more sensitive to surface deformation than the 100 μm radius indenter. These tests provide a strong case for validating the chemo-mechanical polished surfaces for reliable ISS measurements.

Indeed, the chemo-mechanical polishing procedure produced reliable results on α-Ti64 after it was repeated multiple times (more than 10 mins total). Figure 43 shows a poor transition after one polishing and a sharp transition after the second polishing. This sample preparation procedure affects the pop-ins stress (reduced pop-in stress), but it does not affect the indentation yield strength. In other words, the back extrapolated indentation yield strength for tests with larger pop-ins yields the same values as tests with small pop-ins and no pop-ins where a 0.2% offset is used. This is crucial for comparing the indentation yield strengths for electropolished and chemo-mechanical polished surfaces without any effects on the indentation yield strength due to sample preparation procedures.

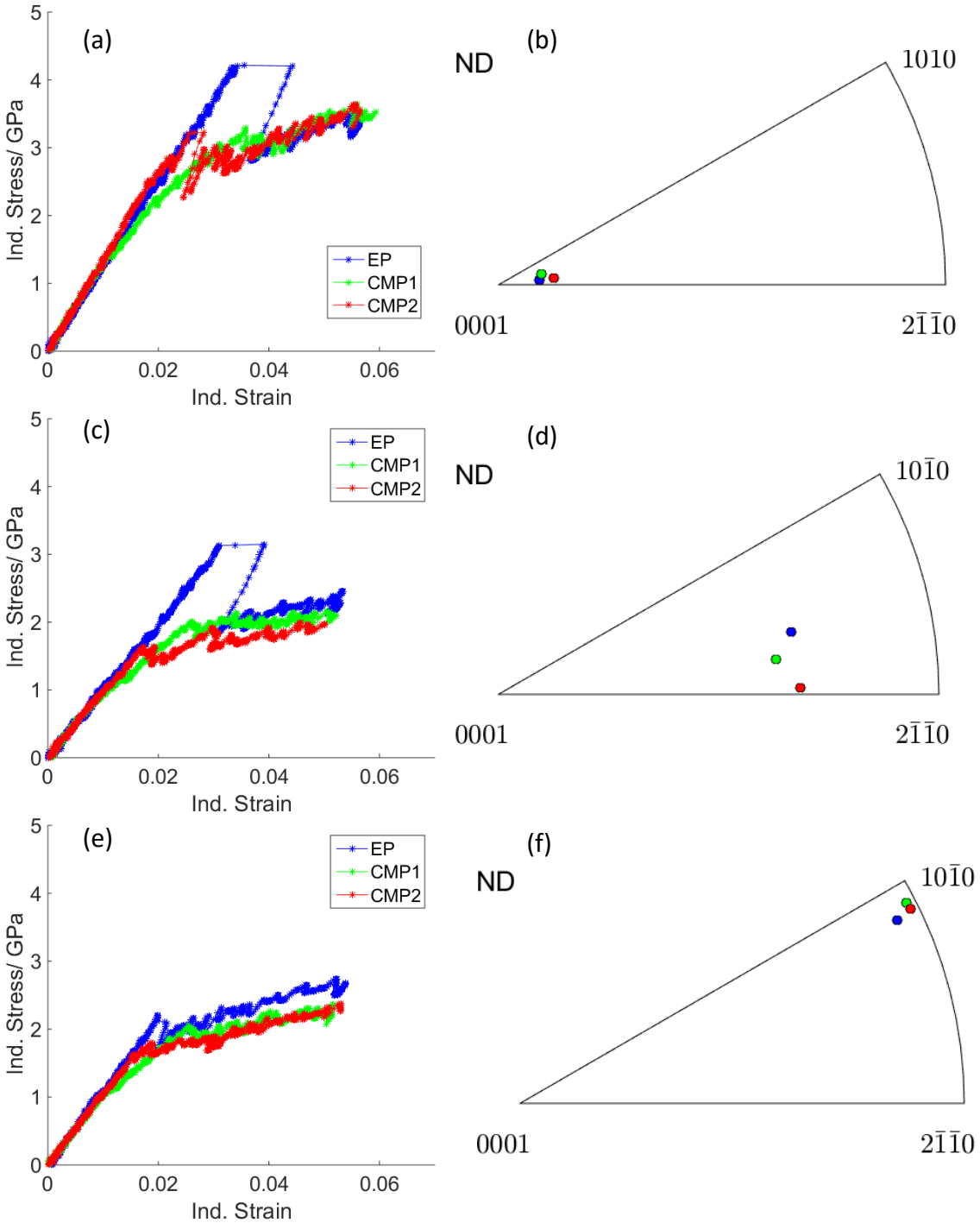

Figure 43: (a,c,e) ISS curves for three different orientations, and (b,d,f) their respective locations in the IPF. Electropolished (EP) surfaces are compared to a chemical-mechanical polished surface (CMP) for a single (CMP1) and repeated (CMP2) polish.

The result for 100 µm radius indents on a chemo-mechanical polished Ti64 β-annealed sample is shown in Figure 44. In this case, the ISS curve remains linear in the initial elastic loading as the contact area passes over the phase boundaries. In order to make reliable indentation measurements on the colony microstructure, the chemo-mechanical sample preparation procedure was required. All indentation measurements for the colonies were made using this sample preparation procedure.

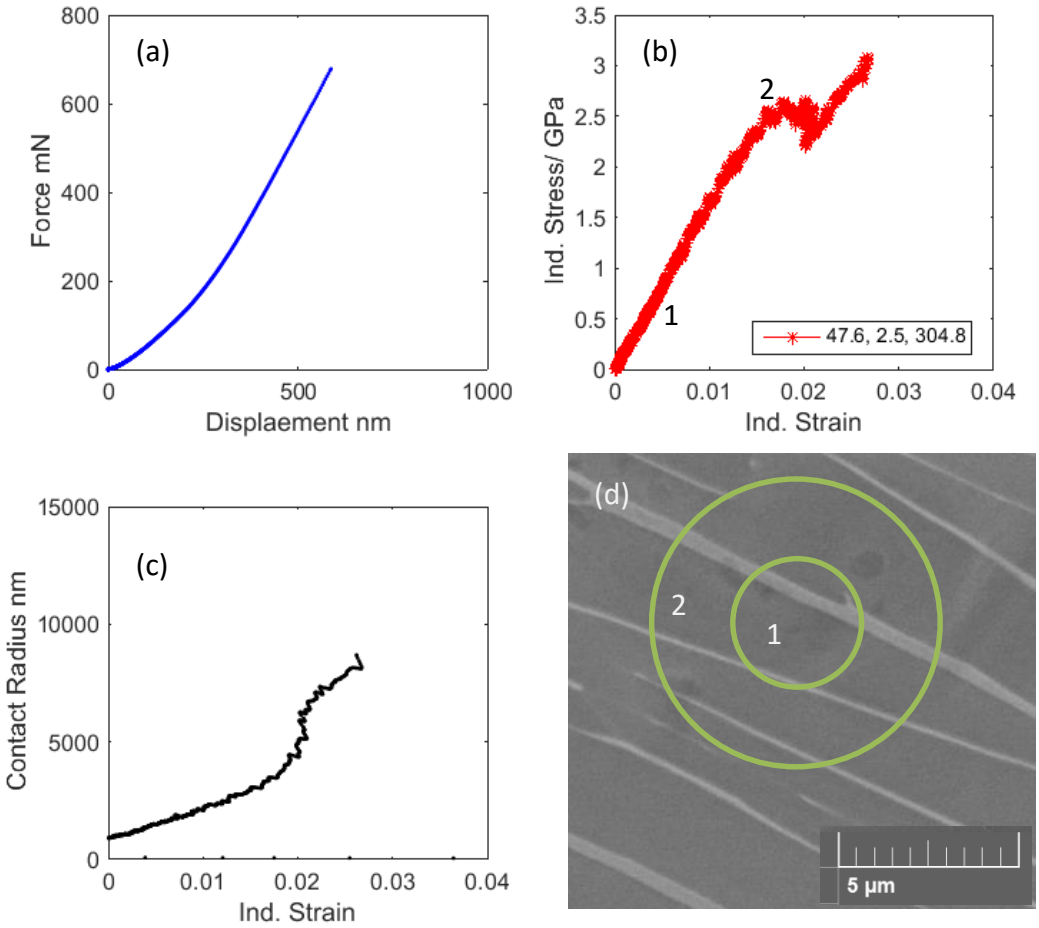

Figure 44: (a) Load-displacement curve, (b) ISS curve, (c) contact radius versus indentation strain, and (d) SEM micrograph of indentation site post-test. Circles 1 and 2 correspond to the approximate projected contact area for indentation strains of 0.006 and 0.017, respectively. For emphasis these points are marked on the ISS curve. Micrograph is a BSE image. The surface was chemo-mechanically polished.

7.2 Results

7.2.1 Elastic Anisotropy

The indentation modulus results for 100 μm radius indents on α-β Ti64 colonies are shown in Figure **45.** They are higher than α-Ti64 and similar to CP Ti in magnitude. The trend with the α-phase declination angle is similar to the trends in CP Ti and α-Ti64. One source from literature for the elastic constants of Ti64 β-annealed were used for determining the expected indentation modulus values [132].

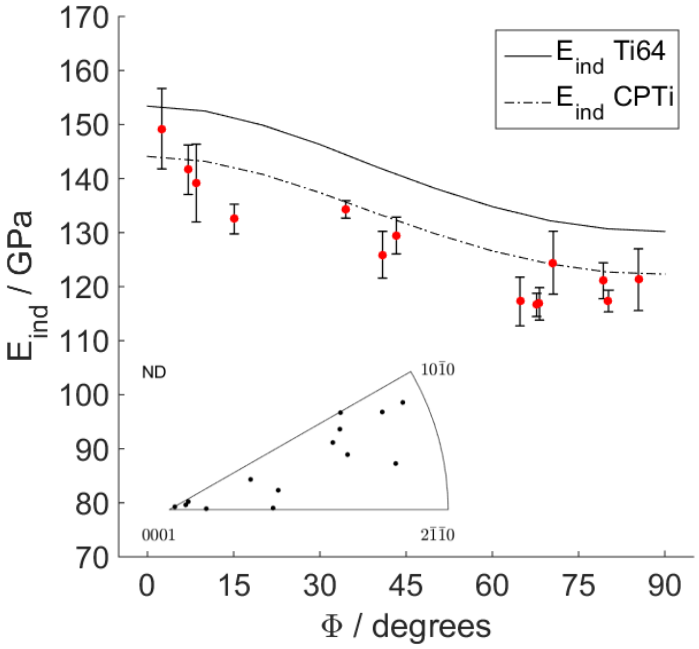

Figure 45: Indentation modulus (E_{ind}) versus declination angle (Φ) measured with a 100 μm radius indenter on Ti64 colonies. The expected indentation modulus (E_{ind} FEM) is determined using elastic constants from literature for CP Ti [77] and Ti64 [132] in FEM simulations courtesy of M. Priddy. Error bars are ± one standard deviation which incorporates multiple answers for single tests and multiple measurements in the same grain when applicable.

7.2.2 Plastic Anisotropy

Representative ISS curves for three distinct declination angles are shown in Figure 46. The same overall trend as CP Ti and α-Ti64 is observed. The highest indentation stresses are reached for colonies with the lowest declination angles. Figure 47 definitively shows that the contact area prior to yield covers multiple α-β lathes for different orientations. For the same indentation displacement, higher strains are reached for tests with higher declination angles. The residual indentation and surrounding area for Figure 47 c shows an impression with slip lines likely related to prismatic slip since they are aligned with the α-crystal prism planes. For indents on colonies with the α-phase aligned near the c-axis, the impression is barely noticeable. It is difficult to extract any more information from the micrographs of the indentation sites since they were indented to the same displacement and not the same indentation strain.

Since the indentation sites are now heterogeneous, it is important to observe the repeatability of measurements within the same colony. Figure 48 shows the ISS curves for three tests in the same colony for two different colonies with different α-phase orientations. The scatter is within the expected variance for indents in the same grain for a pure (homogenous) material. This would imply there is no dependence on where the indent is placed with respect to the β-phase (i.e., directly on an α or β lamellae). The orientation dependence of the indentation yield strength is shown in Figure 49 and Figure 50. The dependence on the α-phase declination angle is similar to CP Ti and α-Ti64. The magnitude of the indentation yield strength is similar to α-Ti64. The hardening behavior of the Ti64 colonies had significant variance due to the rather short plastic segments and more pronounced jagged behavior for some tests. The indentation depth and indentation

strain were dictated by the size and spacing of indents so that repeated measurements inside the same colony could be reliably made. For these reasons no trends could be observed for the initial indentation hardening measurements. From observations of the ISS curves, it appears that indents with the α-phase aligned close to the c-axis have distinct drops in stress followed by continued hardening not seen in other orientations. The contact radius at yield was around 3.5 μm for all orientations.

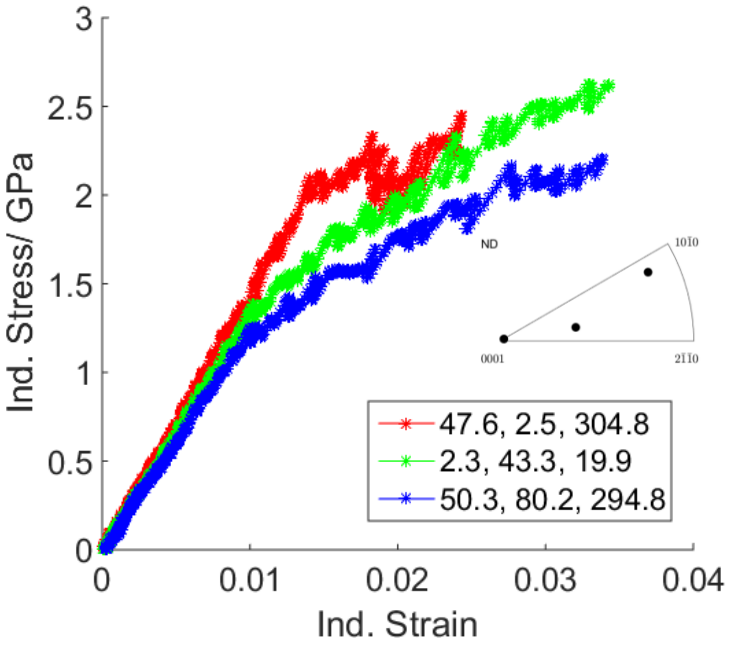

Figure 46: ISS curves for select orientations measured with a 100μm radius indenter on Ti64 colonies. The Bunge-Euler angles are given in the legend for each test.

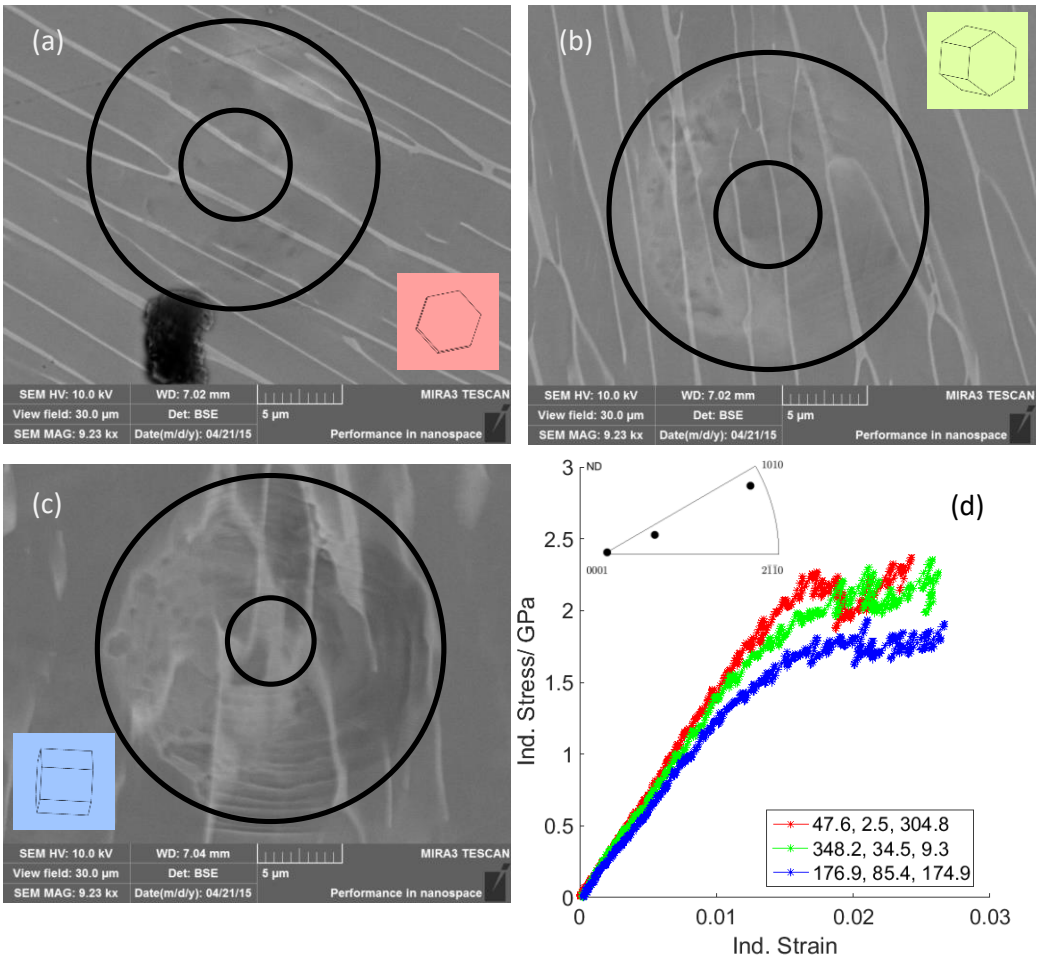

Figure 47: (a-c) BSE micrographs of indentation sites post-test for three different orientations going from hard to soft orientations respectively. The crystal lattice of the α-phase is also shown in the corner of each image. The small and large black circles represent the projected contact area prior to the yield point and at the maximum load respectively. (d) Corresponding ISS curves color coded to match the crystal lattice inserts.

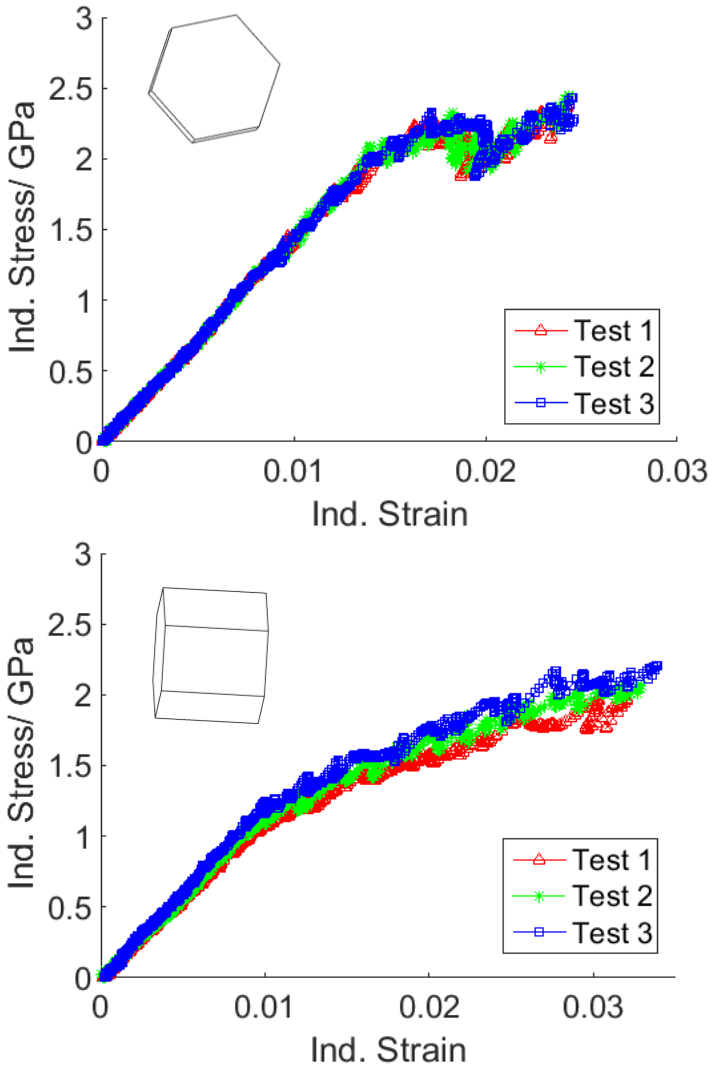

Figure 48: (a-b) ISS curves for three tests in the same Ti64 colony. The crystal lattice of the α-phase is also shown in the corner of each image. The α orientation of the colonies is close (a) to the c-axis (Φ=2.5°) for and (b) almost perpendicular to the c-axis (Φ=80.2°) .

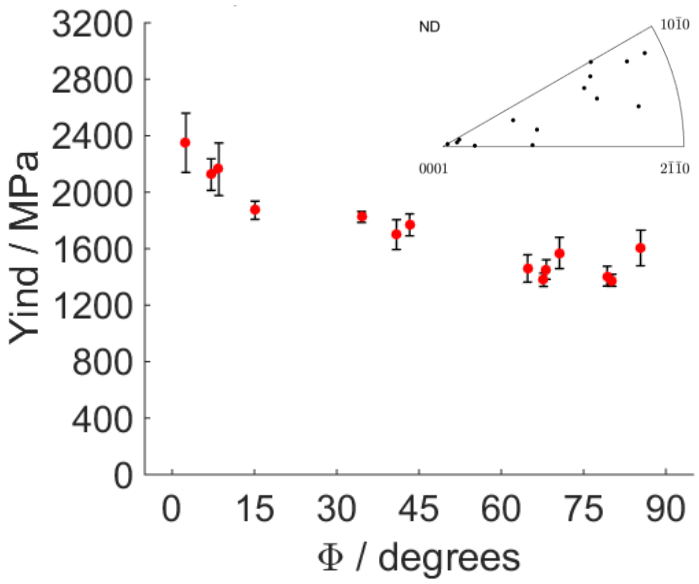

Figure 49: Indentation yield strength versus declination angle for Ti64 colonies. Error bars are ± one standard deviation which incorporates multiple answers for single tests and multiple measurements in the same grain when applicable.

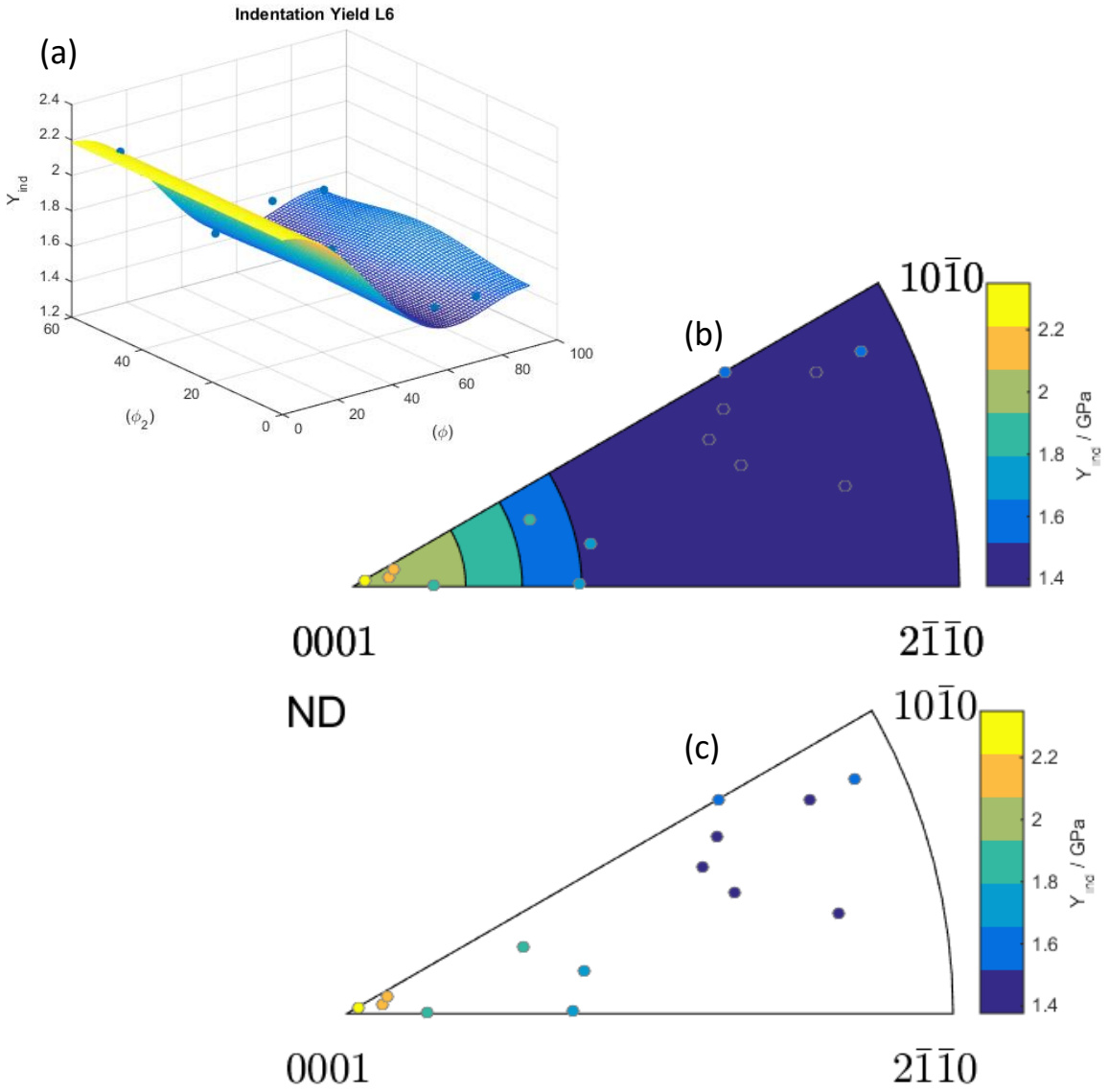

Figure 50: (a) GSH regression fit for indentation yield strength in the indentation orientation space (Bunge-Euler angles ϕ_2, φ) courtesy of D. Patel, (b) IPF contour plot for indentation yield strength with the background contour determined from regression fit. Data points are colored according to their actual values, (c) IPF contour plot without regression fit contours. Data is from 100 µm radius indenter measurements on Ti64 colonies.

7.3 Discussion

7.3.1 Elastic Anisotropy

The indentation modulus primarily depends on the declination angle with the stiffest orientations close to the c-axis and the lowest at full declination. The magnitudes of the indentation modulus are greater than α-Ti64 but not significantly different than CP Ti as shown in Figure 51. Since the Young's modulus for Ti64 (~114 GPa) is higher than CP Ti (105 GPa), there is an expectation that the indentation modulus would be higher than CP Ti for most orientations. The only orientations where the indentation modulus of Ti64 might be higher than CP Ti are at high declination angles. The elastic constants determined for Ti64 by Smith et al. [132] are consistently higher than the experimental values, although they have the same trend with orientation. Smith et al. [132] calibrated the elastic constants with monotonic and cyclic stress-strain curves using crystal plasticity FEM. The uncertainty of this process and the indentation measurements combined could be the reason for the large apparent disagreement. However, it is clear that the small amount of β-Ti increases the stiffness of the colony over α-Ti64 as seen in the indentation modulus trends. This leads one to believe that β-Ti64 should be stiffer than α-Ti64 for at least some orientations.

Annealed β-Ti alloys have a Young's modulus of 100-105 GPa [74]. Recently, Phani et al. [133] used a novel atomic force acoustic microscopy technique to measure the α and β phases in Ti64 in a similar fashion to nanoindentation. They reported indentation modulus values of 117-120 GPa for β-Ti64 and 133.5 GPa for α-Ti64; however, their measurements do not account for crystal orientation at the site of the measurements. In summary, it's unclear what the elastic properties of β-Ti64 are. The

indentation measurements presented here on α-Ti64 and Ti64 colonies seem to imply higher elastic properties than what is currently reported for β-Ti [78].

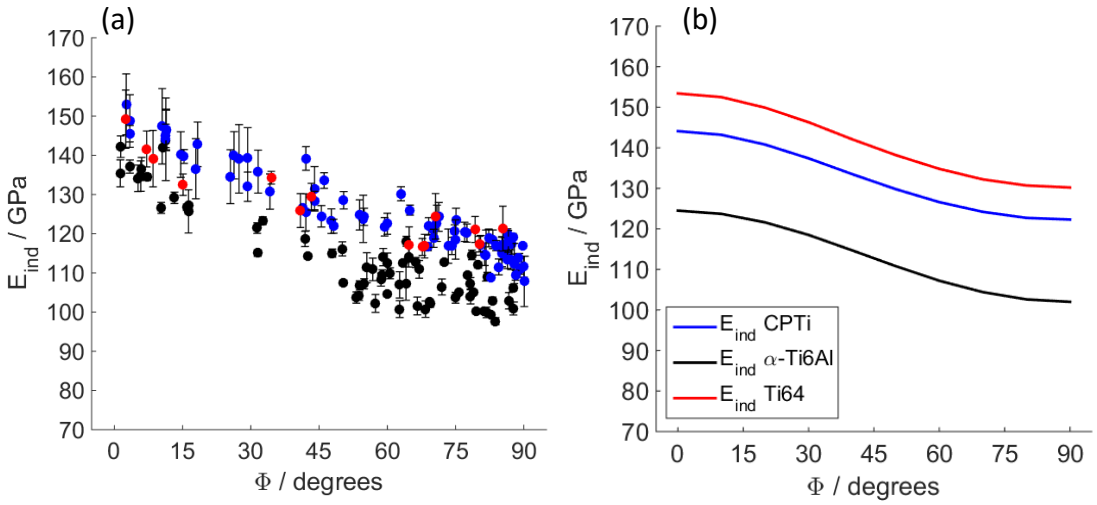

Figure 51: (a) Indentation modulus (E_{ind}) versus declination angle (Φ) measured on CP Ti (blue), α-Ti64 (black), and Ti64 colonies (red). Error bars are ± one standard deviation which incorporates multiple answers for single tests and multiple measurements in the same grain when applicable, (b) The expected indentation modulus determined using single crystal elastic constants from literature [77, 116] in FEM simulations courtesy of M. Priddy.

7.3.2. Plastic Anisotropy

The orientation dependence in yield strength for Ti64 colonies largely followed the same dependence observed for CP Ti and α-Ti64. The indentation strength increased significantly (almost twice as much) over CP Ti. This can be seen in Figure 52 where indents with the same indenter size (100μm) are compared between Ti64 colonies and CP Ti. However, there is little difference between 16 μm indents on α-Ti64 and 100 μm indents in α+β colonies as shown in Figure 52. This would imply that the β-phase does little to increase the initial slip resistance of the colony phase compared to α-Ti64. Chan et al. [134] and Suri et al. [135] showed the single colonies structure have a high degree of plastic anisotropy. In addition to the plastic anisotropy of the α-phase, there is also some anisotropy between different $\vec{a}$ directions. Due to the orientation relationship

(BOR) between α and β [76], there is one $\vec{a}$ direction that lines up closely (0.7°) with the ⟨1 1 1⟩ slip direction in the β-phase which allows for easy transfer of slip across the phase boundary compared to the other $\vec{a}$ directions [108, 135-138]. Most of these observations were made in single colony measurements. He et al. [136] also observed slip transfer for BOR interfaces and some non-BOR interfaces in polycrystalline tensile tests for a titanium alloy with similar α-β morphology. All of this seems to support the observation that the indentation strength isn't changing from indents on α-Ti64 to α-β Ti64 colonies. In regards to the additional plastic anisotropy for $\vec{a}$ slip in colonies, it is likely the heterogeneous stress in indentation and the symmetry of the indenter reduce the chances of capturing this significantly. In other words, there is no indentation equivalent for lining up single slip systems for easy slip. There was no additional orientation dependence on yield strength observed, likely for the above mentioned reasons.

Jun et al. [139] recently did micropillar compression experiments on the titanium alloy 6242 with pillars containing both α and β phases. However, the pillars contained only one sequence of the α-β-α structure and were highly sensitive to the β-phase morphology. This made the interpretation of the results difficult. These tests could isolate small volumes of α-β but likely not measure the effective properties of a single colony. Ding et al. [140] performed micro-cantilever beams on α-β structures of Ti64. They reported an increase in prismatic slip from 340 MPa without β [115, 141] to 480 MPa with β lathes based on experimental observations and FEM simulations of the micro-cantilever tests. This could be due to the additional anisotropy of $\vec{a}$ slip (e.g., harder $\vec{a}$ slip is happening because of the specimen and test geometry). These FIB protocols offer some addition insight into the mechanical behavior of colonies; however, the techniques

do not lend themselves for studying many orientations and alloys. This in fact can be readily accomplished with nanoindentation.

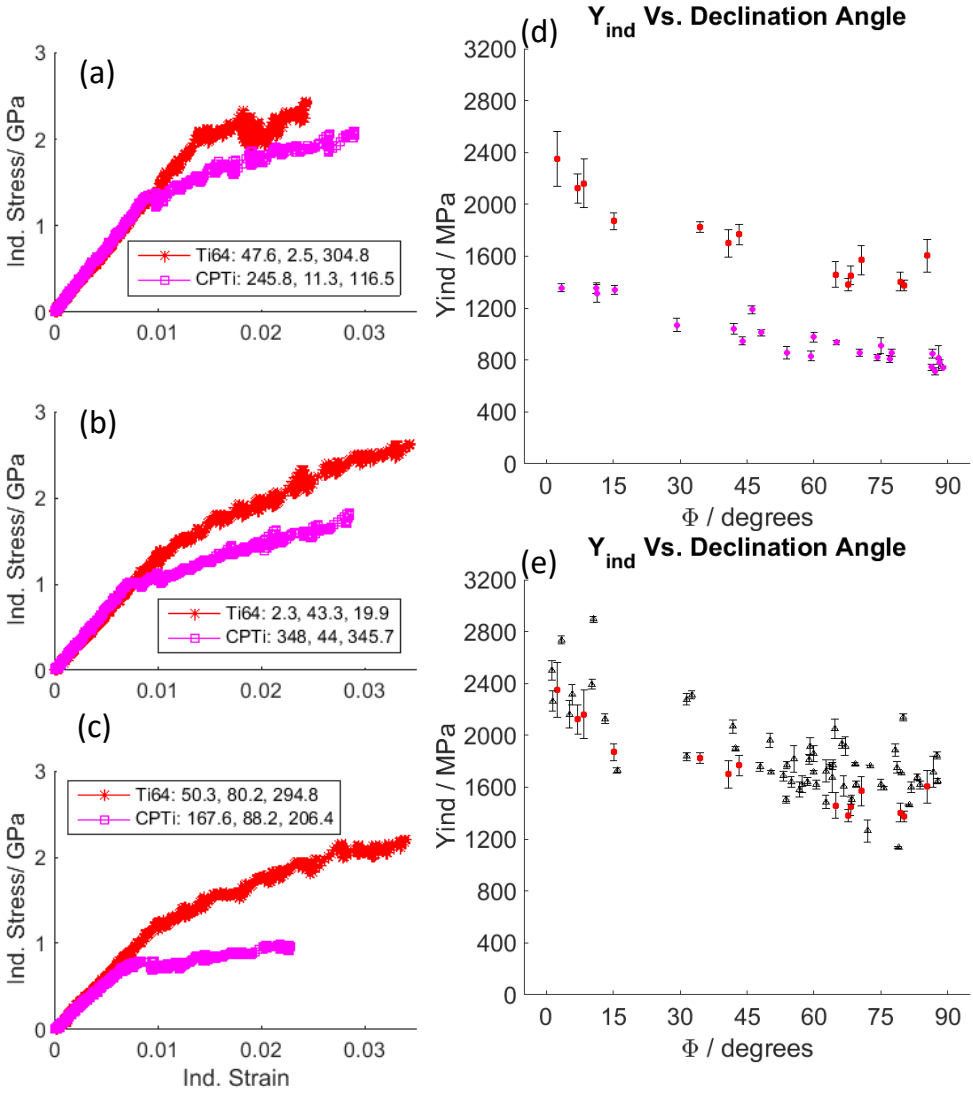

Figure 52: (a, b, c) ISS curves with a 100μm radius indenter for CP Ti (pink) and Ti64 colonies (red) for similar orientations spanning the range of declination angle (second Bunge-Euler angle listed in the legend). (d) Indentation yield strength versus declination angle for 100μm radius indenter on CP Ti (pink) and Ti64 colonies (red), (e) Indentation yield strength versus declination angle for 16μm radius indenter measurements on α-Ti64 (black) and 100μm radius indenter measurements on Ti64 colonies (red).

Chapter 8

Microindentation of Titanium Alloys

8.1 Methods and Materials

Four different materials were used for microindentation testing: Grade 2 CP Ti, Ti64 β-annealed, Ti18 β-annealed, slow cooled and aged (BASCA), and Ti18 solution treated and aged (STA). These span a range of chemical compositions, microstructures, and mechanical properties. The reason for using these different materials was to establish the robustness of microindentation stress-strain protocols for measuring differences in bulk mechanical properties. Ti64 β-annealed samples are the same ones used for nanoindentation and will be compared with nanoindentation results in order to explore the role material hierarchy (e.g., polycrystalline, multi-colony indentation site) on the indentation stress-strain response. Representative SEM and EBSD micrographs for each material are shown in Figure 53 and Figure 54. The Ti18 alloys have substantially more β-Ti than Ti64. Smith et al. [132] estimates the volume fraction of β to be 72% for STA and 48% for BASCA in comparison to Ti64 which has only 2%. The morphology of Ti18 BASCA is similar to Ti64 only it has a basket weave structure of crisscrossed α lamellae in a β matrix. Ti18 STA is comprised of small equiaxed α grains and α+β grains. STA also has microtextured zones throughout.

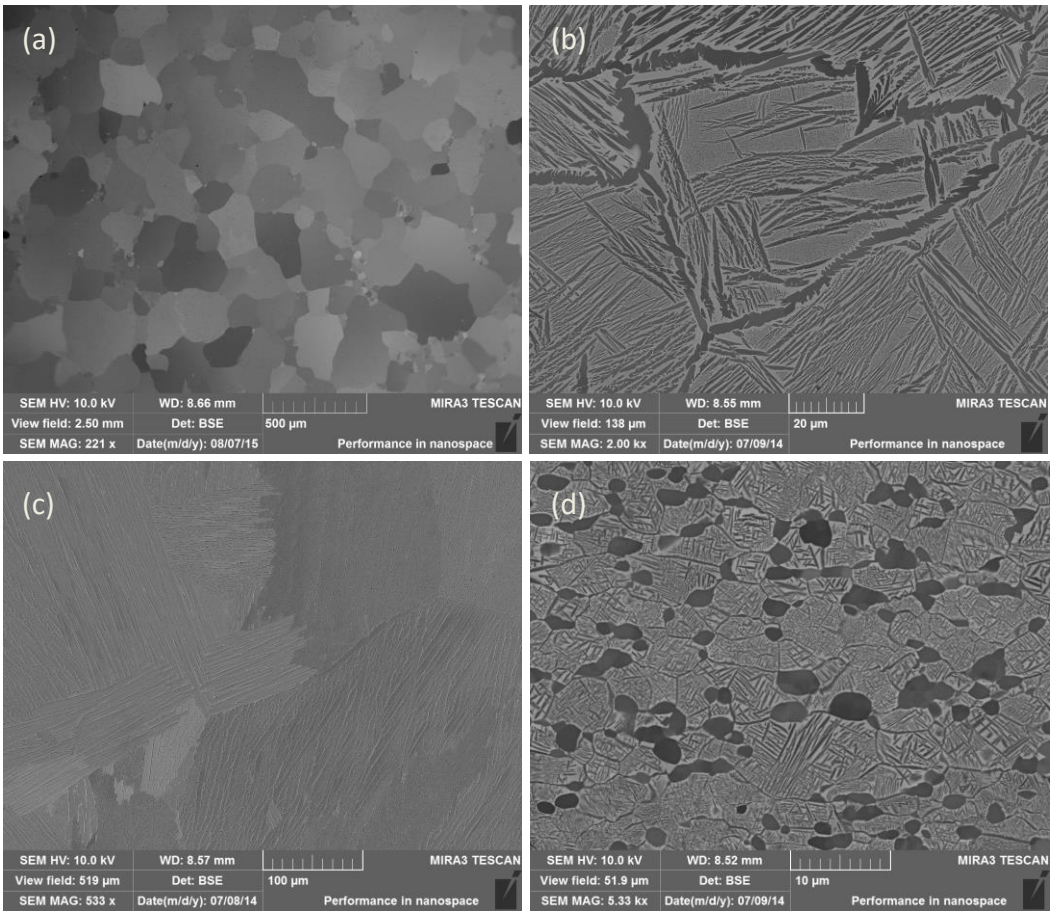

Figure 53: BSE micrographs of titanium alloys used for microindentation: (a) CP Ti, (b) Ti18 BASCA, (c) Ti64 β-annealed , (d) Ti18 STA. All images were taken on electropolished surfaces. All micrographs are from the ND plane.

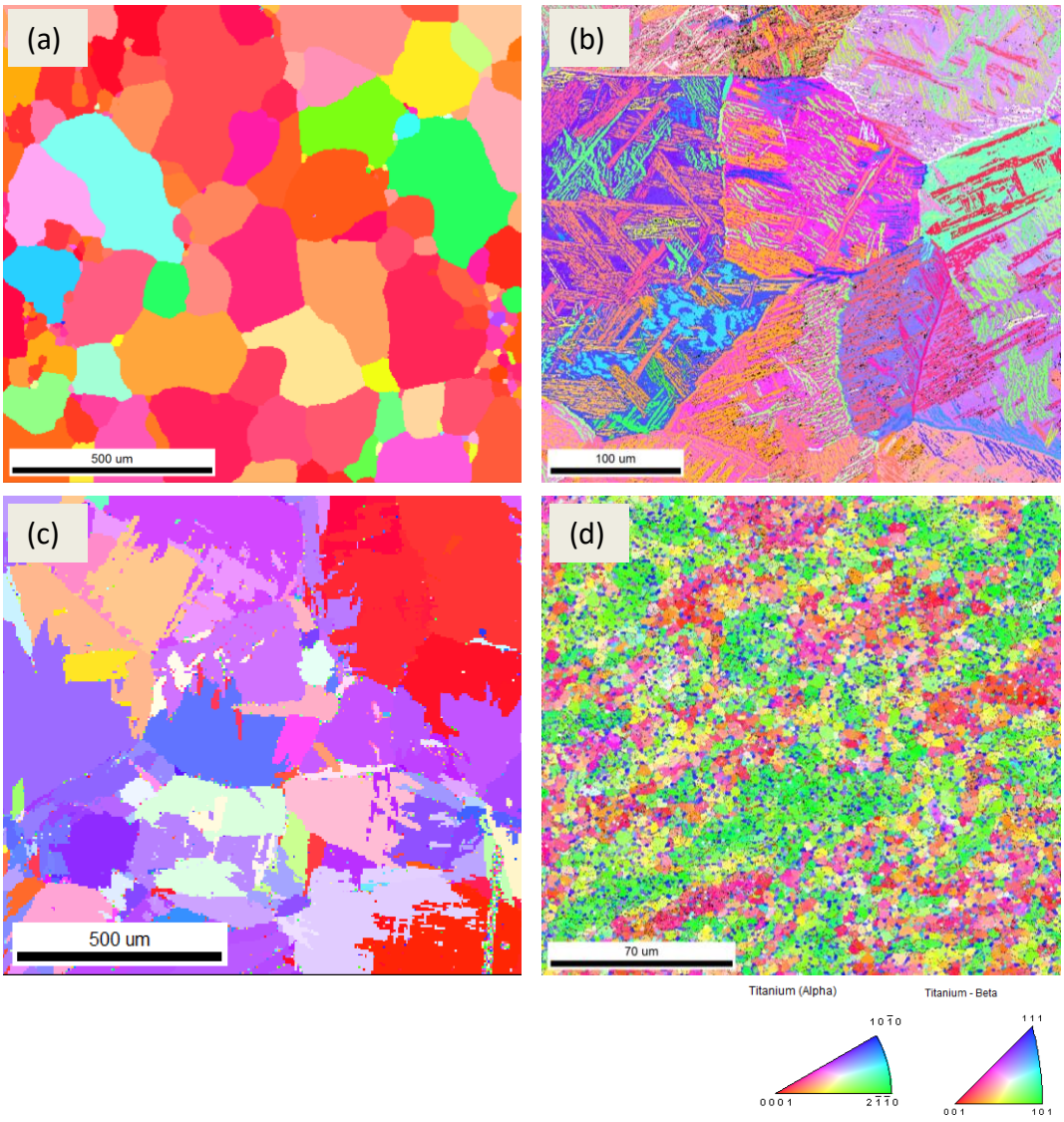

Figure 54: EBSD IPF maps of titanium alloys used for microindentation: (a) CP Ti, (b) Ti18 BASCA [132], (c) Ti64 β-annealed , (d) Ti18 STA [132]. All micrographs are from the ND plane.

The elastic properties of Ti18 STA and BASCA are expected to be lower than CP Ti and Ti64, particularly BASCA [132]. The uniaxial tensile strengths along the ND were measured by Smith et al. [132] to be 955, 1000, 1270 MPa for Ti64, Ti18 BASCA, and STA respectively. The yield strength of the CP Ti material is estimated to be half (~450 GPa) that of Ti64 [74]. These four materials contain a variety of structure morphologies

and mechanical properties for demonstrating the microindentation stress-strain protocols on titanium alloys.

A Zwicki-Roell instrumented microindenter with a maximum loading capacity of 2.5 kN was used for indentation testing. The device is a screw-driven load frame with an indenter head attached. The indenter head has a load cell and houses the indenter tip. The indentation displacement is measured by contacting the sample with a transducer foot. The relative motion between the indenter and the transducer foot provides the displacement measurement. The displacement resolution of this device is 0.02μm. This is critical for making reliable measurements during the initial elastic contact. Spherical tips with 6.35 mm and 0.5 mm radii were used for indentation. The indenter tips were made of tungsten carbide which has high hardness and stiffness. The Young's modulus and Poisson ratio of the tips were estimated to be 640 GPa and 0.22, respectively.

A typical test procedure entails specifying the prescribed displacement rate, load increment, number of cycles, and amount to unload each cycle. The majority of tests were run using a displacement rate of 0.1 mm/min and unloading 50% of the peak force of each cycle. The loading increments were chosen so that an indentation stress-strain curve with enough points could be extracted. It was adjusted depending on the indenter size and strength of the material.

A flat, parallel backside of the sample is a necessity so that the sample doesn't move or rotate and the transducer foot and indenter tip are perpendicular to the sample surface. All samples were mounted in epoxy in 2-inch diameter molds with the material exposed on the reverse side. Both sides were ground flat and parallel. Indentation surfaces were metallographically prepared with a final chemo-mechanical polish with 5

parts 0.06 μm colloidal silica and 1 part hydrogen peroxide. Samples were fastened to a precision ground hardening steel plate with a small amount of glue. The load-displacement data was analyzed following the same procedures outlined in Chapter 4 to extract indentation stress-strain curves and properties.

8.2 Results and Discussion for 0.5 mm Radius Indenter

Representative load-displacement and indentation stress-strain curves for all four materials indented with a 0.5 mm radius indenter are shown in Figure 55. The ISS curves show the highest stress for Ti18 STA and the lowest for CP Ti which is expected based on their uniaxial yield strengths. The average properties for all four materials are shown in Figure 56. The lowest average indentation modulus was on Ti18 BASCA which also had the highest β-volume fraction. The indentation modulus for Ti64 and CP Ti are in good agreement with the ranges measured with nanoindentation. It appears the bulk strength trends are captured with the 0.5 mm radius indenter. Namely Ti18 STA has the highest indentation yield strength, Ti64 and Ti18 BASCA are similar, and CP Ti is the lowest. A close look at the primary indentation zones with respect to the microstructures of each material is shown in Figure 57. Indents on CP Ti are likely to incorporate grain boundaries and multiple grains although it may still be possible to measure a single grain response. However, the indents were placed randomly so this is unlikely to have happened. The primary zone for Ti64 and Ti18 BASCA is more likely to have landed in single colonies or single basket weave grains given the large size of each in both materials. Finally the small features of Ti18 STA put many grains inside the primary zone and even a few microtextures bands.

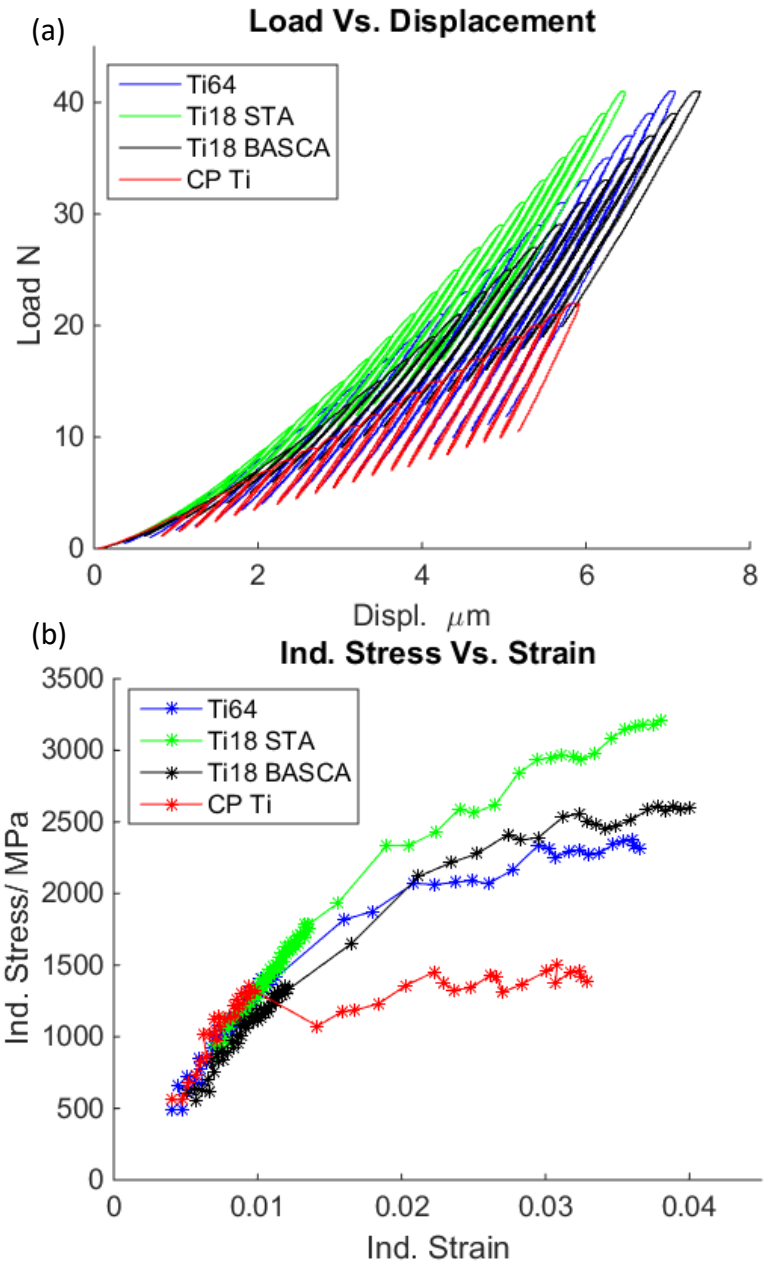

Figure 55: (a) Load versus displacement curves for all four materials with sequential unloading and (b) corresponding ISS curves. All indents were in the ND with a 0.5 mm radius tungsten-carbide indenter tip.

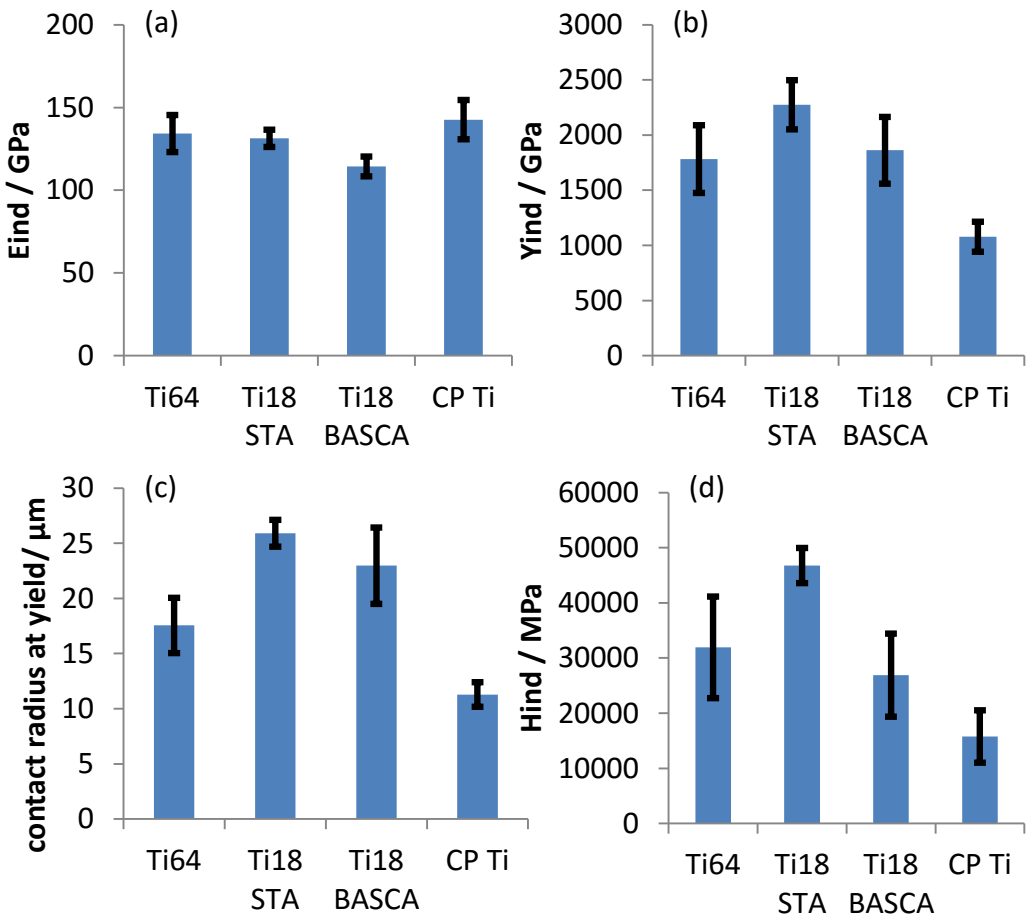

Figure 56: (a) Indentation modulus, (b) Indentation yield strength, (c) contact radius at yield, and (d) indentation initial hardening slope for all four materials with the 0.5 mm radius indenter. Values are for the averages and standard deviations of 9-12 tests randomly placed on the sample. Indents are all in the ND.

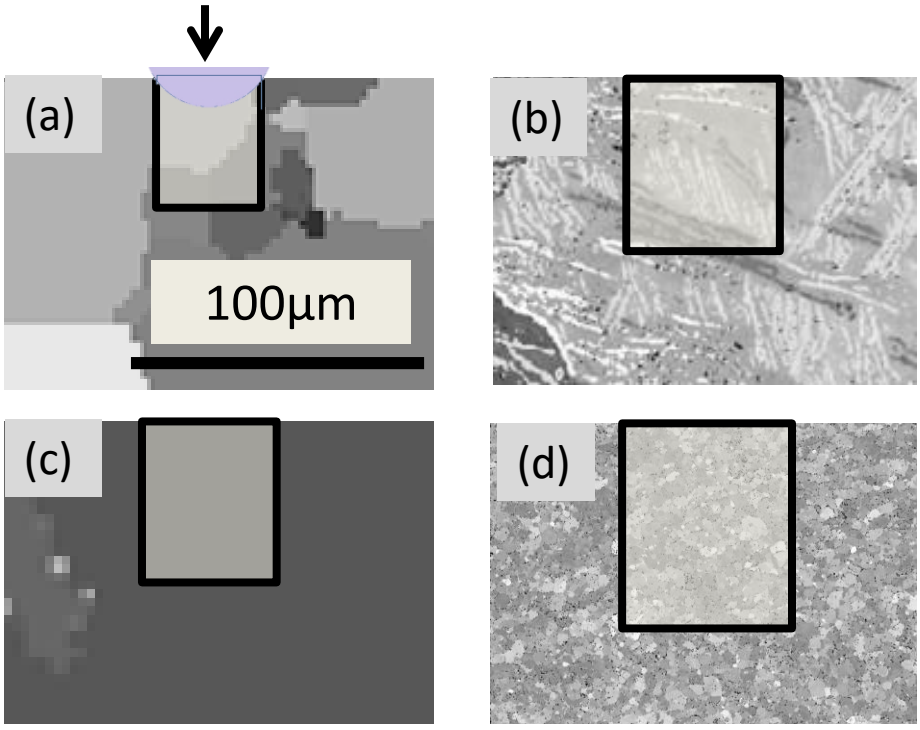

Figure 57: Primary indentation zone for (a) CP Ti, (b) Ti18 BASCA, (c) Ti64, (d) Ti18 STA.

8.3 Results and Discussion for 6.35 mm Radius Indenter

Since the 0.5 mm radius indentation experiments didn't probe many Ti64 colonies, indents using a 6.35 mm radius indenter were carried out. The same sample and test protocols were used for both 0.5 and 6.35 mm radius indenter tests. The only difference was the loading increments and number of cycles. Figure 58 shows the load-displacement and indentation stress-strain curves for 6 tests in Ti64 using the 6.35 mm radius indenter. The primary indentation zone at yield is also illustrated in Figure 58 showing that these indentation tests cover many colonies. The average properties are given in Table **5**. The indentation modulus and yield strengths compare well with nanoindentation and 0.5 mm radius microindentation results.

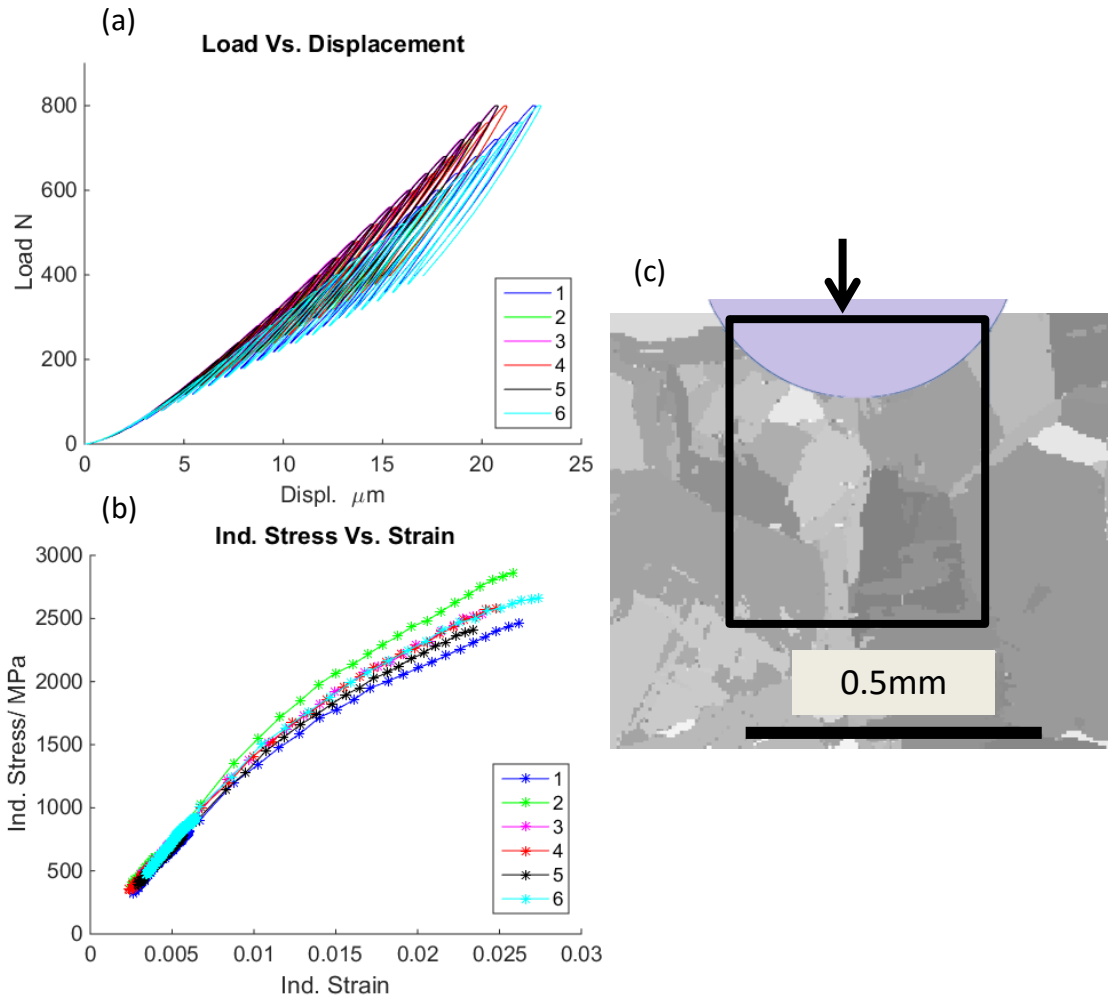

Figure 58: (a) Load versus displacement curves for 6 tests on Ti64 with sequential unloading and (b) corresponding ISS curves. All indents were in the ND with a 6.35 mm radius tungsten-carbide indenter tip. (c) Primary indentation zone for Ti64.

Table 5: Indentation stress-strain measurements for Ti64 β-annealed with a 6.35 mm radius indenter

	E_{ind} [GPa]	Y_{ind} [MPa]	a_{yield} [μm]	H_{ind} [MPa]
Average	127.1	1865	222.2	63,057
Standard Dev.	7.0	184	14.8	6,522
Maximum	112.6	1463	194.1	51,193
Minimum	137.1	2158	246.0	74,788

There appears to be a distinct difference in the initial indentation hardening between 0.5 and 6.35 mm indents. Figure 59 shows representative load-displacement and ISS curves for both indenter sizes. The initial hardening is much higher for the larger

indenter size. The 6.35 mm indents have many colony orientations and boundaries in them. It is likely that the colony boundaries impede dislocation motion and amplify dislocation multiplication. This could be due to the heterogeneity and mismatch at colony boundaries.

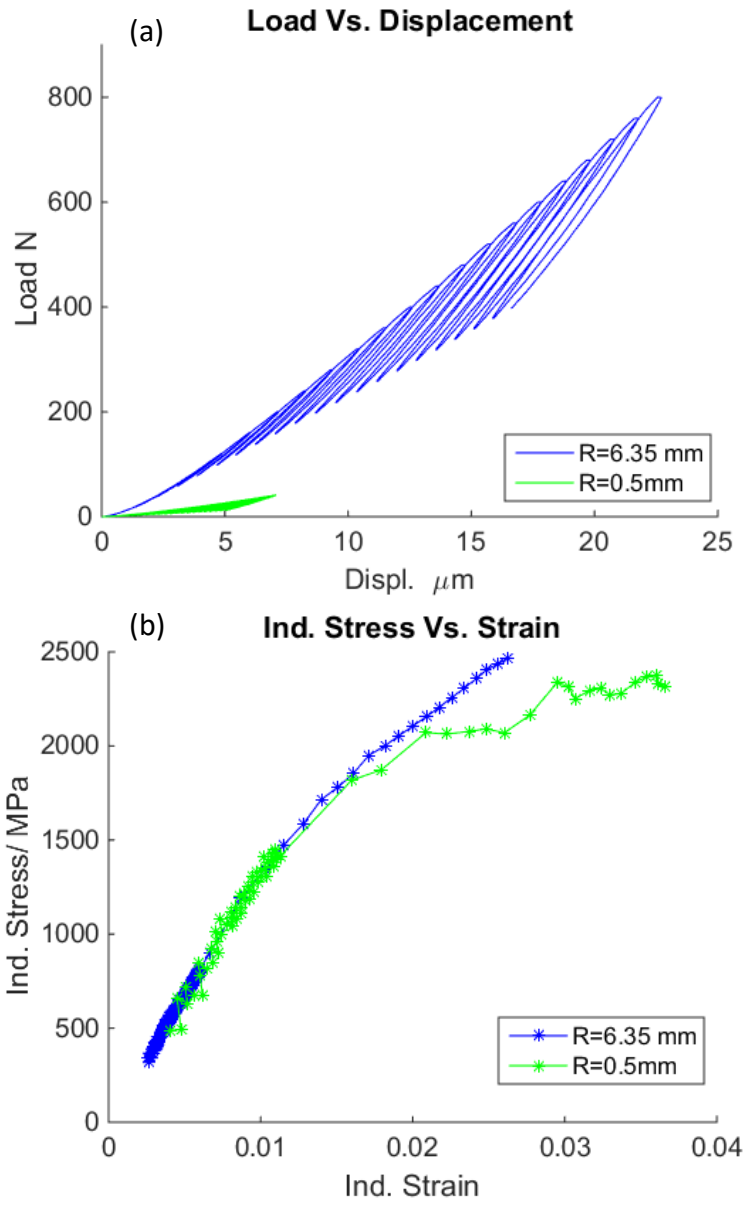

Figure 59: (a) Load-displacement curves for 0.5 and 6.35 mm radius indents on Ti64 and (b) corresponding ISS curves.

While the 6.35 mm indents cover multiple colonies, they are structurally still not the same as bulk tests. This is evident by considering different window sizes on an EBSD IPF map. Figure 60 illustrates a large scan area and a smaller scan area relevant to microindentation with the 6.35 mm indenter. The elastic modulus was calculated using the Hill model using Mtex [142]with elastic constants from [116]. The elastic modulus of the large scan area (124 GPa) is theoretically closer to the Young's modulus from bulk uniaxial tests (114 GPa). This difference is likely due to the basal texture in the sample ND. The smaller window size representative of microindentation tests will produce higher and lower values depending on the structure at the indentation site. This is evident by the higher elastic modulus (131 GPa) for the smaller scan area in Figure 60 with a large area fraction of colonies oriented near the c-axis. The microindentation property variation is likely due the structure variation at this length scale and not just experimental scatter.

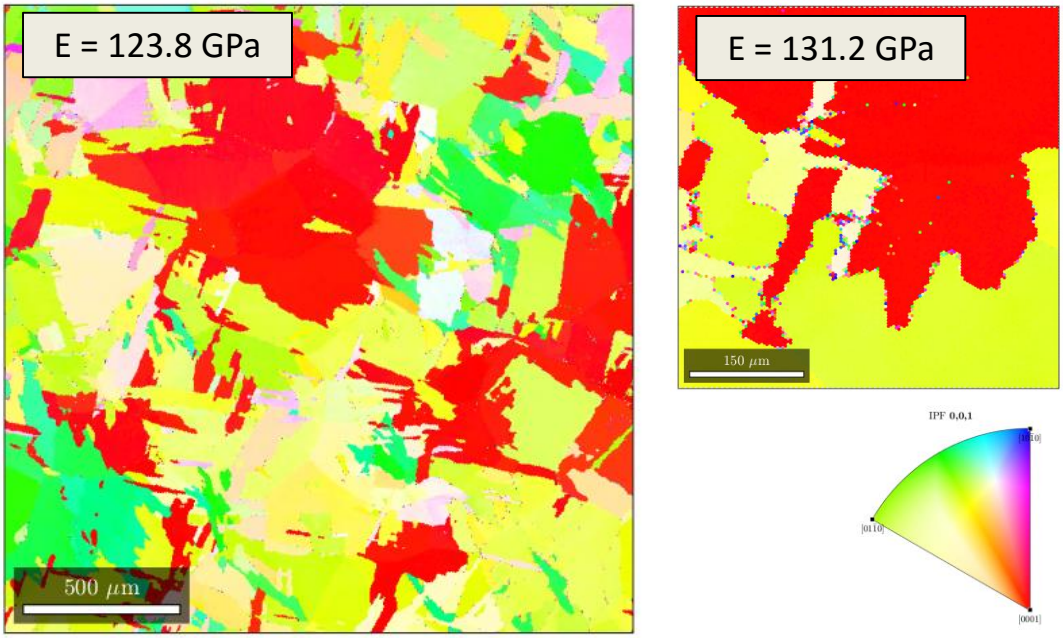

Figure 60: Two different EBSD IPF micrographs for Ti64 and the calculated elastic modulus from the Hill model. The smaller micrograph is characteristic of the indentation zone for 6.35 mm radius indents.

Chapter 9

Discussion of Hierarchical and High Throughput Mechanical Characterization of Ti64

This chapter summarizes the indentation measurements made at multiple lengths scales in Ti64. The lowest length scale tested corresponded to α-Ti64 with a 16.5 μm radius indenter. These tests were done on an altered sample (heat treated) to provide slightly larger α-Ti64 features than in Ti64 in the β-annealed condition. However, the chemical composition and crystalline structures are the same which allows the measurements to be used to estimate the properties of α-Ti64 in β-annealed samples. All other indents with100 μm, 0.5 mm, and 6.35 mm indenter tip radii were done on β-annealed samples. A change in the indenter tip size also changes the primary indentation zone size or the volume of material probed by indentation. The 100 μm indents measured the properties of single colonies, the 0.5 mm indents were at a threshold between single colonies and multiple colonies, and the 6.35 mm indents covered many colonies. It is emphasized that all the experiments were done with polycrystalline samples. The intense effort involved in making single crystal specimens was avoided in this work. Additionally, all samples were prepared using careful metallographic techniques of sectioning, grinding, and polishing. This is much less effort compared to FIB machining of pillars or cantilevers. The high throughput nature of indentation testing makes it a method of choice for rapidly ascertaining materials knowledge.

The pitfalls of indentation testing that were discussed in Chapter 2 were overcome with more sophisticated indentation protocols that allowed for reliable measurements in

the form of indentation stress-strain curves. In order to make indentation measurements from 16μm to 6.35mm radii indenters, two indentation testing machines had to be utilized. The combination of nano and microindentation stress-strain curves with various indenter sizes on Ti64 offers a unique perspective on the hierarchical structure-property relationships. Figure 61 shows the trend in indentation modulus with the indenter size plotted against the primary indentation zone diameter. The average indentation modulus increases when going from α-Ti64 to α+β Ti64 and remains relatively constant up through multiple colony indentation tests. The relatively constant average indentation modulus between indents on single colonies and multiple colonies is expected since there are no structural changes that would influence the modulus (e.g., vol. fraction of phases). The range only goes down a small amount between single colony (100 μm) and multiple colony measurements (6.35 mm) since the effects of texture still create volumes with high volume fractions of colonies aligned with the α-phase c-axis.

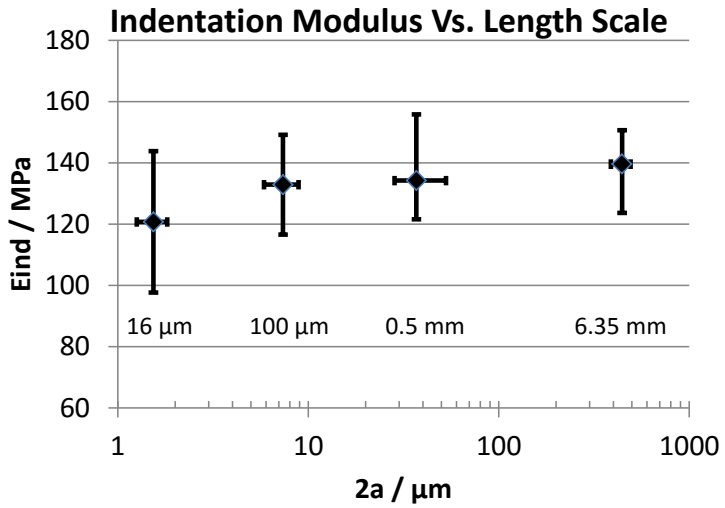

Figure 61: Average indentation modulus measured with four different indenter sizes in Ti64 versus the contact diameter at yield. The error bars represent the minimum and maximum values for each indenter size. The isotropic equivalent indentation modulus (E=113 GPa, v = 0.32) is ~ 126 GPa.

Figure 62 shows the trends of indentation yield strength with material length scale. From these measurements it appears that β-Ti64 has little effect on the indentation yield strength. The indentation yield strength and anisotropy of α-Ti64 is controlling the indentation strength for multiphase indentation experiments. There also seems to be little change in the average strength going from single colonies to multiple colonies. This would indicate the colony boundaries have a minimal effect on indentation strength. The range in strength decreases with each indenter size increase. At the lowest length scale, the range is dictated by the anisotropy of single crystal plasticity. Very high indentation strengths are measured for the extreme case of indenting on the c-axis and very low indentation strengths are measured for fully declined α-Ti64. Similarly high and low strengths are measured for indents on single colonies for the same α-phase orientations. Microindentation tests which include multiple colonies (6.35 mm radius indenter) have the lowest range due to the homogenization of single crystals and colonies. These results appear to show little size or structure effects other than the α-Ti64 crystal orientation. This would indicate that nanoindentation stress-strain curves can be used to estimate bulk strengths for this material system. The initial indentation hardening slope changed drastically from single and few colony measurements to multiple colony measurements as show in Figure 63. The increased hardening rates in the large indentation zones can be attributed to the role of colony boundaries. It is hypothesized that these impede dislocations and enhance dislocation multiplication. The complex structure and stress states at heterogeneity stresses at the colony boundaries are likely to be responsible for these effects.

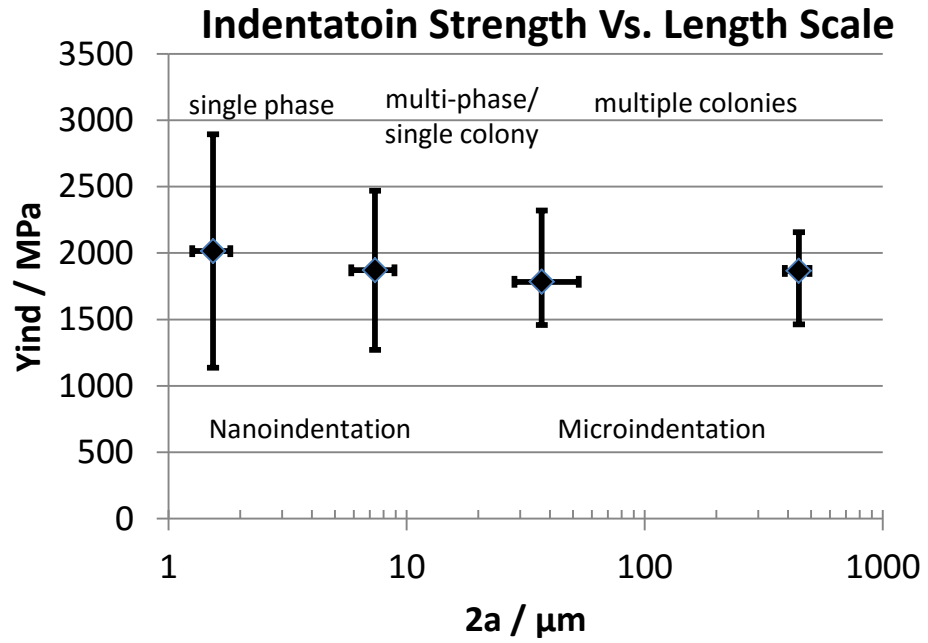

Figure 62: Average indentation yield strength measured with four different indenter sizes in Ti64. The error bars represent the minimum and maximum strengths and contact diameters at yield measured with each indenter size. The uniaxial tensile yield strength of the material tested is ~955 MPa.

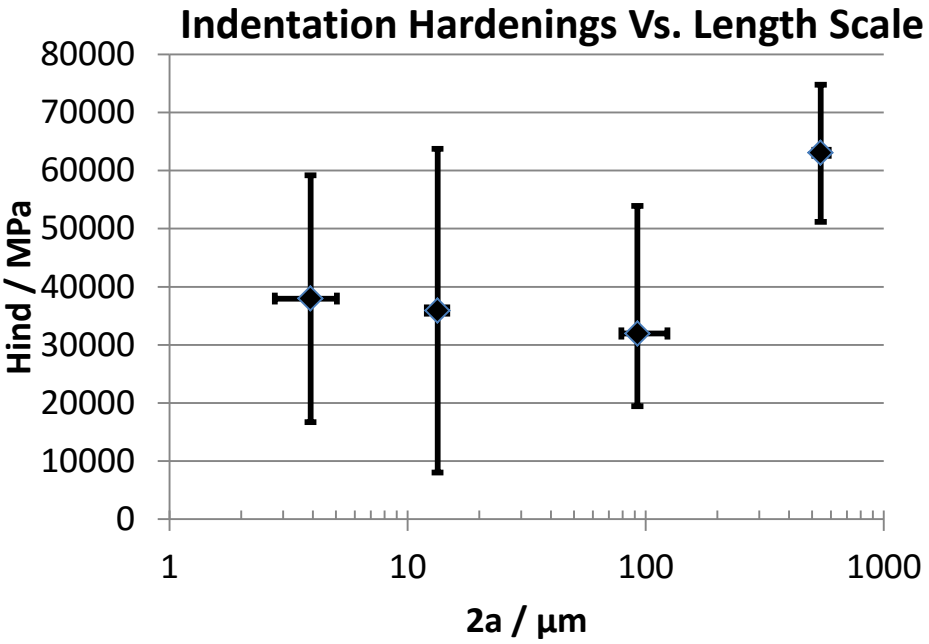

Figure 63: Average indentation initial hardening measured with four different indenter sizes in Ti64 versus the average contact diameter. The error bars represent the minimum and maximum values with each indenter size.

CHAPTER 10

Conclusions

A high throughput hierarchical mechanical characterization protocol was demonstrated on Ti64. This protocol employed recent advances in spherical nanoindentation protocols. Further advancements and new protocols were developed in order to apply them to a more complex material system and a wider range of material length scales. The main conclusions from this dissertation are summarized below:

i. The current work using the spherical indentation stress-strain protocols in metals has covered a limited range of complexity. Some of the assumptions and choices used are likely not to valid for a broader range of sample materials and indenter sizes and materials. These assumptions were identified and addressed by applying CSM corrections, accounting for the indenter tip displacement in the determination of indentation strain, and using a strain offset for measuring indentation yield strength. These changes were needed to make hierarchical measurements in a more complex material system. The robustness of the spherical indentation protocols was increased so that a broader class of materials and experiments could be introduced.

ii. The spherical nanoindentation protocols used in this thesis require the identification of the initial elastic loading segment. In many cases there are multiple solutions which create uncertainty in the measured indentation properties. Important metrics which quantify the initial elastic segment were introduced and recorded to serve as a way for standardizing the process. The

uncertainty in the ISS curve and indentation properties was also estimated by systematically analyzing multiple answers for individual tests. The uncertainty in a single measurement is relatively the same as the uncertainty measured from multiple tests of the same feature.

iii. This study was the first application of the spherical nanoindentation protocols to measure the grain scale elastic and plastic anisotropy in an hcp material. The anisotropy was measured in the form of indentation modulus and yield strength using a combination of nanoindentation and EBSD measurements with a polycrystalline sample. The anisotropy observed in these properties closely matches the available literature on the single crystal properties of CP Ti and alloyed α-Ti. These indentation protocols are able to capture the elastic and plastic anisotropy of hcp α-Ti without the effort of making single crystals.

iv. Changes in properties with chemical composition are an important aspect of materials knowledge in advanced alloys. This study was also the first time the spherical nanoindentation protocols were used to capture this type of knowledge. The measurements on α-Ti64 showed a decrease in indentation modulus and an increase in indentation yield strength across all orientations compared to CP Ti. The indentation modulus measurements were in agreement with single crystal Ti6Al acoustic measurements, and the increase in indentation strength was in good agreement with the single crystal properties of similar chemical compositions of α-titanium. These protocols were able to measure the chemical composition – property measurements in α-Ti without the effort of making single crystals.

v. Many structural alloys are multiphase. This presents a level of structural hierarchy that requires thorough characterization. Spherical indentation protocols were extended to capture the elastic and plastic anisotropy of a two-phase colony microstructure by careful consideration of the colony α-phase orientation and measurements of indentation modulus and yield strength. The indentation yield strength did not change between α-Ti64 and α-β Ti64 indentation. This supports the observations in literature that slip transfer readily occurs at the α-β interface which would reduce its effect on increasing the indentation yield strength. These protocols are capable of capturing structure-property relationships at a two-phase level of structural hierarchy in an advanced alloy.

vi. A third level of structural hierarchy in advanced alloys is polycrystalline structures. Indentation testing at this length scales requires higher load capacity and a different set of protocols. Microindentation stress-strain protocols using the advances in nanoindentation protocols were developed to capture the indentation stress-strain response of polycrystalline volumes. The trends in the indentation properties at this length scale matched bulk trends of modulus and yield strength.

vii. Sophisticated indentation stress-strain protocols used to make measurements across multiple levels of structural hierarchy and length scale in a high throughput manner were developed. The demonstration on Ti64 showed that the indentation yield strength measurements for small volumes of material are comparable to polycrystalline measurements. The differences were mainly

due to the change in structure in the indentation zone (e.g., anisotropy and homogenization) and not indentation size effects. This unique dataset was collected without the effort of single crystal samples or FIB machining with a significant reduction of the amount of material and time compared to conventional protocols. The datasets that can be collected with these protocols can provide the information necessary to advance microstructure models and homogenization theories.

CHAPTER 11

Future Work

The recommended future work can be broken into FEM simulations, InSEM-nanoindentation experiments, nanoindentation experiments on Ti18, and high throughput process-structure-property exploration using microindentation. The nanoindentation experiments at the single phase and single colony length scales in Ti-6Al-4V provide local measurements with which crystal plasticity models can be calibrated. In order to do this, indentation on different crystal and colony orientations has to be performed. In addition to the load-displacement response, there is now an indentation stress-strain measurement which contains the elastic-plastic transition and much richer information about the material response. Parameters for crystal plasticity models can then be estimated by comparing experimental and finite element ISS curves. The full potential of the nanoindentation datasets can only be achieved with a strong modeling effort.

Since it was unclear if twinning is occurring during the early stages of loading, there should be some additional experimental investigation. Cross-sectional TEM at the indentation site for indentation tests stopped right after yield could potentially provide some answers; however, this is a very laborious task. InSEM indentation could also provide insight for less effort. Nanoindentation and EBSD at the edge of samples where the material underneath the indenter can be imaged while the load is applied is now possible with the facilities at Georgia Tech. Such experiments would allow for a better understanding of the deformation that occurs under the indenter tip, particularly the occurrence of twinning.

There appeared to be little change in indentation strength going from α-Ti64 to α+β Ti64. This is only one morphology of the β-phase in Ti alloys. Ti18 on the other hand has a range of higher volume fractions and different morphology of the β-phase. Similar hierarchical nanoindentation experiments to those performed in Ti64 could ascertain the role that the β-phase plays in the mechanical performance of Ti18, particularly going from BASCA to STA samples where there is an increase in macroscopic strength. This can be readily accomplished with the protocols developed in this dissertation.

Finally, the demonstration of microindentation indentation stress-strain measurements to capture structure-property relationships in polycrystalline volumes of titanium alloys opens the possibility for combinatorial process-structure-property studies. These approaches have been used in the other sciences to quickly discovery new materials and obtain knowledge for decision making. Such efforts are crucial to reducing the time and effort for discovery and developing new, advanced materials. The workflow of such a study using the microindentation protocols in this dissertation would entail: 1) creating an assay of material that contains instantiations representative of many process conditions using thermal and mechanical gradients, 2) characterizing the structure as a function of these process conditions, and 3) mechanically characterizing the material using microindentation stress-strain measurements with the appropriate indenter size so that the indentation zone contains a polycrystalline volume that is also representative of a single process (i.e., negligible process gradient in the indentation zone). Each step is a reduction in the time, material, and effort in the path typically taken to assess macroscopic processing-structure-property relationships in structural alloys. This could

provide a much needed high throughput protocol for collecting new materials knowledge in advanced alloys.

REFERENCES

1. Lakes, R., *MATERIALS WITH STRUCTURAL HIERARCHY.* Nature, 1993. **361**(6412): p. 511-515.
2. Fratzl, P. and R. Weinkamer, *Nature's hierarchical materials.* Progress in Materials Science, 2007. **52**(8): p. 1263-1334.
3. Meyers, M.A., et al., *Biological materials: Structure and mechanical properties.* Progress in Materials Science, 2008. **53**(1): p. 1-206.
4. Weiner, S. and H.D. Wagner, *The material bone: Structure mechanical function relations.* Annual Review of Materials Science, 1998. **28**: p. 271-298.
5. Espinosa, H.D., et al., *Merger of structure and material in nacre and bone - Perspectives on de novo biomimetic materials.* Progress in Materials Science, 2009. **54**(8): p. 1059-1100.
6. Barthelat, F., et al., *On the mechanics of mother-of-pearl: A key feature in the material hierarchical structure.* Journal of the Mechanics and Physics of Solids, 2007. **55**(2): p. 306-337.
7. Amada, S., et al., *Fiber texture and mechanical graded structure of bamboo.* Composites Part B-Engineering, 1997. **28**(1-2): p. 13-20.
8. Zhang, Z.Q., Y.W. Zhang, and H.J. Gao, *On optimal hierarchy of load-bearing biological materials.* Proceedings of the Royal Society B-Biological Sciences, 2011. **278**(1705): p. 519-525.
9. Gao, H.J., et al., *Materials become insensitive to flaws at nanoscale: Lessons from nature.* Proceedings of the National Academy of Sciences of the United States of America, 2003. **100**(10): p. 5597-5600.
10. Wegst, U.G.K., et al., *Biomaterials by freeze casting.* Philosophical Transactions of the Royal Society a-Mathematical Physical and Engineering Sciences, 2010. **368**(1917): p. 2099-2121.
11. Bonderer, L.J., A.R. Studart, and L.J. Gauckler, *Bioinspired design and assembly of platelet reinforced polymer films.* Science, 2008. **319**(5866): p. 1069-1073.
12. Launey, M.E., et al., *Designing highly toughened hybrid composites through nature-inspired hierarchical complexity.* Acta Materialia, 2009. **57**(10): p. 2919-2932.
13. Munch, E., et al., *Tough, Bio-Inspired Hybrid Materials.* Science, 2008. **322**(5907): p. 1516-1520.
14. Ashby, M.F., et al., *THE MECHANICAL-PROPERTIES OF NATURAL MATERIALS .1. MATERIAL PROPERTY CHARTS.* Proceedings of the Royal Society-Mathematical and Physical Sciences, 1995. **450**(1938): p. 123-140.
15. Wegst, U.G.K. and M.F. Ashby, *The mechanical efficiency of natural materials.* Philosophical Magazine, 2004. **84**(21): p. 2167-2181.
16. Oliver, W.C. and G.M. Pharr, *Measurement of hardness and elastic modulus by instrumented indentation: Advances in understanding and refinements to methodology.* Journal of Materials Research, 2004. **19**(1): p. 3-20.

17. Uchic, M.D. and D.M. Dimiduk, *A methodology to investigate size scale effects in crystalline plasticity using uniaxial compression testing.* Materials Science and Engineering A, 2005. **400-401**(1-2 SUPPL.): p. 268-278.
18. Sharpe, W.N., et al., *Tensile testing of MEMS materials - recent progress.* Journal of Materials Science, 2003. **38**(20): p. 4075-4079.
19. Wu, B., A. Heidelberg, and J.J. Boland, *Mechanical properties of ultrahigh-strength gold nanowires.* Nature Materials, 2005. **4**(7): p. 525-529.
20. Kiener, D., et al., *FIB damage of Cu and possible consequences for miniaturized mechanical tests.* Materials Science and Engineering A, 2007. **459**(1-2): p. 262-272.
21. Frick, C.P., et al., *Size effect on strength and strain hardening of small-scale 111 nickel compression pillars.* Materials Science and Engineering a-Structural Materials Properties Microstructure and Processing, 2008. **489**(1-2): p. 319-329.
22. Shan, Z.W., et al., *Mechanical annealing and source-limited deformation in submicrometre-diameter Ni crystals.* Nat Mater, 2008. **7**(2): p. 115-119.
23. Bei, H., et al., *Compressive strengths of molybdenum alloy micro-pillars prepared using a new technique.* Scripta Materialia, 2007. **57**(5): p. 397-400.
24. Zhang, P., S.X. Li, and Z.F. Zhang, *General relationship between strength and hardness.* Materials Science and Engineering: A, 2011. **529**: p. 62-73.
25. Alcala, J., A.E. Giannakopoulos, and S. Suresh, *Continuous measurements of load-penetration curves with spherical microindenters and the estimation of mechanical properties.* Journal of Materials Research, 1998. **13**(5): p. 1390-1400.
26. Giannakopoulos, A.E. and S. Suresh, *Determination of elastoplastic properties by instrumented sharp indentation.* Scripta Materialia, 1999. **40**(10): p. 1191-1198.
27. Dao, M., et al., *Computational modeling of the forward and reverse problems in instrumented sharp indentation.* Acta Materialia, 2001. **49**(19): p. 3899-3918.
28. Bucaille, J.L., et al., *Determination of plastic properties of metals by instrumented indentation using different sharp indenters.* Acta Materialia, 2003. **51**(6): p. 1663-1678.
29. Tabor, D., *The hardness of metals*. 1951, Oxford,: Clarendon Press. ix, 175 p.
30. Field, J.S. and M.V. Swain, *Determining the mechanical properties of small volumes of material from submicrometer spherical indentations.* Journal of Materials Research, 1995. **10**(1): p. 101-112.
31. Kalidindi, S.R. and S. Pathak, *Determination of the effective zero-point and the extraction of spherical nanoindentation stress-strain curves.* Acta Materialia, 2008. **56**(14): p. 3523-3532.
32. Basu, S., A. Moseson, and M.W. Barsoum, *On the determination of spherical nanoindentation stress-strain curves.* Journal of Materials Research, 2006. **21**(10): p. 2628-2637.
33. Herbert, E.G., et al., *On the measurement of stress-strain curves by spherical indentation.* Thin Solid Films, 2001. **398**: p. 331-335.
34. Murty, K.L., et al., *Nondestructive determination of tensile properties and fracture toughness of cold worked A36 steel.* International Journal of Pressure Vessels and Piping, 1998. **75**(11): p. 831-840.
35. Pathak, S. and S.R. Kalidindi, *Spherical nanoindentation stress-strain curves.* Materials Science & Engineering R-Reports, 2015. **91**: p. 1-36.

36. Pathak, S., et al., *Studying grain boundary regions in polycrystalline materials using spherical nano-indentation and orientation imaging microscopy.* Journal of Materials Science, 2012. **47**(2): p. 815-823.
37. Kalidindi, S.R., S. Pathak, and D. Stojakovic, *Measurement of the local mechanical properties in polycrystalline samples using spherical nanoindentation and orientation imaging microscopy.* Acta Materialia, 2009. **57**(10): p. 3020-3028.
38. Kalidindi, S.R. and S.J. Vachhani, *Mechanical characterization of grain boundaries using nanoindentation.* Current Opinion in Solid State & Materials Science, 2014. **18**(4): p. 196-204.
39. Vachhani, S.J. and S.R. Kalidindi, *Grain-scale measurement of slip resistances in aluminum polycrystals using spherical nanoindentation.* Acta Materialia, 2015. **90**: p. 27-36.
40. Brinell, J.A., Second Cong. Int. Methodes d'Essai, Paris, 1900.
41. ASTM International, *Standard Test Method for Brinell Hardness of Metallic Materials*, in *E10-12*. 2015: West Conshohocken, PA.
42. ASTM International, *Standard Test Method for Knoop and Vickers Hardness of Materials*, in *E384*. 2015: West Conshohocken, PA.
43. Oliver, W.C. and G.M. Pharr, *AN IMPROVED TECHNIQUE FOR DETERMINING HARDNESS AND ELASTIC-MODULUS USING LOAD AND DISPLACEMENT SENSING INDENTATION EXPERIMENTS.* Journal of Materials Research, 1992. **7**(6): p. 1564-1583.
44. Bhushan, X.L.A.B., *A review of nanoindentation continuous stiffness measurement technique and its applications.* Materials Characterization, 2002(48): p. 11-36.
45. J. Hay, P.A., and E. Herbert, *CONTINUOUS STIFFNESS MEASUREMENT DURING INSTRUMENTED INDENTATION TESTING.* EXPERIMENTAL TECHNIQUES, 2010. **86**.
46. Yu, W. and J.P. Blanchard, *An elastic-plastic indentation model and its solutions.* Journal of Materials Research, 1996. **11**(09): p. 2358-2367.
47. Hill, R., B. Storakers, and A.B. Zdunek, *A THEORETICAL-STUDY OF THE BRINELL HARDNESS TEST.* Proceedings of the Royal Society of London Series a-Mathematical Physical and Engineering Sciences, 1989. **423**(1865): p. 301-330.
48. Johnson, K.L., *The correlation of indentation experiments.* Journal of the Mechanics and Physics of Solids, 1970. **18**(2): p. 115-126.
49. Hill, R., E.H. Lee, and S.J. Tupper, *The Theory of Wedge Indentation of Ductile Materials.* Proceedings of the Royal Society of London A: Mathematical, Physical and Engineering Sciences, 1947. **188**(1013): p. 273-289.
50. Mesarovic, S.D. and N.A. Fleck, *Spherical indentation of elastic–plastic solids.* Proceedings of the Royal Society of London A: Mathematical, Physical and Engineering Sciences, 1999. **455**(1987): p. 2707-2728.
51. Field, J.S. and M.V. Swain, *A SIMPLE PREDICTIVE MODEL FOR SPHERICAL INDENTATION.* Journal of Materials Research, 1993. **8**(2): p. 297-306.
52. Hertz, H., D.E. Jones, and G.A. Schott, *Miscellaneous papers*. 1896, London, New York,: Macmillan and co. xxvi, 340 p.

53. Johnson, K.L., *Contact mechanics*. 1985, Cambridge Cambridgeshire ; New York: Cambridge University Press. xi, 452 p.
54. Donohue, B.R., A. Ambrus, and S.R. Kalidindi, *Critical evaluation of the indentation data analyses methods for the extraction of isotropic uniaxial mechanical properties using finite element models.* Acta Materialia, 2012. **60**(9): p. 3943-3952.
55. Pathak, S., J. Shaffer, and S.R. Kalidindi, *Determination of an effective zero-point and extraction of indentation stress-strain curves without the continuous stiffness measurement signal.* Scripta Materialia, 2009. **60**(6): p. 439-442.
56. Willis, J.R., *Hertzian Contact of Anisotropic Bodies.* Journal of the Mechanics and Physics of Solids, 1966. **14**(3): p. 163-&.
57. Vlassak, J.J. and W.D. Nix, *Indentation Modulus of Elastically Anisotropic Half-Spaces.* Philosophical Magazine a-Physics of Condensed Matter Structure Defects and Mechanical Properties, 1993. **67**(5): p. 1045-1056.
58. Vlassak, J.J. and W.D. Nix, *MEASURING THE ELASTIC PROPERTIES OF ANISOTROPIC MATERIALS BY MEANS OF INDENTATION EXPERIMENTS.* Journal of the Mechanics and Physics of Solids, 1994. **42**(8): p. 1223-1245.
59. Vlassak, J.J., et al., *The indentation modulus of elastically anisotropic materials for indenters of arbitrary shape.* Journal of the Mechanics and Physics of Solids, 2003. **51**(9): p. 1701-1721.
60. Swadener, J.G. and G.M. Pharr, *Indentation of elastically anisotropic half-spaces by cones and parabolae of revolution.* Philosophical Magazine a-Physics of Condensed Matter Structure Defects and Mechanical Properties, 2001. **81**(2): p. 447-466.
61. Gao, Y.F. and G.M. Pharr, *Multidimensional contact moduli of elastically anisotropic solids.* Scripta Materialia, 2007. **57**(1): p. 13-16.
62. Patel, D.K., H.F. Al-Harbi, and S.R. Kalidindi, *Extracting single-crystal elastic constants from polycrystalline samples using spherical nanoindentation and orientation measurements.* Acta Materialia, 2014. **79**: p. 108-116.
63. Nix, W.D. and H.J. Gao, *Indentation size effects in crystalline materials: A law for strain gradient plasticity.* Journal of the Mechanics and Physics of Solids, 1998. **46**(3): p. 411-425.
64. Swadener, J.G., E.P. George, and G.M. Pharr, *The correlation of the indentation size effect measured with indenters of various shapes.* Journal of the Mechanics and Physics of Solids, 2002. **50**(4): p. 681-694.
65. Huang, Y., et al., *A model of size effects in nano-indentation.* Journal of the Mechanics and Physics of Solids, 2006. **54**(8): p. 1668-1686.
66. Pharr, G.M., E.G. Herbert, and Y.F. Gao, *The Indentation Size Effect: A Critical Examination of Experimental Observations and Mechanistic Interpretations.* Annual Review of Materials Research, Vol 40, 2010. **40**: p. 271-292.
67. Greer, J.R. and J.T.M. De Hosson, *Plasticity in small-sized metallic systems: Intrinsic versus extrinsic size effect.* Progress in Materials Science, 2011. **56**(6): p. 654-724.
68. Pathak, S., et al., *Understanding pop-ins in spherical nanoindentation.* Applied Physics Letters, 2014. **105**(16).

69. Morris, J.R., et al., *Size Effects and Stochastic Behavior of Nanoindentation Pop In.* Physical Review Letters, 2011. **106**(16).
70. Shim, S., et al., *A different type of indentation size effect.* Scripta Materialia, 2008. **59**(10): p. 1095-1098.
71. Pathak, S., et al., *Improved analysis of bone nano-mechanical properties using a novel nanoindentation technique.* Journal of Bone and Mineral Research, 2007. **22**: p. S480-S480.
72. Phani, P.S., et al., *A stochastic model for the size dependence of spherical indentation pop-in.* Journal of Materials Research, 2013. **28**(19): p. 2728-2739.
73. Kalidindi, S.R., et al., *Importance of surface preparation on the nano-indentation stress-strain curves measured in metals.* Journal of Materials Research, 2009. **24**(3): p. 1142-1155.
74. Lütjering, G. and J.C. Williams, *Titanium*. 2nd ed. Engineering materials and processes,. 2007, Berlin ; New York: Springer. xii, 442 p.
75. Donachie, M.J., *Titanium : a technical guide*. 2nd ed. 2000, Materials Park, OH: ASM International. vii, 381 p.
76. Burgers, W.G., *On the process of transition of the cubic-body-centered modification into the hexagonal-close-packed modification of zirconium.* Physica, 1934. **1**: p. 561-586.
77. Simmons, G. and H. Wang, *Single crystal elastic constants and calculated aggregate properties: a handbook*. 2d ed. 1971, Cambridge, Mass.,: M.I.T. Press. xv, 370 p.
78. Ledbetter, H., et al., *Elastic constants of body-centered-cubic titanium monocrystals.* Journal of Applied Physics, 2004. **95**(9): p. 4642-4644.
79. Agilent Technologies, I., *Agilent Technologies Nano Indenter G200 User's Guide*. 2012.
80. Vachhani, S.J., R.D. Doherty, and S.R. Kalidindi, *Effect of the continuous stiffness measurement on the mechanical properties extracted using spherical nanoindentation.* Acta Materialia, 2013. **61**(10): p. 3744-3751.
81. Pharr, G.M., J.H. Strader, and W.C. Oliver, *Critical issues in making small-depth mechanical property measurements by nanoindentation with continuous stiffness measurement.* Journal of Materials Research, 2009. **24**(3): p. 653-666.
82. Cordill, M.J., et al., *The Nano-Jackhammer effect in probing near-surface mechanical properties.* International Journal of Plasticity, 2009. **25**(11): p. 2045-2058.
83. Bartier, O., X. Hernot, and G. Mauvoisin, *Theoretical and experimental analysis of contact radius for spherical indentation.* Mechanics of Materials, 2010. **42**(6): p. 640-656.
84. Taljat, B., T. Zacharia, and F.M. Haggag, *Analysis of hall-indentation load-depth data .1. Determining elastic modulus.* Journal of Materials Research, 1997. **12**(4): p. 965-974.
85. Chaudhri, M.M., *A note on a common mistake in the analysis of nanoindentation data.* Journal of Materials Research, 2001. **16**(2): p. 336-339.
86. Fischer-Cripps, A.C., *Use of combined elastic modulus in the analysis of depth-sensing indentation data.* Journal of Materials Research, 2001. **16**(11): p. 3050-3052.

87. Minh-Quy, L., *Material characterization by instrumented spherical indentation.* Mechanics of Materials, 2012. **46**: p. 42-56.
88. Huber, N. and C. Tsakmakis, *A finite element analysis of the effect of hardening rules on the indentation test.* Journal of Engineering Materials and Technology-Transactions of the Asme, 1998. **120**(2): p. 143-148.
89. Huber, N. and C. Tsakmakis, *Experimental and theoretical investigation of the effect of kinematic hardening on spherical indentation.* Mechanics of Materials, 1998. **27**(4): p. 241-248.
90. Pane, I. and E. Blank, *Role of plasticity on indentation behavior: Relations between surface and subsurface responses.* International Journal of Solids and Structures, 2006. **43**(7–8): p. 2014-2036.
91. Ozturk, F., et al., *Influence of aging treatment on mechanical properties of 6061 aluminum alloy.* Materials & Design, 2010. **31**(2): p. 972-975.
92. Buha, J., et al., *Secondary precipitation in an Al-Mg-Si-Cu alloy.* Acta Materialia, 2007. **55**(9): p. 3015-3024.
93. Edwards, G.A., et al., *The precipitation sequence in Al-Mg-Si alloys.* Acta Materialia, 1998. **46**(11): p. 3893-3904.
94. Weaver, J.S., et al., *High Throughput Exploration of Process-Property Linkages in Al-6061 using Spherical Microindentation.* In preparation.
95. Mante, F., G.R. Baran, and B. Lucas, *Nanoindentation studies of titanium single crystals.* Biomaterials, 1999. **20**(11): p. 1051-1055.
96. Britton, T.B., et al., *The effect of crystal orientation on the indentation response of commercially pure titanium: experiments and simulations.* Proceedings of the Royal Society a-Mathematical Physical and Engineering Sciences, 2010. **466**(2115): p. 695-719.
97. Zambaldi, C., et al., *Orientation informed nanoindentation of alpha-titanium: Indentation pileup in hexagonal metals deforming by prismatic slip.* Journal of Materials Research, 2012. **27**(1): p. 356-367.
98. Fizanne-Michel, C., et al., *Determination of hardness and elastic modulus inverse pole figures of a polycrystalline commercially pure titanium by coupling nanoindentation and EBSD techniques.* Materials Science and Engineering: A, 2014. **613**: p. 159-162.
99. Merson, E., R. Brydson, and A. Brown, *The effect of crystallographic orientation on the mechanical properties of titanium*, in *Emag: Electron Microscopy and Analysis Group Conference 2007*, R.T.M.G.B.P.D. Baker, Editor. 2008.
100. Wang, Y. and J.C. Huang, *Texture analysis in hexagonal materials.* Materials Chemistry and Physics, 2003. **81**(1): p. 11-26.
101. Naka, S., L.P. Kubin, and C. Perrier, *THE PLASTICITY OF TITANIUM AT LOW AND MEDIUM TEMPERATURES.* Philosophical Magazine a-Physics of Condensed Matter Structure Defects and Mechanical Properties, 1991. **63**(5): p. 1035-1043.
102. Li, T.L., et al., *Indentation Schmid factor and orientation dependence of nanoindentation pop-in behavior of NiAl single crystals.* Journal of the Mechanics and Physics of Solids, 2011. **59**(6): p. 1147-1162.
103. Hasija, V., et al., *Deformation and creep modeling in polycrystalline Ti-6Al alloys.* Acta Materialia, 2003. **51**(15): p. 4533-4549.

104. Kwon, J., et al., *Characterization of deformation anisotropies in an alpha-Ti alloy by nanoindentation and electron microscopy.* Acta Materialia, 2013. **61**(13): p. 4743-4756.
105. Nemat-Nasser, S., W.G. Guo, and J.Y. Cheng, *Mechanical properties and deformation mechanisms of a commercially pure titanium.* Acta Materialia, 1999. **47**(13): p. 3705-3720.
106. Ghaderi, A. and M.R. Barnett, *Sensitivity of deformation twinning to grain size in titanium and magnesium.* Acta Materialia, 2011. **59**(20): p. 7824-7839.
107. Lederich, R.J., et al., *The effect of grain size on yield stress and work hardening of polycrystalline titanium at 295 K and 575 K.* Materials Science and Engineering, 1978. **33**(2): p. 183-188.
108. Salem, A.A. and S.L. Semiatin, *Anisotropy of the hot plastic deformation of Ti-6Al-4V single-colony samples.* Materials Science and Engineering a-Structural Materials Properties Microstructure and Processing, 2009. **508**(1-2): p. 114-120.
109. El-Danaf, E., S. Kalidindi, and R. Doherty, *Influence of grain size and stacking-fault energy on deformation twinning in fcc metals.* Metallurgical and Materials Transactions A, 1999. **30**(5): p. 1223-1233.
110. Yu, Q., et al., *Strong crystal size effect on deformation twinning.* Nature, 2010. **463**(7279): p. 335-338.
111. Yu, Q., R.K. Mishra, and A.M. Minor, *The Effect of Size on the Deformation Twinning Behavior in Hexagonal Close-Packed Ti and Mg.* Jom, 2012. **64**(10): p. 1235-1240.
112. Xiao, L., et al., *SIZE EFFECT ON DEFORMATION MODE IN MICRON-SIZED Ti-5Al SINGLE CRYSTAL LOADED ALONG 2 (1)over-bar (1)over-bar 0 AND 0001.* International Journal of Modern Physics B, 2010. **24**(15-16): p. 2466-2471.
113. Britton, T.B., F.P.E. Dunne, and A.J. Wilkinson, *On the mechanistic basis of deformation at the microscale in hexagonal close-packed metals.* Proceedings of the Royal Society a-Mathematical Physical and Engineering Sciences, 2015. **471**(2178).
114. Viswanathan, G.B., et al., *Direct observations and analyses alpha phase of an alpha/beta Ti-alloy of dislocation substructures in the formed by nanoindentation.* Acta Materialia, 2005. **53**(19): p. 5101-5115.
115. Gong, J.C. and A.J. Wilkinson, *Anisotropy in the plastic flow properties of single-crystal alpha titanium determined from micro-cantilever beams.* Acta Materialia, 2009. **57**(19): p. 5693-5705.
116. Kim, J.Y. and S.I. Rokhlin, *Determination of elastic constants of generally anisotropic inclined lamellar structure using line-focus acoustic microscopy.* Journal of the Acoustical Society of America, 2009. **126**(6): p. 2998-3007.
117. Atapour, M., et al., *Corrosion behaviour of investment cast and friction stir processed Ti-6Al-4V.* Corrosion Science, 2010. **52**(9): p. 3062-3069.
118. Atapour, M., et al., *Corrosion Behavior of Ti-6Al-4V with Different Thermomechanical Treatments and Microstructures.* Corrosion, 2010. **66**(6).
119. Kim, J.-Y., V. Yakovlev, and S.I. Rokhlin, *Line-focus acoustic microscopy of Ti-6242 α/β single colony: determination of elastic constants.* AIP Conference Proceedings, 2002. **615**(1): p. 1118-1125.

120. Song, Y., et al., *Calculation of bulk modulus of titanium alloys by first principles electronic structure theory.* Journal of Computer-Aided Materials Design, 1999. **6**(2-3): p. 355-362.
121. Wilson, N.C., et al., *The effect of dopant incorporation on the elastic properties of Ti metal.* Modelling and Simulation in Materials Science and Engineering, 2015. **23**(1): p. 015005.
122. Williams, J.C., R.G. Baggerly, and N.E. Paton, *Deformation behavior of HCP Ti-Al alloy single crystals.* Metallurgical and Materials Transactions A, 2002. **33**(3): p. 837-850.
123. Zaefferer, S., *A study of active deformation systems in titanium alloys: dependence on alloy composition and correlation with deformation texture.* Materials Science and Engineering: A, 2003. **344**(1–2): p. 20-30.
124. Sakai, T. and M.E. Fine, *Basal slip of Ti□Al single crystals.* Scripta Metallurgica, 1974. **8**(5): p. 545-547.
125. Sakai, T. and M.E. Fine, *Plastic deformation of Ti-Al single crystals in prismatic slip.* Acta Metallurgica, 1974. **22**(11): p. 1359-1372.
126. Conrad, H., *Effect of interstitial solutes on the strength and ductility of titanium.* Progress in Materials Science, 1981. **26**(2): p. 123-403.
127. Fitzner, A., et al., *The Effect of Aluminium on Deformation and Twinning in Alpha Titanium: The 45 degrees Case.* Light Metals Technology 2013, 2013. **765**: p. 549-553.
128. Fundenberger, J.J., et al., *Modelling and prediction of mechanical properties for materials with hexagonal symmetry (zinc, titanium and zirconium alloys).* Acta Materialia, 1997. **45**(10): p. 4041-4055.
129. Han, F., et al., *Experiments and crystal plasticity finite element simulations of nanoindentation on Ti–6Al–4V alloy.* Materials Science and Engineering: A, 2015. **625**: p. 28-35.
130. Gerday, A.F., et al., *Material behavior of the hexagonal alpha phase of a titanium alloy identified from nanoindentation tests.* European Journal of Mechanics a-Solids, 2011. **30**(3): p. 248-255.
131. Sun, Q.Y., et al., *Size effects in strength and plasticity of single-crystalline titanium micropillars with prismatic slip orientation.* Scripta Materialia, 2011. **65**(6): p. 473-476.
132. Smith, B.D., D. Shih, and D.L. McDowell, *Cyclic Plasticity Experiments and Polycrystal Plasticity Modeling of Three Distinct Ti Alloy Microstructures.* International Journal of Plasticity.
133. Phani, M.K., et al., *Mapping of elasticity and damping in an α + β titanium alloy through atomic force acoustic microscopy.* Beilstein Journal of Nanotechnology, 2015. **6**: p. 767-776.
134. Chan, K.S., C.C. Wojcik, and D.A. Koss, *Deformation of an alloy with a lamellar microstructure: experimental behavior of individual widmanstatten colonies of an α-β titanium alloy.* Metallurgical Transactions A, 1981. **12**(11): p. 1899-1907.
135. Suri, S., et al., *Room temperature deformation and mechanisms of slip transmission in oriented single-colony crystals of an alpha/beta titanium alloy.* Acta Materialia, 1999. **47**(3): p. 1019-1034.

136. He, D., et al., *Effect of retained beta layer on slip transmission in Ti-6Al-2Zr-1Mo-1V near alpha titanium alloy during tensile deformation at room temperature.* Materials & Design, 2014. **56**: p. 937-942.
137. Seal, J.R., et al., *Analysis of slip transfer and deformation behavior across the alpha/beta interface in Ti-5Al-2.5Sn (wt.%) with an equiaxed microstructure.* Materials Science and Engineering a-Structural Materials Properties Microstructure and Processing, 2012. **552**: p. 61-68.
138. Savage, M.F., et al., *Deformation mechanisms and microtensile behavior of single colony Ti-6242Si.* Materials Science and Engineering a-Structural Materials Properties Microstructure and Processing, 2001. **319**: p. 398-403.
139. Jun, T.-S., et al., *Local deformation mechanisms of two-phase Ti alloy.* Materials Science and Engineering: A, 2016. **649**: p. 39-47.
140. Ding, R.G., et al., *Transmission electron microscopy of deformed Ti-6Al-4V micro-cantilevers.* Philosophical Magazine, 2012. **92**(25-27): p. 3290-3314.
141. Gong, J. and A.J. Wilkinson, *Micro-cantilever testing of < a > prismatic slip in commercially pure Ti.* Philosophical Magazine, 2011. **91**(7-9): p. 1137-1149.
142. Mainprice, D., R. Hielscher, and H. Schaeben, *Calculating anisotropic physical properties from texture data using the MTEX open-source package.* Geological Society, London, Special Publications, 2011. **360**(1): p. 175-192.